

School of Science and Engineering  
Centre for Marine Science and Technology  
Department of Physics and Astronomy

**Spatial Variations in the Acoustic Peak Pressure  
of Impulsive Low Frequency Anthropogenic  
Signals in Underwater Marine Environments**

**Marta Galindo Romero**

Thesis presented for the Degree of  
Doctor of Philosophy  
of  
Curtin University

**June 2017**

This page intentionally left blank

# DECLARATION

To the best of my knowledge and belief this thesis contains no material previously published by any other person except where due acknowledgement has been made.

This thesis contains no material which has been accepted for the award of any other degree or diploma in any university.

Signature: \_\_\_\_\_

Date: 27 JUNE 2017

This page intentionally left blank

“Todo pasa y todo queda,  
pero lo nuestro es pasar,  
pasar haciendo caminos,  
caminos sobre el mar”.

- Antonio Machado

This page intentionally left blank

This thesis is dedicated to my family.

“Physics is not the most important thing.

Love is”.

- Richard Feynman.

This page intentionally left blank

## SUMMARY

The increasing noise pollution in the oceans during the last decades raised the concern about its potential impact on the marine environment. Various jurisdictions, regulations and policies have been developed with the goal of protecting marine life. One of the requirements is conducting noise impact assessments, as a preventive measure, prior to the commencement of an offshore industrial activity likely to produce high levels of underwater sound. Seismic surveys using airgun arrays and offshore pile driving operations are two such activities.

An important part of noise impact assessments is the modelling of noise propagation from the source and the calculation of control parameters at different distances to determine whether or not the predicted levels will be below or above the thresholds allowed by regulators. One of the control parameters for impulsive signals is the peak pressure level. This parameter, unlike other control parameters like the sound exposure level, cannot be accurately predicted at long distances with existing underwater propagation models.

This thesis aimed at understanding the changes in the peak pressure level of impulsive anthropogenic signals propagating in a randomly fluctuating underwater sound channel with the final goal of developing methods for predicting peak levels or estimating their probability distribution before the offshore industrial activities occur.

Airgun array signals from three different surveys were used to conduct an empirical analysis. This analysis led to the formulation of an empirical equation which can be used to predict the peak pressure level of anthropogenic impulsive signals based on its correlation with the sound exposure level. The regression coefficients were shown to be weakly dependent on the environmental characteristics. The equation can be applied to values of the sound exposure level predicted with a numerical model (so-called semi-empirical prediction), which provides a significant improvement in the prediction of the average value of the

peak pressure level at each range. The fluctuations around that value were estimated using extreme value theory.

The approach used to predict the peak pressure of airgun array signals was also applied to impulsive noise from offshore impact pile driving. It was demonstrated to be similarly effective for predicting the peak pressure level and its fluctuations. An additional term was added to the empirical equation to account for the effect of variation in different parameters of the piles.

Additionally, the characteristics of individual airguns and airgun arrays as an underwater sound source were investigated via modelling.

Five publications resulted from this project.

## LIST OF PUBLICATIONS

The publications arising from the development of the project and containing some of the major findings, are listed below.

- Galindo-Romero, M., A. Gavrilov, and A. Duncan, *Fluctuations of the peak pressure level of man-made impulsive sound signals propagating in the ocean*. The Journal of the Acoustical Society of America, 2017. 141(2): p. 661-668.
- Galindo-Romero, M., Lippert, T., Gavrilov A. and von Estorff, O., *Empirical prediction of peak pressure level from sound exposure level. Part I: Airgun arrays signals*. The Journal of the Acoustical Society of America, 2015. 138(6): p. EL540-EL544.
- Lippert, T., Galindo-Romero, M., Gavrilov A. and von Estorff, O., *Empirical estimation of peak pressure level from sound exposure level. Part II: Offshore impact pile driving noise*. The Journal of the Acoustical Society of America, 2015. 138(3): p. EL287-EL292.
- Galindo-Romero, M., A. Gavrilov, and A. Duncan, *Single global empirical equation for prediction of the peak pressure level of airgun arrays signals in different marine environments*, in 2nd International Conference and Exhibition on Underwater Acoustics. 2014: Rhodes, Greece. p. 1491-1496.
- Galindo-Romero, M., A. Gavrilov, and A. Duncan, *Spatial decay of the peak pressure of an air gun array signal in a range dependent environment off Cape Leeuwin, Western Australia*, in 1st International Conference and Exhibition on Underwater Acoustics. 2013: Corfu, Greece. p. 1571-1576.

This page intentionally left blank

## ACKNOWLEDGMENTS

I have always thought the Acknowledgements section of a thesis or book is quite often the nicest part of it. It is what I normally first check as a reader because it speaks volumes about the author. Ludwig Wittgenstein said “Knowledge is in the end based on acknowledgement”. Undoubtedly, with *acknowledgement* he was talking about recognition or acceptance, not gratitude. However, there are certainly many people in our lives responsible for the knowledge we have today, so the recognition of their contribution is in the end a form of gratitude itself.

Below are some of the organisations and people who helped me getting to this point of my career and my life to whom I am very thankful.

This project has been funded by Chevron through the Western Australian Energy Research Alliance (WA:ERA) within the scope of the “Marine Noise” project (PDEP AES 11-P2SR-68). I also thank Chevron for providing financial, logistical and informational support for field measurements of underwater pile driving noise in the Wheatstone project development area off Onslow, Western Australia, which was funded through WA:ERA and implemented within the scope of the project titled “Model of noise emission from marine pile driving” (PDEP AES 12-P2SR-85).

I also want to thank Geoscience Australia for providing the experimental data collected off Cape Leeuwin, RocOil Pty. Ltd for the data from Dongara, and Origin Energy for supporting measurements in Bass Strait.

I want to thank my principal supervisor, Prof. Alexander Gavrilov (Sasha). Since the beginning until the end of my PhD many people heard me saying I felt very lucky having him as my supervisor. I admire Sasha not only for his work and his impressive capacity of working on a gigantic number of projects at the same time, but also for his kindness. He has always been willing to meet me to discuss anything and I am infinitely grateful for his advice and help on this project. I have learnt so much from him and I will always be grateful for his invaluable help.

I want to thank my co-supervisor Dr. Alec Duncan for his help and guidance, not only on my thesis but also on my work in commercial jobs and tutoring. He has been very inspiring for me.

I want to thank Dr. Christine Erbe for her constant support and for believing in me even before knowing me, giving me the chance to come to Perth to join the CMST family.

I have been very fortunate of being a part of CMST, a group of fantastic researchers and fantastic people and I want to thank them all. I also want to thank the staff from the Physics department, always nice and helpful with me during these years.

I want to thank my colleagues and friends of “the dungeon”. Working on your PhD is not that hard when you are surrounded by friends. I take with me a big collection of fun memories, especially in the office. I want to thank particularly Matt for his help with this and other projects, and Jamie for correcting and thus helping me to improve my use of Shakespeare’s language and also for all the interesting conversations and advice.

I want to thank Dion for making the last stage of my PhD an easier journey and definitely a very happy time of my life.

Quiero darles las gracias a mis amigos en España. En especial, a Alba, mi mejor amiga, por estar siempre cerca, incluso estando en otra estación del año. A mis amigos de Villarrobledo, que han amenizado mis horas con sus constantes conversaciones. Y a mis amigos murcianos Jose y Javi, por su apoyo y amistad.

Finalmente, quiero dar las gracias a mi familia. Quiero agradecerles su constante apoyo, estímulo, y su amor incondicional durante toda mi vida. La familia no se puede elegir y yo me di cuenta hace mucho de lo afortunada que soy de tener una familia que siempre se ha sentido orgullosa de mí y me ha animado a ser mi mejor yo. Quiero darle las gracias a mi padre por ser un ejemplo de trabajo duro, tenacidad y por tener siempre una sonrisa en su cara. Quiero darle las gracias a mi madre por ser, no solo una de las personas más amorosas que conozco, sino por ser un ejemplo de fuerza y coraje. Para acabar, quiero darle las gracias a mi hermana por compartir conmigo su felicidad y su visión optimista del mundo, por tener siempre tiempo para hablar conmigo, y

por ser un ejemplo para mí, a pesar de ser la pequeña. No podría imaginar mi vida sin ellos. Esta tesis es para ellos.

This page intentionally left blank

# TABLE OF CONTENTS

SUMMARY .....	i
LIST OF PUBLICATIONS.....	iii
ACKNOWLEDGMENTS .....	v
TABLE OF CONTENTS .....	ix
LIST OF FIGURES.....	xiii
LIST OF TABLES.....	xxv
THESIS STRUCTURE.....	xxvii
Chapter 1. Introduction.....	1
1.1 Motivation and significance.....	1
1.1.1 Sources of sound in the ocean.....	1
1.1.2 Noise impact.....	4
1.1.3 Control parameters.....	9
1.2 Scope and objectives.....	11
Chapter 2. Theoretical Background.....	13
2.1 Sound propagation in a fluctuating ocean.....	13
2.2 Sound from industrial activities.....	17
2.2.1 Signals from offshore seismic surveys using airguns.....	18
2.2.1.1 Airguns.....	19
2.2.1.2 Airgun arrays.....	21
2.2.1.3 Modelling of sound emission from airguns and airgun arrays	
23	
2.2.2 Signals from offshore impact pile driving.....	26
2.2.2.1 Modelling of sound emission from pile driving.....	28
2.3 Underwater sound propagation modelling.....	28
2.3.1 Existing underwater sound propagation models.....	30
2.4 Prediction of control parameters.....	37
2.4.1 Prediction of the sound exposure level.....	38
2.4.2 Prediction of the peak pressure level.....	38

2.4.3	Discussion.....	41
Chapter 3.	Experimental airgun array data: Description and processing.....	43
3.1	Cape Leeuwin.....	44
3.1.1	Description of the survey .....	44
3.1.2	Signal processing .....	47
3.2	Dongara 48	
3.2.1	Description of the survey .....	48
3.2.2	Signal processing .....	50
3.3	Bass Strait .....	53
3.3.1	Description of the survey .....	53
3.3.2	Signal processing .....	54
Chapter 4.	Modelling of sound propagation: Numerical simulation using the data of Cape Leeuwin.....	57
4.1	Description of the simulations .....	57
4.1.1	Sound propagation modelling.....	57
4.1.2	Source .....	59
4.1.3	Geoacoustic model .....	60
4.1.4	Calculated metrics .....	61
4.1.5	Numerical prediction results and comparison with measurements .....	62
4.2	Concluding remarks .....	65
Chapter 5.	Empirical analysis of airgun array signals and semi-empirical prediction of peak pressure .....	67
5.1	Preliminary empirical results.....	68
5.2	Individual data sets .....	70
5.2.1	Cape Leeuwin .....	70
5.2.2	Dongara.....	73
5.2.3	Bass Strait.....	80
5.2.4	Discussion.....	85
5.3	Generalised analysis of data sets .....	85
5.3.1	Overview .....	85
5.3.2	Analysis.....	88
5.3.3	Application of the generalised equation to all environments .....	88

5.3.4	Statistical analysis.....	92
5.4	Semi-empirical prediction .....	95
5.4.1	Description of the algorithm.....	96
5.4.2	Application of the algorithm .....	97
5.4.3	Statistical analysis.....	99
5.5	Concluding remarks.....	100
Chapter 6.	Analysis of single airguns and airguns arrays as acoustic sources ...	101
6.1	Single airguns.....	102
6.2	Airgun arrays .....	104
6.2.1	Description of the arrays .....	104
6.2.2	Correlation between peak pressure level and sound exposure level for different azimuth angles .....	109
6.3	Concluding remarks.....	113
Chapter 7.	Fluctuations of peak pressure around the mean value .....	115
7.1	Randomness of the peak pressure.....	115
7.2	Theoretical foundation.....	117
7.3	Analysis of the combined data set .....	121
7.4	Analysis of the Cape Leeuwin data .....	123
7.4.1	Cape Leeuwin – Empirical analysis.....	123
7.4.2	Cape Leeuwin – Semi-empirical analysis .....	127
7.5	Description of the algorithm .....	130
7.6	Concluding remarks.....	133
Chapter 8.	Estimation of peak pressure level of signals from offshore impact pile driving operations.....	135
8.1	Pile driving experimental data .....	136
8.2	Analysis of correlation for pile driving data .....	137
8.3	Correction of empirical equation for peak pressure level estimation of pile driving signals with different hammer-pile interaction .....	140
8.4	Fluctuations of the peak pressure level of pile driving signals around the mean value .....	143
8.4.1	Analysis of the Onslow data.....	143
8.4.2	Description of the algorithm.....	144
8.5	Concluding remarks.....	147

Chapter 9. Conclusions.....	149
9.1 Conclusions.....	149
9.2 Future work .....	153
REFERENCES .....	155
APPENDIX A: Acronyms .....	171
APPENDIX B: Symbols .....	173
APPENDIX C: Transmission loss associated of signal energy modelled for different attenuation coefficients .....	177

## LIST OF FIGURES

Fig. 1.1: Different sources of sound in the ocean. Sound propagation from sources is represented by spherical wave fronts in all cases for simplicity. Biological sources are represented in white and anthropogenic sources are represented in red. The waveform of an airgun array signal is also included (front red signal).....	3
Fig. 2.1: Possible sound propagation paths underwater (straight lines). Dotted lines represent two different sound speed profiles. ....	14
Fig. 2.2: Airgun array (short thick orange lines) and hydrophone array (long yellow lines with green dots) towed from vessel.....	18
Fig. 2.3: Schematic view of a seismic survey. Sound signals are emitted from the airgun array (short orange line) and received on the hydrophone array (long green lines) after reflection from different sediment layers. ....	19
Fig. 2.4: An idealised illustration of sound signal generation by an underwater explosion or airgun.....	20
Fig. 2.5: Sound pressure waveform from a single airgun simulated at long ranges in the vertically downward direction, and then reduced to 1 m from the centre of the source. The primary pulse is the direct arrival of the shock wave, followed by its reflection from the sea surface with negative amplitude, and then by the bubble pulses.....	21
Fig. 2.6: Sound pressure waveform of a 4230 cui airgun array simulated for an equivalent point source at 1 m from its centre in boundary free space (i.e. no reflection from the sea surface in contrast to the waveform shown in Fig. 2.5).....	22
Fig. 2.7: Airguns in array.....	23

Fig. 2.8: Waveform simulated with CMST’s airgun model (red) compared with the measured (reference) waveform of the array (blue).....	26
Fig. 2.9: Illustration of vertical pile being driven into the seafloor by hammer impacts and corresponding emission of noise in the water.....	27
Fig. 3.1: Map of Australia showing the three locations where the airgun array seismic surveys were conducted. ....	44
Fig 3.2: Map of Cape Leeuwin and Cape Naturaliste with the HA01 station and seismic survey tracks.....	45
Fig 3.3: Hydrophone array of station HA01 off Cape Leeuwin. Figure based on Alexander Gavrilov’s illustration. ....	46
Fig. 3.4: Sound speed profile over the continental slope off Cape Leeuwin measured in November 2005.....	46
Fig. 3.5: Bathymetry along the acoustic propagation path (highlighted in Fig. 3.2 with a thick red line). The position of the receiver is depicted by a yellow dot at 1100 m from the surface. ....	47
Fig. 3.6: Waveform of the first shot recorded at 16.9 km from the source. ....	48
Fig. 3.7: General map of the survey with the location of recorders 1, 2 and 3 [126]. ....	49
Fig. 3.8: Location of survey shots (blue) and tracks analysed (red). The magenta dots are the receiver location. The coordinates are given in metres for UTM zone 50.....	52
Fig. 3.9: Track 1 of Bass Strait survey. ....	54
Fig. 3.10: Waveform measured at different distances from the source.....	55
Fig. 3.11: Bathymetry (blue line) along transects from the sound receiver to the furthest shot location of seismic tracks 1 (top), 2 (middle) and 3 bottom. Red dots show sea depth at the location of each shot of the three seismic tracks versus distance to the receiver. Note that the sound propagation	

paths from different shots were not fully coincident with the seismic tracks. Therefore the sea depth at shot locations differs from that measured at the same distance from the sound receiver in the direction to the furthest shot..... 56

Fig. 4.1: Modelled source signal for 0 degrees elevation and 0 degrees azimuth. 60

Fig. 4.2: Comparison of the transmission loss obtained from the experimental data and simulations with RAMGeo and adiabatic mode model. The *TL* is shown for the sound exposure level (top) and peak pressure level (bottom)..... 62

Fig. 4.3: Comparison of the transmission loss obtained from experimental data and simulations with RAMGeo and adiabatic mode model (AMM) in octave bands 10-20 Hz (top), 20-40 Hz (middle), 40-80Hz (bottom). *TL* for sound exposure (left); *TL* for peak pressure (right). ..... 64

Fig. 5.1: Waveforms of airgun array signals received at different distances from the source: short distances 17.4 km, and 16.9 km (left panels), and long distances 82.8 km and 83.0 km (right panels). ..... 69

Fig. 5.2: Experimental transmission loss of the sound exposure and the peak pressure levels..... 70

Fig. 5.3: Measured peak pressure level versus sound exposure level and the line from best linear fit. .... 71

Fig. 5.4: Sound exposure level, peak pressure level and empirical prediction of peak pressure level from sound exposure level..... 72

Fig. 5.5: Distribution of  $\Delta L_{peak}$  for Cape Leeuwin measurements and its best fit by a normal distribution. (a) Histogram and best-fit by normal Probability Density Function (PDF) (red line), (b) Cumulative Density Function (CDF). Parameters of the normal distribution fit: mean  $\mu = -0.07$  dB and standard deviation  $\sigma = 1.87$  dB. Results of K-S test:  $h = 1, p = 0.000006, \alpha = 0.05$ ..... 73

Fig. 5.6: Experimental transmission loss of the sound exposure and peak pressure levels for each of the six seismic tracks..... 74

Fig. 5.7:  $L_{peak}$  vs.  $SEL$  and regression line for each of six selected tracks of the Dongara survey..... 76

Fig. 5.8: Sound exposure level, peak pressure level and empirical predictions of peak pressure level for each selected line of the Dongara survey. .... 77

Fig. 5.9: Distribution of  $\Delta L_{peak}$  for Track 1NW of Dongara measurements. (a) Histogram of experimental data and best fit by normal PDF (red line), (b) CDF. Parameters of the normal distribution fit:  $\mu = -0.65$  dB,  $\sigma = 1.22$  dB. Parameters of K-S test:  $h = 1$ ,  $p = 0.025150$ ,  $\alpha = 0.05$ . .... 78

Fig. 5.10: Distribution of  $\Delta L_{peak}$  for Track 1SE of Dongara measurements. (a) Histogram of experimental data and best fit by normal PDF (red line), (b) CDF. Parameters of the normal distribution fit:  $\mu = -0.24$  dB,  $\sigma = 1.60$  dB. Parameters of K-S test:  $h = 0$ ,  $p = 0.618343$ ,  $\alpha = 0.05$ . .... 78

Fig. 5.11: Distribution of  $\Delta L_{peak}$  for Track 2NW of Dongara measurements. (a) Histogram of experimental data and best fit by normal PDF (red line), (b) CDF. Parameters of the normal distribution fit:  $\mu = 0.30$  dB,  $\sigma = 1.21$  dB. Parameters of K-S test:  $h = 0$ ,  $p = 0.110303$ ,  $\alpha = 0.05$ . .... 78

Fig. 5.12: Distribution of  $\Delta L_{peak}$  for Track 2SE of Dongara measurements. (a) Histogram of experimental data and best fit by normal PDF (red line), (b) CDF. Parameters of the normal distribution fit:  $\mu = 0.39$  dB,  $\sigma = 1.42$  dB. Parameters of K-S test:  $h = 0$ ,  $p = 0.070417$ ,  $\alpha = 0.05$ . .... 79

Fig. 5.13: Distribution of  $\Delta L_{peak}$  for Track 3SW of Dongara measurements. (a) Histogram of experimental data and best fit by normal PDF (red line), (b) CDF. Parameters of the normal distribution fit:  $\mu = 0.67$  dB,  $\sigma = 1.19$  dB. Parameters of K-S test:  $h = 0$ ,  $p = 0.664172$ ,  $\alpha = 0.05$ . .... 79

Fig. 5.14: Distribution of  $\Delta L_{peak}$  for Track 3NE of Dongara measurements. (a) Histogram of experimental data and best fit by normal PDF (red line), (b) CDF. Parameters of the normal distribution fit:  $\mu = 1.29$  dB,  $\sigma = 1.39$  dB. Parameters of K-S test:  $h = 0$ ,  $p = 0.607051$ ,  $\alpha = 0.05$ ..... 79

Fig. 5.15: Experimental transmission loss of the sound exposure and the peak pressure levels measured in Bass Strait: Track 1 (top), Track 2 (centre), and Track 3 (bottom)..... 81

Fig. 5.16:  $L_{peak}$  vs.  $SEL$  and regression line from Bass Strait data: Track 1 (top), Track 2 (centre), and Track 3 (bottom)..... 82

Fig. 5.17:  $SEL$  (red), measured  $L_{peak}$  (blue) and empirical predictions of  $L_{peak}$  (green) from Bass Strait data. Track 1 (top), Track 2 (centre), and Track 3 (bottom)..... 83

Fig. 5.18: Distribution of  $\Delta L_{peak}$  for Track 1 of Bass Strait measurements. (a) Histogram of experimental data and best fit by normal PDF (red line), (b) CDF. Parameters of the normal distribution fit:  $\mu = -1.55$  dB,  $\sigma = 1.06$  dB. Parameters of K-S test:  $h = 0$ ,  $p = 0.553056$ ,  $\alpha = 0.05$ ..... 84

Fig. 5.19: Distribution of  $\Delta L_{peak}$  Track 3 of Bass Strait measurements. (a) Histogram of experimental data and best fit by normal PDF (red line), (b) CDF. Parameters of the normal distribution fit:  $\mu = -0.30$  dB,  $\sigma = 1.69$  dB. Parameters of K-S test:  $h = 0$ ,  $p = 0.747970$ ,  $\alpha = 0.05$ ..... 84

Fig. 5.20: Distribution of  $\Delta L_{peak}$  for Track 3 of Bass Strait measurements. (a) Histogram of experimental data and best fit by normal PDF (red line), (b) CDF. Parameters of the normal distribution fit:  $\mu = -1.14$  dB,  $\sigma = 1.28$  dB. Parameters of K-S test:  $h = 0$ ,  $p = 0.849395$ ,  $\alpha = 0.05$ ..... 84

Fig. 5.21: Experimental  $L_{peak}$  vs.  $SEL$  in dB (green dots) and the linear regression line (blue) from all measurement data. .... 88

Fig. 5.22: Measured sound exposure level (red), measured peak pressure level (blue), empirical prediction of peak pressure level from *SEL* with the specific regression coefficients (green), and empirical prediction of peak pressure level from *SEL* with the generalised regression coefficients (yellow) in Eq. 5.1 for the Cape Leeuwin data..... 89

Fig. 5.23: Measured sound exposure level (red), measured peak pressure level (blue), empirical prediction of peak pressure level with the specific regression coefficients (green), and empirical prediction of peak pressure level with the generalised regression coefficients (yellow) for all tracks of the Dongara data set. .... 90

Fig. 5.24: Measured sound exposure level (red), measured peak pressure level (blue), empirical prediction of peak pressure level with the specific regression coefficients (green), and empirical prediction of peak pressure level with the generalised regression coefficients (yellow) for Tracks 1 (top), 2 (centre) and 3 (bottom) of the Bass Strait measurements..... 91

Fig. 5.25: Distribution of  $\Delta L_{peak}$  with all data and fit to a normal distribution. (a) Histogram of measure data and its best fit by normal distribution PDF (red line), (b) CDF. Parameters of the normal distribution fit:  $\mu = 0.00$  dB,  $\sigma = 1.64$  dB. Parameters of K-S test:  $h = 1, p = 0.000666$  with  $\alpha = 0.05$ . .... 93

Fig. 5.26: Distribution of the number of shots with range from all tracks used for analysis. .... 94

Fig. 5.27: Distribution of  $\Delta L_{peak}$  for short ranges (in the range interval [1.3, 15.0] km) and fit to a normal distribution. (a) Histogram of measure data and its best fit by normal distribution PDF (red line), (b) CDF. Parameters of the normal distribution fit:  $\mu = 0.04$  dB,  $\sigma = 1.50$  dB. Parameters of K-S test:  $h = 0, p = 0.080153, \alpha = 0.05$ ..... 94

Fig. 5.28: Distribution of  $\Delta L_{peak}$  for medium ranges (in the range interval [15.0, 68.0] km) and fit to a normal distribution. (a) Histogram of measure data and its best fit by normal distribution PDF (red line), (b) CDF. Parameters of the normal distribution fit:  $\mu = -0.12$  dB,  $\sigma = 1.90$  dB. Parameters of K-S test:  $h = 1, p = 0.000006, \alpha = 0.05$ . ..... 95

Fig. 5.29: Distribution of  $\Delta L_{peak}$  in the range interval [68.0, 94.0] km and fit to a normal distribution. (a) Histogram of measure data and its best fit by normal distribution PDF (red line), (b) CDF. Parameters of the normal distribution fit:  $\mu = 0.03, \sigma = 1.81$  dB. Parameters of K-S test:  $h = 0, p = 0.073123, \alpha = 0.05$ . ..... 95

Fig. 5.30: Visualization of semi-empirical prediction algorithm. .... 97

Fig. 5.31: Peak pressure level vs range. Measurements (blue); prediction obtained directly from the waveform simulated using RAMGeo (red); and semi-empirical prediction obtained using the linear equation (5.1) with the generalised coefficient and the numerically predicted *SEL* values (yellow). ..... 98

Fig. 5.32: Distribution of  $\Delta L_{peak}$ , being this the difference between the measurements and the semi-empirical prediction using the linear equation with the generalised coefficients and RAMGeo modelling results for the Cape Leeuwin data. (a) Experimental histogram and PDF (red line) of the best normal distribution fit, (b) CDF and its fit. Parameters of the normal distribution fit:  $\mu = 0.09$  dB,  $\sigma = 2.79$  dB. Parameters of K-S test:  $h = 1, p = 0, \alpha = 0.05$ . ..... 99

Fig. 6.1: Waveforms (top) and energy spectral level (bottom) of a signal for a single airgun of 150 cui predicted by the CMST airgun model. The signal reflected from the sea surface (ghost) is not included. .... 102

Fig. 6.2: Left: Sound exposure level vs. volume for five single airguns. Right: Squared peak pressure vs. volume for the same single airguns. .... 103

Fig. 6.3: Coefficient  $B$  vs Volume for  $A = 1$  for single airgun signals in semi-logarithmic scale. .... 104

Fig. 6.4: Horizontal layout of airgun arrays. Array elements are shown much larger than actual size, comparing to the distance between the guns, but are scaled proportional to the cube root of their volume..... 106

Fig. 6.5: Comparison between the waveforms (top) and energy spectral level (bottom) for Array 1 towed at 9 m below the sea surface. The example (measured) signal for the vertically downward direction (blue) and the signal predicted by the CMST's airgun array model (red). .... 107

Fig. 6.6: Comparison between the waveforms (top) and energy spectral level (bottom) for Array 2 towed at 7 m below the sea surface. The example (measured) signal for the vertically downward direction (blue) and the signal predicted by the CMST's airgun array model (red). .... 107

Fig. 6.7: Comparison between the waveforms (top) and energy spectral level (bottom) for Array 3 towed at 7 m below the sea surface. The example (measured) signal for the vertically downward direction (blue) and the signal predicted by the CMST's airgun array model (red). .... 108

Fig. 6.8: Comparison between the waveforms (top) and energy spectral level (bottom) for Array 4 towed at 6 and 9 m (V-shaped) below the sea surface. The example (measured) signal for the vertically downward direction (blue) and the signal predicted by the CMST's airgun array model (red). .... 108

Fig. 6.9: Comparison between the waveforms (top) and energy spectral level (bottom) for Array 5 towed at 10 m below the sea surface. The example (measured) signal for the vertically downward direction (blue) and the signal predicted by the CMST's airgun array model (red). .... 109

Fig. 6.10: Coefficient  $B$  vs Volume for  $A = 1$  for airgun array signals..... 110

Fig. 6.11: Variation of $SEL$ in dB re 1 $\mu\text{Pa}^2\cdot\text{s}$ (top blue) and $L_{peak}$ in dB re 1 $\mu\text{Pa}$ (bottom red) vs azimuth angle in degrees, calculated for source signals modelled for Array 5.....	111
Fig. 6.12: $B'$ vs azimuth angle in degrees, calculated for source signals modelled for Array 5. ....	113
Fig. 7.1: Fluctuations of the ratio $y$ around the constant value of $10^{B_G/10}$ derived from Eq. 7.2 using the coefficient $A_G$ . The number $n$ represents the order of each individual measurement of the generalised data set at different locations. ....	122
Fig. 7.2: Histogram of $y$ and its best fit by the Gumbel distribution for the combined data set. ....	122
Fig. 7.3: Fluctuations of ratio $y$ around the constant $10^{B_S/10}$ u derived from Eq. 7.2 using the Cape Leeuwin data set and the coefficient $A_S$ . ....	124
Fig. 7.4: Histogram of $y$ and best fit to the Gumbel distribution for the Cape Leeuwin data set based on the experimental values. ....	124
Fig. 7.5: CDF of $L_{peak}$ calculated for two different $SEL$ values using the regression coefficients and Gumbel distribution parameters derived from the combined data set (solid blue) and only from the Cape Leeuwin set (solid red). The dashed vertical lines show the estimation of $L_{peak}$ using the generalised (blue) and Cape Leeuwin specific regression coefficients (red). ....	125
Fig. 7.6: Estimation of $L_{peak} _P$ for $P = 0.9$ for the Cape Leeuwin data set using experimental $SEL$ values. The red curve was obtained with the use of the specific coefficients and the green curve with the generalised coefficients. ....	126
Fig. 7.7: Estimation of $L_{peak}$ vs range for the Cape Leeuwin data set. The upper limit $L_{peak} _P$ estimated for probability $P = 0.9$ using the generalised	

Gumbel distribution parameters (green line) is compared with experimental measurements (blue line) and the empirical estimation of the mean value using Eq. 5.1 (magenta)..... 127

Fig. 7.8: Prediction of  $L_{peak} | P$  for P = 0.9 for the Cape Leeuwin data set using the semi-empirical prediction of  $L_{peak}$  from *SEL*. The red curve was obtained with the use of the specific coefficients and the green curve with the generalised coefficients..... 128

Fig. 7.9: Prediction of  $L_{peak}$  and its upper limit of 90% probability vs range for the Cape Leeuwin data set. Semi-empirical prediction of the average value of  $L_{peak}$  (magenta). The upper limit for the 90% of values (green). Experimental measurements of  $L_{peak}$  (blue)..... 129

Fig. 7.10: Visualization of the algorithm to estimate the upper limit of  $L_{peak}$  fluctuations for specified probability as a function of range from an airgun array. .... 132

Fig. 8.1: Map of the area with location of piles (blue dots) and noise recorders (red dots). The panel on the right side shows the layout of the piles... 137

Fig. 8.2: Measurements of *SEL* and  $L_{peak}$  vs. range..... 138

Fig. 8.3: Measurements of  $L_{peak}$  vs. *SEL* from vertical (blue dots) and slanting (red dots) pile. The black dashed line shows the best linear fit for the relationship derived from all samples. .... 138

Fig. 8.4: Distribution of the difference between measured  $L_{peak}$  values and their prediction from the corresponding *SEL* values using Eq. 5.1 with the regression coefficients  $A = 1.13$  and  $B = 2.4$  dB (blue bars) and fit to a normal distribution (red). (a) Histogram, (b) Cumulative Density Function (CDF). Parameters of the normal fit:  $\mu = -2.3979e-013$  dB,  $\sigma = 1.3878$  dB. .... 139

Fig. 8.5: Fluctuations of the ratio  $y$  around the constant value of  $10^{B/10}$  predicted from Eq. 7.2 using the coefficient  $A$ . The number  $n$  represents the order of each individual measurement of the data set. .... 143

Fig. 8.6: (a) Histogram of  $y$  calculated with the experimental data (blue) and its best fit by a Gumbel distribution (red). (b) Cumulative Density Function (CDF) of measurements (blue) and Gumbel distribution fit (red). ..... 144

Fig. 8.7: Visualization of the algorithm to estimate the fluctuations of  $L_{peak}$  around its mean value and its upper limit of chosen probability for pile driving signals..... 146

This page intentionally left blank

## LIST OF TABLES

Table 3.1: Description of tracks after data selection .....	50
Table 3.2: Description of tracks after processing .....	55
Table 5.1: Regression coefficients of Dongara data .....	75
Table 5.2: Regression coefficients of Bass Strait data .....	80
Table 5.3: Experimental data from all surveys.....	87
Table 5.4: Parameters of normal distribution fit and K-S test for generalised data set at different ranges.....	92
Table 6.1: Description of airgun arrays .....	105
Table 8.1: Regression coefficients for pile driving data .....	139
Table 8.2: Comparison of pile characteristics between Port Phillip Bay and Onslow .....	140

This page intentionally left blank

## THESIS STRUCTURE

**T**he thesis is divided into nine chapters and three appendices containing the information described below.

Chapter 1 is the introduction of the thesis. It presents the project by explaining the motivation and importance in relation to the current context in the field. Subsequently the objectives of the project are described.

Chapter 2 summarizes the relevant theory related to the project, including: characteristics of sound propagation in a fluctuating ocean, description of the main anthropogenic sources of sound, principles of underwater acoustic modelling, and analysis of the difficulties encountered with the prediction of the main parameters that are used in the context of noise impact assessment.

Chapter 3 describes the experimental seismic data used in this study. Three sets of measurements from different seismic surveys using airgun arrays are described, in conjunction with the processing done for each set.

Chapter 4 is dedicated to the modelling of sound propagation for one of the environments studied. It includes the description of the propagation model; the modelling of the source, the seafloor and the water column; and the results obtained, which are compared with the measurements. The modelling results are also used in the analysis described in the following chapters.

Chapter 5 focuses on an empirical analysis of the seismic data. Individual analyses were conducted for each location, followed by a generalised analysis, resulted from the results obtained in the individual analyses.

Chapter 6 considers the dependence of the relationship between the peak pressure and sound exposure levels at the sound source on parameters of single airguns and airgun arrays.

Chapter 7 complements the study of Chapter 5 with a method to estimate the fluctuations of the peak pressure level around the predicted mean value.

Chapter 8 is based on the application of the empirical equation used with airgun arrays signals to predict the peak pressure level from offshore pile driving activities.

Chapter 9 summarises the main conclusions of the project, followed by suggestions for the future work on this topic.

Finally, after the references section, three appendices are included. Appendix A gives the different acronyms used in the text, Appendix B presents the list of symbols of parameters with a reference to their definition, and Appendix C includes an extra result that was not included in the main text.

All illustrations presented in this thesis have been made by the author unless stated otherwise.

# Chapter 1.

## Introduction

**T**his chapter aims to provide a general outline of the thesis and to put the project into context. The first section presents the motivation, explaining the reasons that led to the development of this project together with its importance. The second and final section describes the scope and main objectives of this study.

### 1.1 Motivation and significance

#### 1.1.1 Sources of sound in the ocean

There are many different sources of sound in the ocean, some of them represented in Fig. 1.1. They can be classified into two main groups: natural and anthropogenic sources. Both of them contribute to the total ambient sound in the ocean [1].

Natural sound can have a physical or biological origin. Some examples of physical sound sources in the ocean are rain falling over the water, ice cracking and breaking up, wind waves and earthquakes. Biological sound is the one produced by marine organisms in an intentional or unintentional way. In relation to the former, sound plays a very important role in the life of many marine animals for the interaction with their environment and between each other. Because of its efficient underwater propagation, sound is employed by different species in different activities, including communication (at short or long distances), foraging, search for habitats, navigation, mating, etc. [2] as a consequence of the evolution of the vocal and auditory system of many marine

animals [3]. However, these signals can experience interferences with other acoustic signals, including anthropogenic sounds progressively more present in the ocean.

Anthropogenic sound can also be produced intentionally (since sound propagates in water much better than electromagnetic waves) or unintentionally, as a result of the increasing industrial marine operations. In general, these operations generate high levels of underwater sound (e.g. 227 dB re 1 $\mu$ Pa for the peak pressure at 5 m from impact pile driving [4, 5]), which have a potential impact on many marine organisms, as discussed in the next subsection. The major underwater noise sources are offshore seismic surveys, pile driving for offshore installations, explosions, and active sonar operations [6]. Subsea drilling and dredging can produce high intensity noise as well [7, 8]. This thesis focuses on the noises produced by seismic surveys and offshore pile driving.

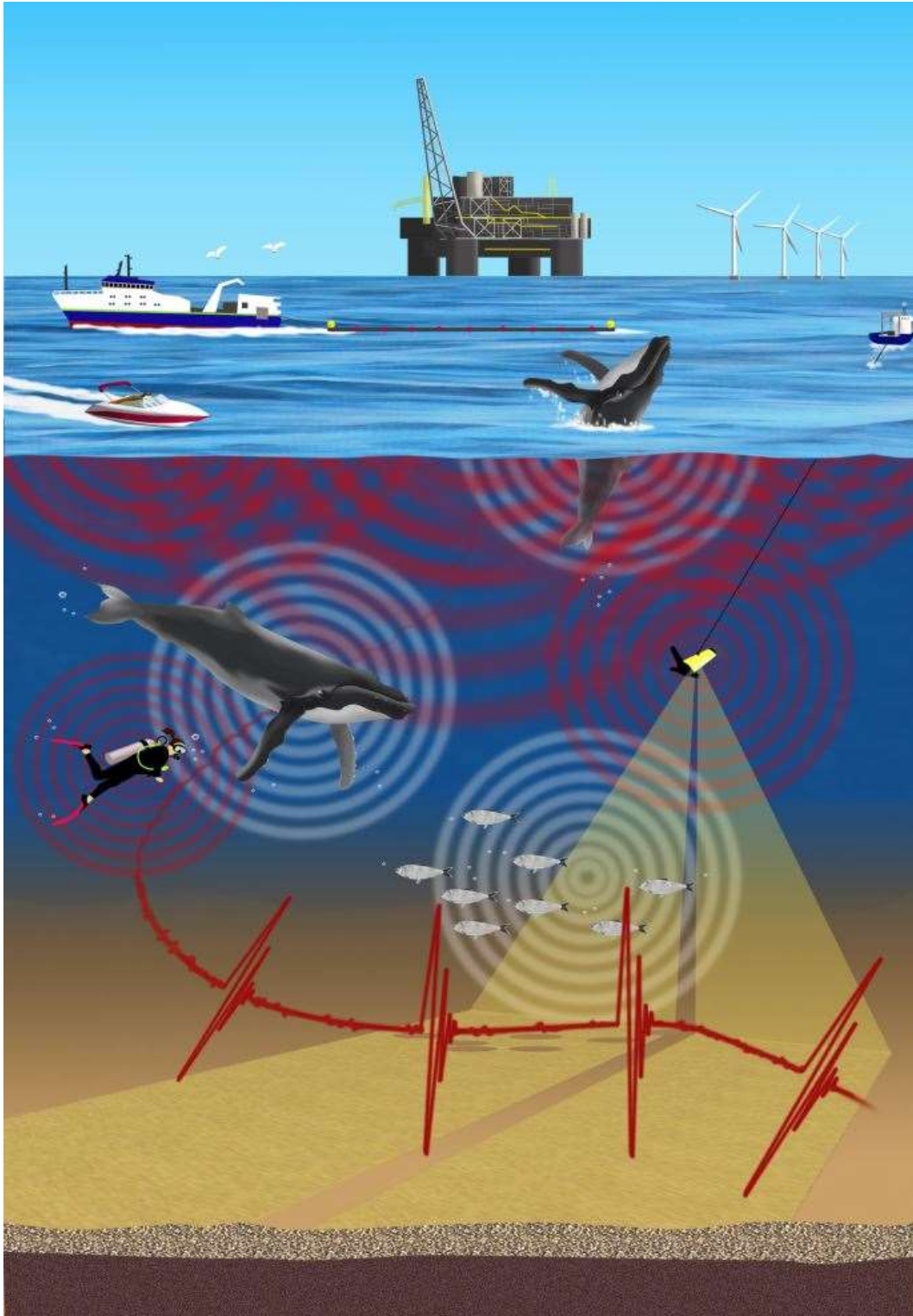


Fig. 1.1: Different sources of sound in the ocean. Sound propagation from sources is represented by spherical wave fronts in all cases for simplicity. Biological sources are represented in white and anthropogenic sources are represented in red. The waveform of an airgun array signal is also included (front red signal).

### 1.1.2 Noise impact

There is a real concern about the increase of anthropogenic sound levels in the ocean and the impact of noise on marine animals [2, 8-14]. In this thesis “noise” refers to the unwanted sound that could have a negative effect on some organisms.

The possible effects of noise on marine animals can be classified into four categories [15]:

- Physical and physiological.

These effects include damages on the hearing system of animals, threshold shifts, etc. Several studies have been conducted to determine the occurrence of some of these effects on certain species, but not all of them led to the same conclusions. For instance, assessing the problem of whether exposure to airgun signals can produce damage on fish ears, studies like [16] concluded that this exposure can produce important damages to the fish ears, whereas other studies like [17-19] support the lack of correlation between airgun signal pressure waveforms and fish hearing damage for the species studied. In a more recent study with pulses from waterguns, sound exposure levels to induce mortality related to tissue injury on Northern Pike were determined [20]. That study was conducted to develop methods to control invasive fish, but it also proved the impact of impulsive sources on this specific fish and potentially on others with similar hearing system tissues.

- Perceptual.

These effects are related to the interference and masking of biological sounds used for communication and echolocation with anthropogenic sounds [21]. For instance, noise produced by fast whale-watching boats masked killer whale calls from 14 km according to a model applied in Southern British Columbia [22]. Masked temporary threshold shift (MTTS) were observed in harbour porpoises after exposure to airgun signals [23] and also in white whales after exposure to a water gun [24].

- Behavioural.

These effects include disruptions on migration, avoidance of specific areas, changes on calling rates, etc. Some animals like humpback whales, sea turtles and fish have been seen to avoid sources of noise like marine surveys and show an alarm response [25, 26]. Other behavioural responses have been observed in different fish and squid during and after airgun noise exposure [26]. In contrast, other marine mammals like grey whales in the north-eastern coast of Sakhalin Island, Russia, did not show significant changes in their movement and behaviour in presence of seismic surveys [27]. Regarding whale's songs, recent studies have demonstrated the effect of anthropogenic noise on changes on calling rates for bowhead whales [28], humpback whales [29] and blue whales [30].

- Indirect.

These effects can include a reduction of feeding rates as a consequence of the decrease in the number of preys because of some of the other effects described above. This decrease in the number of fish means as well a decrease in the number of commercial catches, which is a concern for fishermen [31].

These and many other studies conclude that anthropogenic noise can have a negative effect on marine animals, especially at short ranges, but there is still much that is not understood or known and more data and studies are needed [13, 15]. For example, it is known that the impact of sound on animals depends to some extent on the frequency range that the specific species can hear and the level of sound [4] but more measurements of audiograms for different species are needed because the current number is very limited or even inexistent for some species [32]. Also, more measurements of anthropogenic noise which can potentially have adversely effects on marine animals are necessary. Without this information the possibility of obtaining definite results is restrained.

Attending to the issues described previously, the impact of sound on marine animals is the object of many current research projects. Some organizations are working in this field trying to assess it (e. g. the Population Consequences of

Disturbance (PCoD) model [33]) while others are trying to reduce the levels of anthropogenic sound generated in the ocean to prevent that impact. For instance, the Scientific Committee on Oceanic Research and the Partnership for Observation of the Global Oceans are working towards an International Quiet Ocean Experiment [34] to confront the problem of noise impact on marine life with a combined effort.

This concern has also been reflected in the latest regulations, policies, and initiatives focused on the protection of the marine environment [35]. Some examples in different countries, described in more detail in [32], are presented below organized by geographical areas.

### **Australia and New Zealand**

- The Australian *Environment Protection and Biodiversity Conservation Act 1999* (EPBC) [36].

Following [37], this regulation compels the Defence to avoid those Navy activities that produce a significant environmental impact, like the underwater noise from active sonar. Through the Australian *EPBC Act Policy Statement 2.1 - Interaction between offshore seismic exploration and whales* [38] precaution zones are defined for proposed seismic surveys;

- The National Offshore Petroleum Safety and Environmental Management Authority (NOPSEMA).

It manages the noise exposure in marine environments within Commonwealth waters;

- The New Zealand 2013 Code of Conduct for Minimising Acoustic Disturbance to Marine Mammals from Seismic Survey Operations [39].

The Code requires sound transmission modelling to indicate whether received sound exposure levels in Areas of Ecological Importance or Marine Mammal Sanctuaries will exceed 186 dB re 1  $\mu\text{Pa}^2\cdot\text{s}$  at a range of 200 m from the acoustic source, or 171 dB re 1  $\mu\text{Pa}^2\cdot\text{s}$  at ranges of 1 km and 1.5 km.

## Europe

- The *EC Marine Strategy Framework Directive* (MSFD) [40].

Its aim is protecting the marine environment across Europe. Its Descriptor 11 includes underwater noise to be such as it does not negatively affect the marine environment. It occurs in the context of the requirement for the member states to achieve *Good Environmental Status* (GES) by 2020, as stated in Article 9. One of the control magnitudes adopted is the peak sound pressure level, defined as the zero-to-peak amplitude of the pulse, as it is mentioned and defined in [40, 41];

- The OSPAR Commission [42].

It includes fifteen Governments of Europe working towards the protection of the marine environment of the North-East Atlantic, including managing of underwater noise;

- The Joint Nature Conservation Committee (JNCC).

JNCC works closely with the Government of the UK managing underwater noise and mitigation practices;

- The Agreement on the Conservation of Small Cetaceans of the Baltic and North Seas (ASCOBANS).

Some of its goals are preventing injury of the cetaceans during seismic surveys and pile driving activities. JNCC has established guidelines to achieve those goals;

- The Agreement on the Conservation of Cetaceans of the Black Sea, Mediterranean Sea and Contiguous Atlantic Area (ACCOBANS).

A working group was created to work on the mitigation of noise impacts [43];

- The Baltic Marine Environment Protection Commission - Helsinki Commission (HELCOM).

It was established with the goal of protecting the marine environment of the Baltic Sea from all sources of pollution through intergovernmental

cooperation. Its Life+ project Baltic Sea Information on the Acoustic Soundscape (BIAS) aims at having soundscape maps of commercial vessels in the Baltic Sea.

## United States of America

- The *Marine Mammal Protection Act* of 1972 (MMPA) [44].

Administrated by the National Marine Fisheries Service (NMFS) and the Fish and Wildlife Service, it works for the protection of marine mammals from anthropogenic noise;

- The *Endangered Species Act* 1973 (ESA) [45].

It protects listed endangered species from possible acoustic injury or disturbance.

Following the appropriate normative in each country, prior to undertaking industrial marine operations that will generate high levels of noise, noise impact assessments must be conducted to predict the potential effects of such activity. These assessments include the prediction of sound signal propagation from the source in the specific environment, to estimate what levels will be received at different distances. However, the prediction of underwater noise levels from offshore and nearshore industrial operations such as pile driving or seismic surveys is a complex task which can have a very high computational cost. This is why the predictions are usually made by a combination of numerical methods for underwater acoustics and extrapolation from measurements [46]. Further research is therefore needed, and this project aims at offering better tools for the prediction of sound levels from industrial activities, specifically for the peak pressure level, as explained next.

### 1.1.3 Control parameters

Different metrics can be used to evaluate the intensity of an acoustic signal and currently there are no common international standards for it. The scientific community is working towards it through different groups. For instance:

- The Subcommittee SC 3 of the Technical Committee ISO/TC 43 is working on standard ISO/CD 18405 focused on terminology used in underwater acoustics.
- TNO suggested, based on previous ISO standards, a standard for the physical quantities involved in the measurement and monitoring of underwater noise [47]. This standard was also recommended in the report prepared to support the implementation of MSFD Descriptor 11 relative to underwater noise, for the goal of achieving the GES [48].

Therefore, until an international standard is formulated and no ambiguity occurs with metrics, it is very important to select appropriate metrics and provide a good definition of the terminology and units employed.

Attending to the general practice, the units more commonly used in the context of impact assessment are the sound pressure level (*SPL*), the sound exposure level (*SEL*) and the peak pressure level ( $L_{peak}$ ) [10, 49, 50]. *SPL* (defined in Eq. 1.1) is the root mean square (RMS) pressure expressed in dB re 1  $\mu\text{Pa}$ , and it is a common measure used in this context. However, it is not an appropriate characteristic to control the impact of impulsive signals because the signal is not uniformly distributed with time. Moreover, the time window to calculate the average is not standardized so it will likely be different in each case, making the comparison of levels from different studies very difficult [51]. Furthermore, *SPL* is less robust than *SEL* in terms of modelling when the modelled environment differs from the real scenario [52].

$$SPL = 10 \log \left( \frac{1}{T_a} \int_0^{T_a} p(t)^2 dt \right) \text{ dB re } 1 \mu Pa^2. \quad (1.1)$$

where  $T_a$  is the averaging time.

$SEL$  is the square of the instantaneous sound pressure  $p(t)$  integrated over the duration  $T$  of an impulsive signal and represented in dBs relative to  $1 \mu Pa^2 \cdot s$  (Eq. 1.2). In reality, transient signals are commonly mixed with background noise, so that it is impossible to absolutely define the signal start time and duration. For this reason, the signal duration  $T$  is commonly defined as a time interval  $[t1, t2]$  containing 90% of signal's energy, where 5% of cumulative signal and noise energy before and after signal's arrival are ignored. It is a good measure of the energy of transient signals in the context of noise impact assessment.

$$SEL = 10 \log \left( \int_0^T p(t)^2 dt \right) \text{ dB re } 1 \mu Pa^2 s. \quad (1.2)$$

Finally, for transients, one of the most appropriate measures (together with  $SEL$ ) is the peak-to-peak sound pressure level [10, 53, 54] or peak pressure level  $L_{peak}$  (zero-to-peak sound pressure level) defined in Eq. 1.3.  $L_{peak}$  is the maximum instantaneous sound pressure level of an acoustic signal  $p(t)$  represented in dBs relative to  $1 \mu Pa$ .

$$L_{peak} = 20 \log(\max |p(t)|) \text{ dB re } 1 \mu Pa. \quad (1.3)$$

Peaks in an acoustic signal can have different effects on marine animals such as causing changes in their behaviour and even damages to their hearing systems at short distances; so they need to be predicted. It is also important to predict the peak pressure levels at longer distances for pollution control and regulation. However, as it is explained in Chapter 2, predictions of peak levels with the available models of underwater sound propagation are much less accurate than predictions of the sound exposure, which is proportional to the signal energy.

Statistical techniques like Monte Carlo methods can be useful, but their computational cost is too high for long range problems. An alternative method is therefore required, and this is the main goal of this project.

## 1.2 Scope and objectives

The object of this research was anthropogenic impulsive acoustic signals of low frequency, radiated in underwater environments. Particularly, signals from offshore seismic surveys were chosen to be studied and modelled, given their presence and importance in the context of oil and gas exploration. The methodological approach was applied afterwards to offshore impact pile driving signals.

This research is focused on the Australian marine environments, in light of the high number of the mentioned activities carried out offshore and the access to data from some of them. However, given the diversity of the Australian environments studied, the results of this project will be applicable to other environments with similar characteristics worldwide.

The main objectives of this research were:

1. Improving the theoretical understanding of changes in the peak pressure that occur as an impulsive signal propagates in a randomly fluctuating underwater sound channel in the ocean.
2. Developing a method to predict peak pressure values and/or their probability distribution as a function of range.
3. Verifying the results of the model by comparison with measured data.

The specific tasks undertaken to attain these objectives, which represent the original contributions to the field, are presented through the following chapters and summarised in the conclusions (Chapter 9).

This page intentionally left blank

# Chapter 2.

## Theoretical Background

“Realize that everything  
connects to everything else”  
- Leonardo da Vinci

**T**he aim of this chapter is to provide the technical context where the project is framed.

Firstly, the basic characteristics of sound propagation in fluctuating oceans are presented. This part does not intend to fully cover the theory on sound fluctuations, as that is out of the scope of the project, but to offer a general description of the theory of wave propagation and fluctuations in random media connecting with the difficulties encountered when applied to the peak pressure of an underwater sound signal. Secondly, the main characteristics of airgun array signals and pile driving signals are explained, as they are the sources studied in this project. Thirdly, the main underwater sound propagation models currently used by the scientific community are described and their limitations are explained. Finally, the difficulties associated with the prediction of the spatial and temporal variations of the peak pressure level are discussed in comparison with the prediction of the sound exposure level.

### 2.1 Sound propagation in a fluctuating ocean

Sound waves experience different phenomena during propagation in the ocean, which affect the signal's travel paths, amplitude, and phase, as simplistically illustrated in Fig. 2.1. Most of these phenomena are well known and can be modelled using some approximations with the current underwater

acoustic propagation models [55-58]. However, some effects experienced by the signal, such as amplitude fluctuations, can be difficult to predict.

Fluctuations in amplitude can be caused by temporal variations in the acoustic environment, such as moving inhomogeneities in the water column [58], the relative motion of the source and receiver, and changes in the sound speed profile in the water column as a consequence of ocean dynamics. Fluctuations resulted from dynamics of the ocean can include large scale, mesoscale and small scale features [56]. Large scale effects are those produced by the wind stress or changes in the density of water, for instance, currents like the Antarctic Circumpolar Current and the Gulf Stream [59]. Some examples of mesoscale features are internal waves [60], tides, fronts, and eddies [56]. Small scale features, such as small-scale turbulences produced by the influence of the atmosphere [57], or fine ducting near fronts [61] can also be very significant from an acoustical point of view. Fluctuations can also result from changes in the sound speed profile over a rough seafloor.

All these fluctuations can produce significant difficulties in different applications that rely on underwater sound transmission, such as underwater acoustic communications [62].

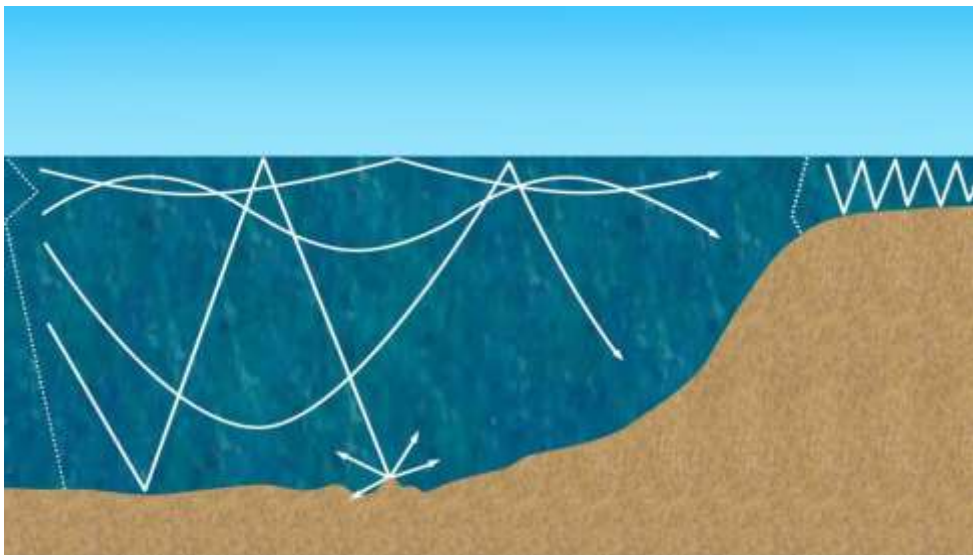


Fig. 2.1: Possible sound propagation paths underwater (straight lines). Dotted lines represent two different sound speed profiles.

The theory of wave propagation and fluctuations in random media has been broadly studied (e.g. [60, 63, 64]). When applied to the propagation of sound in the ocean, this theory is developed in terms of different regimes regarding the saturation of fluctuations: unsaturated, partially saturated, and saturated [60]. Two parameters are used in [60] to determine the regime: the diffraction parameter  $\Lambda$ , and the strength parameter  $\Phi$ , in form of  $\Lambda$ - $\Phi$  space. The former is the weighted average of the ratio of the first vertical Fresnel zone radius to the vertical correlation length of sound speed fluctuations, whereas the latter is the RMS phase variability and it is used to estimate the strength of fluctuations ( $\Phi^2$ ). In a very simplistic way, an unsaturated regime is that where geometrical approximations are valid and fluctuations are not very strong, whereas a saturated regime is that where strong fluctuations are present. Determining the regime is very important in many cases, but difficulties were found to determine it in some studies (e.g. [65]). Recently, the concept of the  $\Lambda$ - $\Phi$  diagram was reformulated to offer a more precise delimitation between saturated and unsaturated regimes [66]. The diagram is commonly used when sound speed fluctuations are mainly caused by internal waves, which are not directly considered in this project. For that reason, it is briefly described here but it was not used to calculate fluctuations of the sound signals analysed in this study.

Despite the development of the theory of wave propagation and fluctuations in random media, a general statistical theory of fluctuations in the ocean sound channel cannot be formulated, because this would require realistic stochastic models of the acoustic environment including its boundaries, as well as predictions of the effects of random changes in all environmental parameters on the acoustic transmission. However, a generalised theory can be developed under certain conditions of underwater sound propagation.

In multipath underwater sound propagation, sound waves propagate refracting in the water column and reflecting from the sea surface and seafloor following multiple paths. Scattering affects the amplitude and phase of the received sound signal and the randomness of the phase is more significant than that of the amplitude [64]. If the sound field at the receiver is formed by a large number of statistically independent signals scattered with random phase from various scattering features, then this field tends to be fully randomized. This is an

effect of saturated transmission scintillation [67]. The sound field can then be represented by a complex variable where variations of the real and imaginary components follow a normal distribution, the phase is uniformly distributed, the amplitude is Rayleigh distributed [68], and the instantaneous intensity is exponentially distributed [69].

This was discussed by Dyer in his study of the statistics of sound transmission fluctuations in the ocean [64]. In [67], some of the analysis presented in [64] and [68] was extended to take into consideration the time-bandwidth product  $\mu$  of the transmitted signal. The values of the transmission loss ( $TL$ ) mean and  $TL$  standard deviation presented in [64] were found to be valid for an instantaneous measurement when  $\mu = 1$ . However, in the majority of underwater acoustic applications the sound intensity is averaged over time and/or certain frequency band, so that  $\mu$  is larger than unity. The gamma distribution is shown in [67] to be an appropriate model of sound intensity fluctuation in a fully randomised field when  $\mu \gg 1$ . Consequently, fluctuations of the sound intensity level expressed in logarithmic units can be modelled by an exponential-gamma distribution. An agreement with this model at  $\mu \gg 1$  has been observed in later studies (e.g. [69]). The analysis in [67] was extended in [70] by including the frequency correlation of broadband signals, using coherence theory.

Despite a vast number of studies on fluctuations of underwater sound, some of them referred to before, the references to the influence of scattering from the underwater sound channel boundaries and sound speed fluctuations in the water column on the spatial decay of the peak pressure in broadband impulsive signals and the predictions of its fluctuations are very scarce. Studies conducted using airgun signals showed that the peak pressure amplitude is affected by seafloor characteristics [71, 72]. Regarding the influence of the sea surface on the peak pressure, the effect of the wave height on the peak pressure in a low-frequency range is considered in [73] and the dependence of fluctuations on the angle of incidence after surface reflection is described in [74]. Finally, in a study on travel time and intensity fluctuations of pulses due to physical oceanographic characteristics observed in the Asian Seas International Acoustics Experiment

(ASIAEX) [75], the authors found that the peak intensity of the transmitted impulsive signal was dependent on several factors, such as the movement of the receive array relative to a spatial mode interference structure, energy loss, and changes resulting from pulse spreading at a fixed energy. Moreover, they noticed that the peak intensity showed higher temporal variability than the average intensity in the pulse, which was expected as a result of averaging. Finally, in [76] the authors analyse fluctuations of the peak intensity of seafloor backscatter signals, which is used in some multibeam sonar systems as a measure of backscatter strength. Their measurements and theoretical analysis show that fluctuations of peak backscatter amplitude tend to be extreme value distributed at oblique angles of incidence where the footprint of the beam on the seafloor is significantly larger than the instantaneous insonification area.

Chapter 7 of this thesis presents an approach to model peak pressure fluctuations of broadband impulsive signals, following a similar approach described by Dyer [64] and Makris [67], but using the extreme value theory.

## **2.2 Sound from industrial activities**

A high proportion of the noise generated in marine industrial operations is made of low frequency (LF) impulsive signals of high energy. The frequency band of these signals overlaps the hearing range of some marine animals and, because of the lower sound attenuation at low frequencies, they propagate over longer distances, increasing the range of potential damage.

Two different kinds of signals were studied in this project: signals produced in offshore seismic surveys using airguns arrays and signals radiated from offshore pile driving operations. The project was mainly focused on the signals from the former group. The approach used with it was applied afterwards to the latter group.

This section briefly describes the main characteristics of both types of signal.

### 2.2.1 Signals from offshore seismic surveys using airguns

Oil and gas companies undertake offshore seismic surveys to find natural underwater reservoirs of oil and gas. For that purpose, a seismic vessel tows an airgun array close to the sea surface that acts as an acoustic source of high-intensity impulsive sound. A number of hydrophone streamers of several kilometres length also towed behind the vessel close to the sea surface receive the signals reflected from the interfaces between different sediment layers in the seabed (see Figs. 2.2 and 2.3).

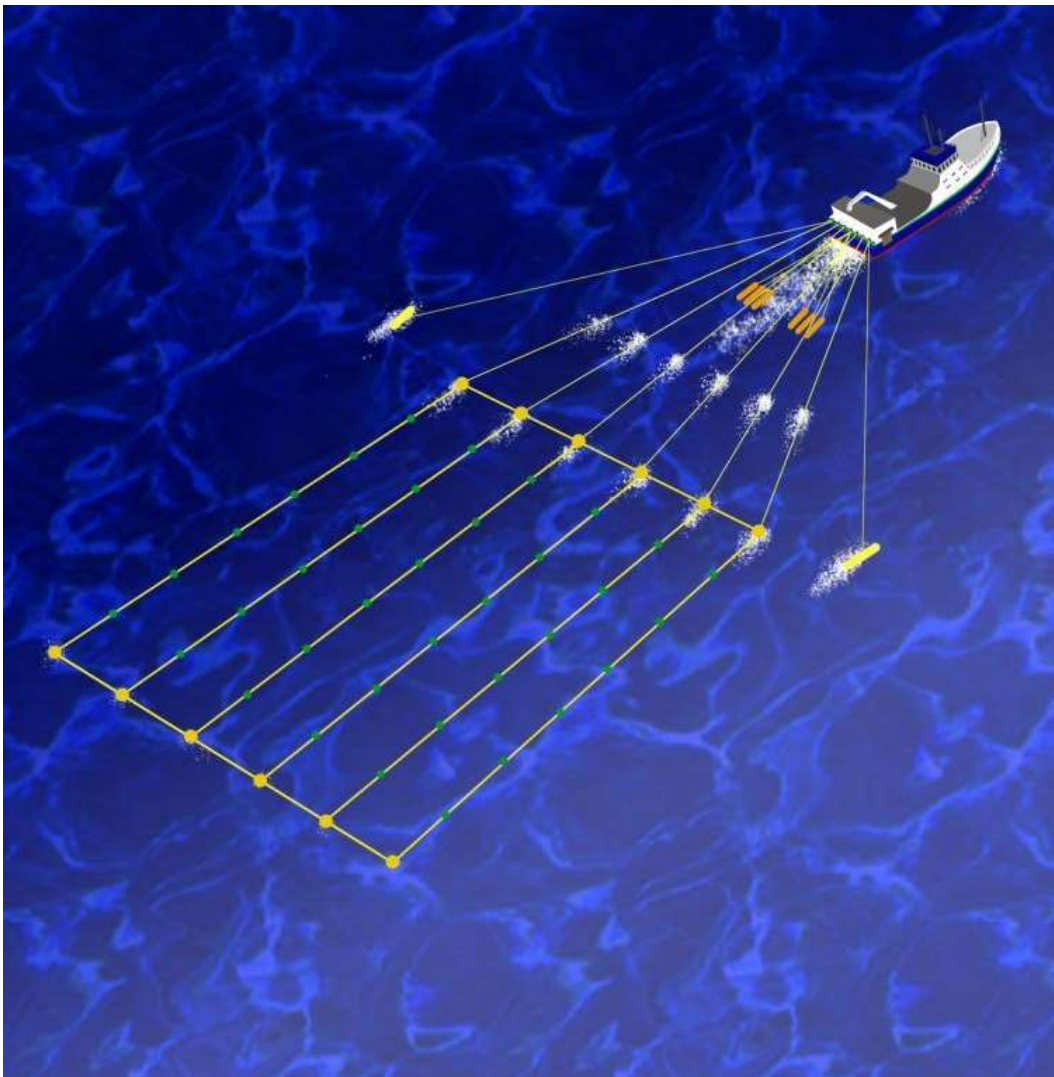


Fig. 2.2: Airgun array (short thick orange lines) and hydrophone array (long yellow lines with green dots) towed from vessel.

Hydrophones moored close to the seafloor are also used in some cases to receive the signals. The airgun signals can also be used in geoacoustic inversion studies [77]. The signals produced by airguns are impulsive, in contrast to continuous signals from the sources of resonant type also used for sub-bottom profiling [78]. These are signals of high intensity (peak levels of up to 255 dB re 1  $\mu$ Pa at 1 m [79]). They are broadband signals with most of the energy concentrated below 200 Hz, which is generally the frequency required for imaging the geological subsea formations. The spectrum of the propagated signal varies with distance and this variation depends on the environment [58].

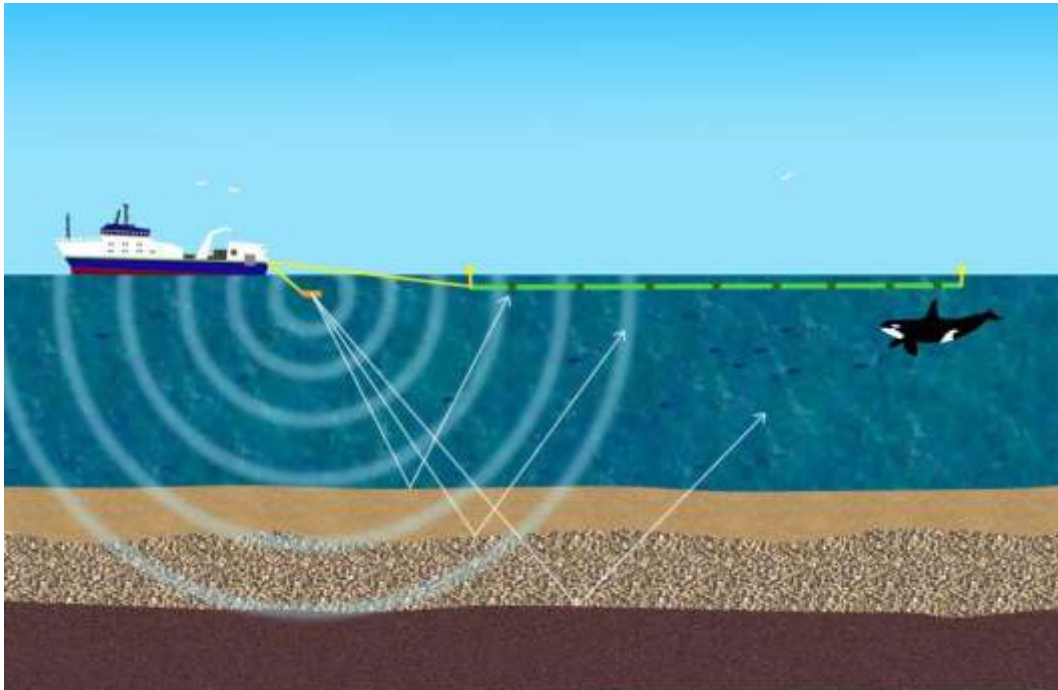


Fig. 2.3: Schematic view of a seismic survey. Sound signals are emitted from the airgun array (short orange line) and received on the hydrophone array (long green lines) after reflection from different sediment layers.

### 2.2.1.1 Airguns

Airguns are electromechanical devices that generate an intense impulsive acoustic signal by releasing air or nitrogen compressed at high pressure in a chamber, into the water. They are characterized by the volume of air expelled, which typically ranges from 30 to 800 in<sup>3</sup> [80]. The air is released as a bubble that

expands very quickly until the pressure reaches the value of the hydrostatic pressure of the surrounding water. However, the pressure continues reducing its value due to inertia. The difference in pressure produces the collapse of the bubble, and then a new expansion, producing a succession of positive and negative pulses. These oscillations repeat several times, with lower amplitude each time [81]. The typical signature of an airgun signal is similar to that of an underwater explosion. Figure 2.4 illustrates an ideal sound signal generated by these two types of underwater sound source. The signature of the airgun signal has typically lower source level and lower maximum frequency, but it is better controlled in terms of the signal intensity and firing rate [82]. The initial shock wave has the highest amplitude, and then the amplitude decreases with each bubble pulse.

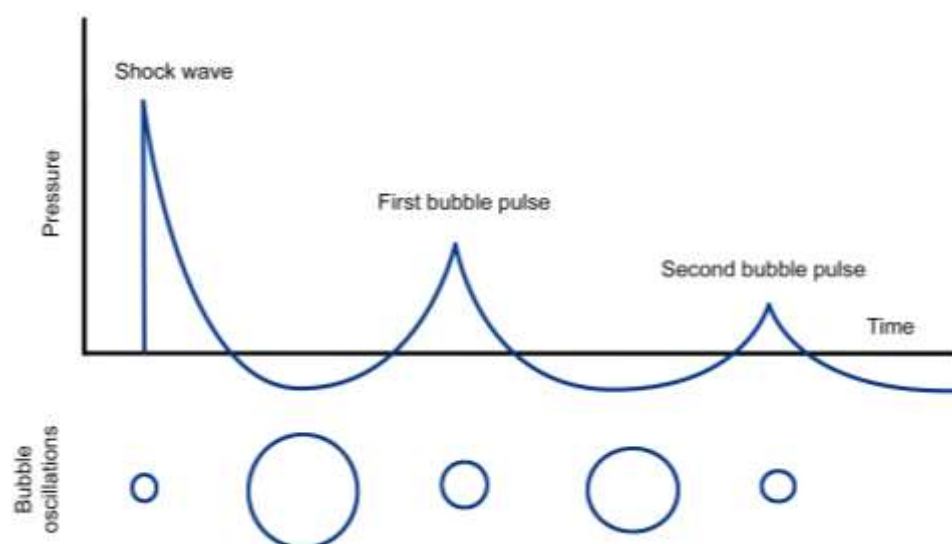


Fig. 2.4: An idealised illustration of sound signal generation by an underwater explosion or airgun.

Figure 2.5 illustrates the sound pressure waveform from a single airgun simulated at large distance vertically below the gun in deep water, where the absolute pressure value was scaled back to 1 m from an equivalent point source centre assuming spherical spreading loss. The primary pulse is the direct arrival of the shock wave, followed by its reflection from the sea surface with an opposite amplitude, and then by the bubble pulses.

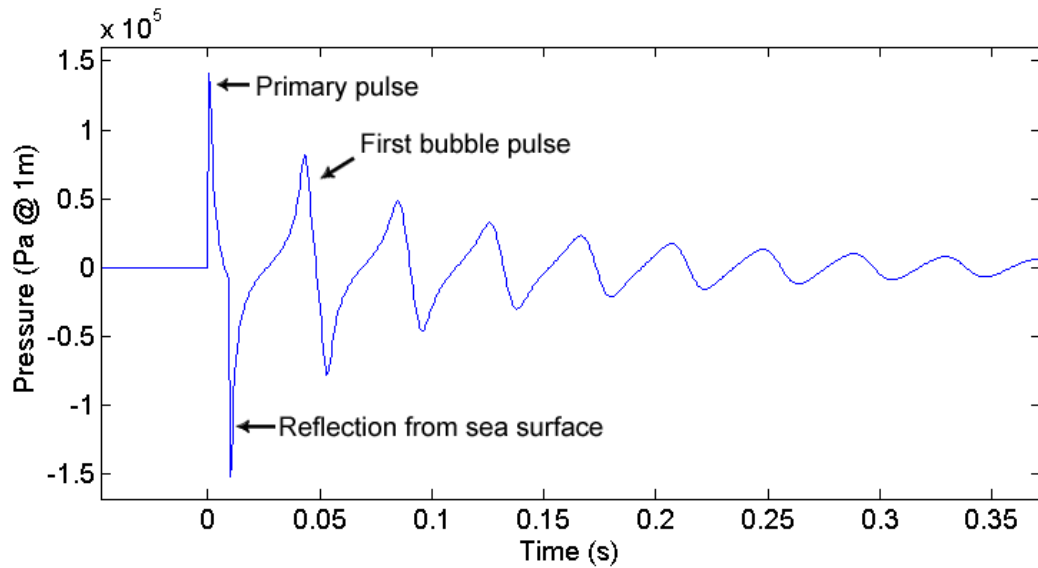


Fig. 2.5: Sound pressure waveform from a single airgun simulated at long ranges in the vertically downward direction, and then reduced to 1 m from the centre of the source. The primary pulse is the direct arrival of the shock wave, followed by its reflection from the sea surface with negative amplitude, and then by the bubble pulses.

### 2.2.1.2 Airgun arrays

Airgun arrays (see example depicted in Fig. 2.7) are much more commonly used as a seismic source than single guns for three main reasons.

The first reason is that using guns with different volumes will significantly reduce the overall effect of the bubble oscillations produced by each single gun in comparison with the primary shockwave impulse. The period of these oscillations is different for airguns of different volume and therefore, when superimposed, the acoustic signals due to these oscillations from the different airguns partly cancel each other (see example in Fig. 2.6).

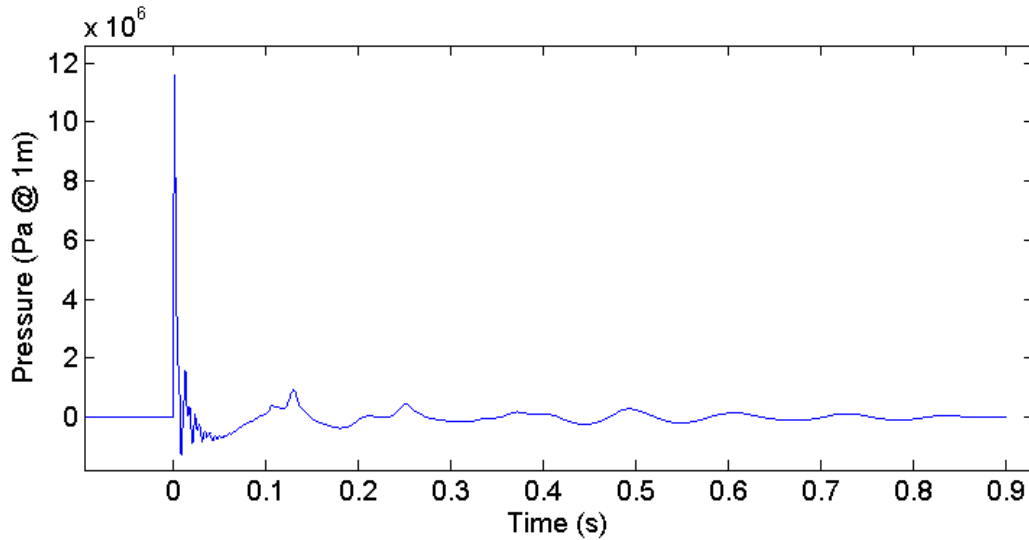


Fig. 2.6: Sound pressure waveform of a 4230 cui airgun array simulated for an equivalent point source at 1 m from its centre in boundary free space (i.e. no reflection from the sea surface in contrast to the waveform shown in Fig. 2.5).

The second reason is that an airgun array produces a signal of significantly higher amplitude than a single gun of the same total volume.

The third reason is that using an array of airguns produces a directional signal emitted towards the seafloor, while a single gun is not directional.

Most arrays have total volumes between 1500 and 8000 cui. They typically consist of 3-6 subarrays, each one having 4-8 guns in a linear arrangement [80], forming a horizontal planar array.

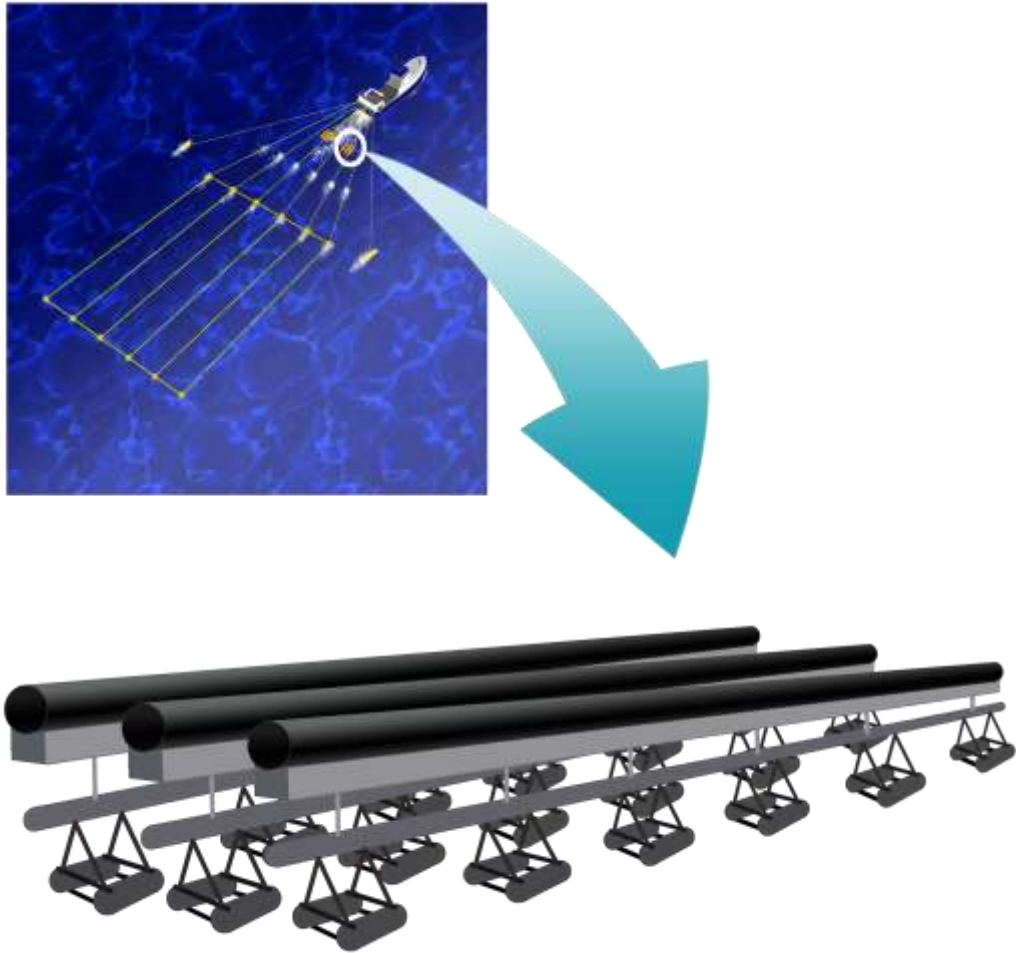


Fig. 2.7: Airguns in array.

### 2.2.1.3 Modelling of sound emission from airguns and airgun arrays

Source models are necessary to understand the process of sound emission and to calculate the signal waveform and spectrum at a reference distance from the source. The simplest model of an airgun signature is based on the free-bubble oscillation model [83]. This model considers a free bubble (spherical air bubble in an infinite water environment) with pressure and volume oscillating between the chamber's initial pressure and volume and the minimum pressure, when the

volume is maximum. The oscillations repeat with decaying amplitude until all the initial energy is radiated as sound or converted to heat and dissipated. According to an idealised model of an airgun [83], the peak acoustic pressure is proportional to the cube root of the chamber volume. This model predicts correctly the dependence of the bubble oscillation period on pressure and volume, reformulated later in [84]. However, the model overestimates the amplitude of the primary pulse compared to experimental data.

Using this theory as the start point, Johnson [85] developed a simple model for the airgun bubble which gives results similar to other previous models, but still showed disagreements with measured data. The modelled amplitude was much higher than the measurements, and the damping factor was underestimated, so the decay of the modelled signal was much slower. However, the model is useful to understand the behaviour of the bubbles. In this model, the bubble is considered a sphere with pressure  $p_w$  at the wall. The bubble motion is given by Eq. 2.1, where  $r$  is the radius of the bubble,  $\rho$  is the density of water, and  $c$  is the sound speed in the water.

$$\frac{d^2 r}{dt^2} - \frac{p_w}{\rho r} + \frac{3}{2r} \left( \frac{dr}{dt} \right)^2 - \frac{1}{\rho c} \frac{dp_w}{dt} = 0. \quad (2.1)$$

The pressure at a distance  $R$  from the centre of the source with a particle velocity  $v = (dr/dt)$  at the wall is given by Eq. 2.2, assuming  $R \gg r$ .

$$p(R) = \frac{r}{R} \left( p_w + \frac{\rho v^2}{2} \right). \quad (2.2)$$

The acoustic pressure at the bubble wall is calculated as a difference between the absolute air pressure inside the bubble,  $p_a$ , and the hydrostatic pressure in surrounding water  $p_0$  (Eq. 2.3). The absolute air pressure in the bubble is given by Eq. 2.4 where  $r_0$  is the radius of the bubble when the pressure is  $p_0$ , and  $\gamma$  is a thermodynamic parameter.

$$p_w = p_a - p_0, \quad (2.3)$$

$$p_a = p_0 \left( \frac{r_0}{r} \right)^{3\gamma}. \quad (2.4)$$

With the substitution of Eq. 2.5 (obtained by differentiation of Eq. 2.4) into Eq. 2.1 the problem can be solved numerically using a standard differential equation solver for initial value problems [86].

$$\frac{dp_w}{dt} = \frac{-3\gamma p_a v}{r}. \quad (2.5)$$

To correct the differences observed between the predicted results from this model and measurements, Duncan [87] modified it and obtained a more accurate signal model for sound emission by real airguns. Firstly, the damping factor was increased to match the bubble oscillation decay rate with the measured results. Secondly, a finite rise time for the first pressure pulse was introduced to correct for the differences observed when comparing with the measured waveform.

This model of a single airgun was used to construct the CMST's sound emission model for airgun arrays including coupling between different airguns in the array. In this model, the ambient pressure was changed to include the pressure of all the airguns in the array and the pressure from the ghost signals (surface reflection).

The model is calibrated for each array by scaling the amplitude of the far-field waveform (correcting for spherical spreading) after comparison with an example waveform provided by the seismic contractor. The sample waveform is obtained via simulation with the software Nucleus [88] or Gundalf [89], both of them calibrated with measured data. The calculations are made for distances far enough from the source to meet the far-field criterion.

In the CMST's model the far-field pressure at the receiver for each airgun is calculated using Eq. 2.6 [90], where  $p$  is the pressure of the source at 1 m,  $t$  is the time,  $R$  is the distance from the source to the receiver,  $R'$  is the distance from the

ghost source to the receiver,  $c$  is the speed of sound in water, and  $\Gamma$  is the sound reflection coefficient at the surface ( $\Gamma = -1$  for pressure released surface).

$$p_{rec}(t) = \frac{1}{R} p\left(t - \frac{R}{c}\right) + \frac{\Gamma}{R'} p\left(t - \frac{R'}{c}\right). \quad (2.6)$$

As an example, Fig. 2.8 shows the testing of the model for an airgun array designed for a real seismic survey, by comparing the waveform predicted with CMST's model, to the reference waveform provided by the seismic contractor, both for the vertically downward direction. The agreement is very good in general.

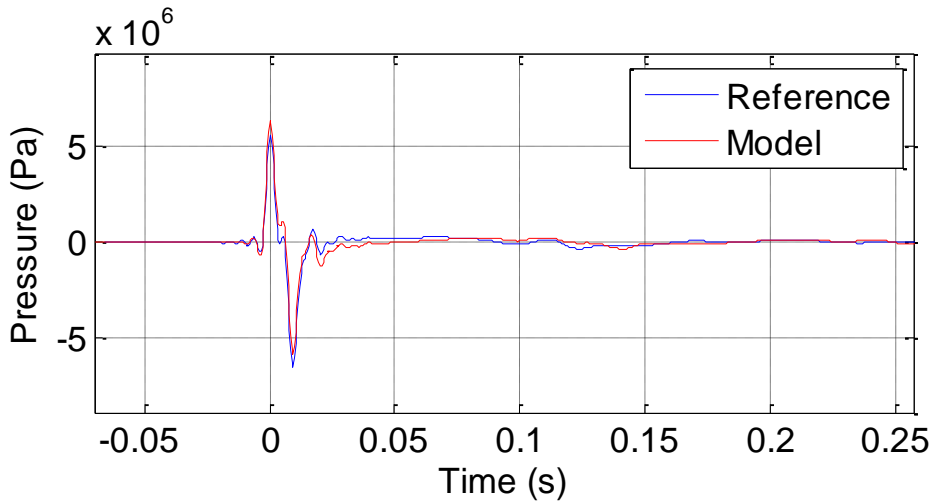


Fig. 2.8: Waveform simulated with CMST's airgun model (red) compared with the measured (reference) waveform of the array (blue).

## 2.2.2 Signals from offshore impact pile driving

Impact pile driving occurs during many types of offshore construction, including offshore wind farms, oil and gas platforms, and ports.

A pile, vertical or slanting, is driven into the seafloor after consecutive high-energy impacts with a hammer (see Fig. 2.9). The diameter of the hammer ranges between 0.5 m to 6.5 m depending on the size of the pile [91]. For large piles such as those installed for offshore windfarms in the North Sea, the impact energy of

the hammer (which depends on its mass and velocity) reaches values around 2000 kJ [91]. This energy and the pile cross-section area, are directly related to the intensity of the sound transmitted underwater.

The peak pressure of the emitted underwater sound is governed by the radial deformation of the pile resulting from the impact and propagating downwards. This radial deformation emits a pressure wave which propagates as a Mach cone, due to the difference of the propagation velocity of deformation along the pile and in the surrounding water [92]. This effect has been observed not only in simulations of the generation and propagation of noise from pile driving, but also in experimental measurements of impact pile driving noise using a vertical array [93].

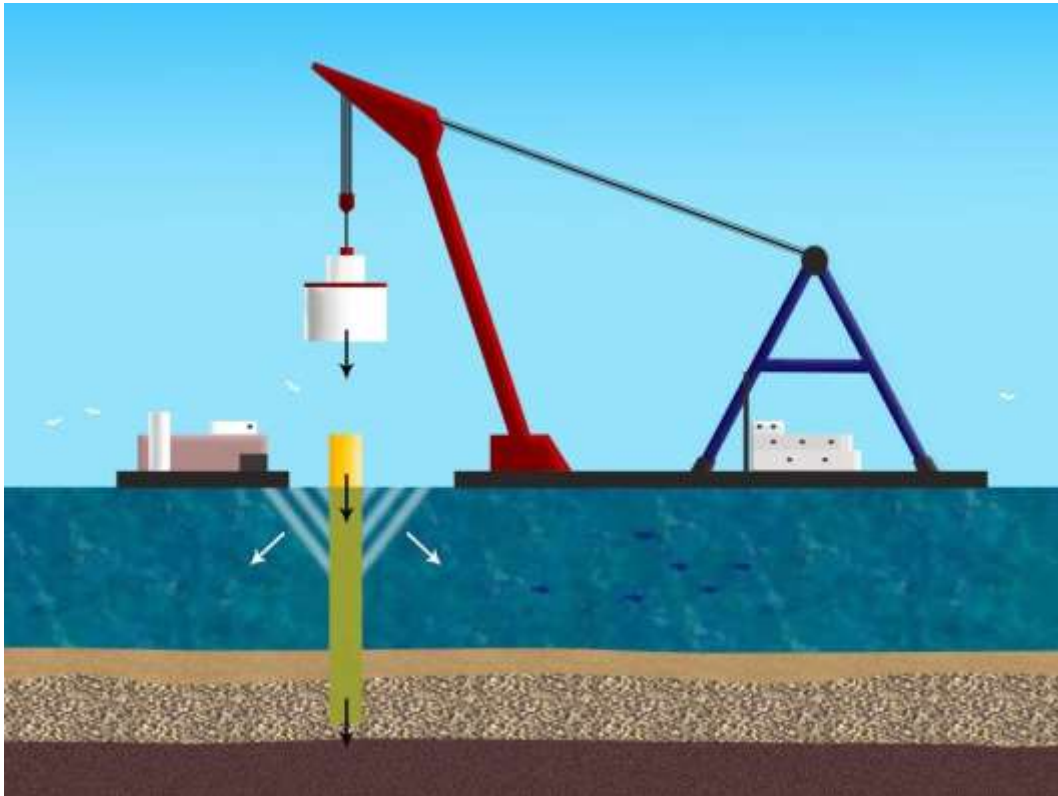


Fig. 2.9: Illustration of vertical pile being driven into the seafloor by hammer impacts and corresponding emission of noise in the water.

### 2.2.2.1 Modelling of sound emission from pile driving

Predicting the noise radiated from pile driving has been studied during the last years but, given the complexity of the problem, there are no closed-form analytical solutions.

The workshop COMPILER was organized in Hamburg in June 2014 with the goal of setting a benchmark case to validate and compare seven different numerical models that have been developed in various institutions worldwide. An article including the benchmark case, the description of the models, and the comparison of results was accepted for publication at the IEEE Journal of Ocean Engineering [94]. Models were classified into near field and far field models, but this section focuses exclusively on the first group regarding sound emission. Most models solved an axial-symmetric problem of sound emission by a cylindrical pile using the Finite Element Method (FEM) in the frequency domain, except for one model where a Finite Difference Method (FDM) was used in the time domain. Different software packages were used, including PAFEC-FE [95], ABAQUS and COMSOL. The general procedure involved using FEM for the pile and the surrounding media (water and ground), which were assumed to be fluid. The interaction between the pile, water and ground was modelled by bidirectional coupling; energy loss due to the deformation of the soil and the friction with the pile was accounted for by introducing additional damping in the pile material embedded into the ground. Then, different propagation models were used for predictions at long ranges. Almost all models using FEM obtained similar results for the waveform predicted at several distances, and also for the value of  $SEL$  and  $L_{peak}$ . The model using FDM underestimated secondary arrivals, which led to somewhat lower values of the received signal energy.

## 2.3 Underwater sound propagation modelling

Modelling of underwater sound propagation aims at predicting the sound field for a certain source and environment. Frequency-domain analysis is commonly the preferred option to calculate it. Some of the reasons to choose the

frequency domain are the frequency dependence of sound attenuation and scattering at the seabed and sea surface, and the fluctuations of underwater sound signals due to the variability of the ocean. The propagation model chosen for modelling is run on a frequency grid to obtain the transfer function  $h(r, z, \omega)$  for a distance  $r$ , depth  $z$  and frequency  $\omega$ . Then, using the source spectrum  $S(\omega)$  and Fourier synthesis, the waveform of the signal at the time  $t$ ,  $p(r, z, t)$ , can be obtained from Eq. 2.7. This was the procedure used in this study.

$$p(r, z, t) = \frac{1}{2\pi} \int_{-\infty}^{\infty} S(\omega) h(r, z, \omega) e^{-i\omega t} d\omega. \quad (2.7)$$

The accuracy of prediction of the received signal is highly dependent on the knowledge of environmental parameters. Since a fully realistic description of the environment, including the temporal variability of the ocean is not achievable, there are constraints to the accuracy of the transmission models. Nevertheless, a reliable model with appropriate approximations can provide reliable predictions, if parameters of the underwater sound propagation environment including the water column and seabed are known to a reasonable degree.

Some of the environmental parameters that generally need to be known are the parameters of the seafloor that have an influence on sound reflection from the bottom, known as the geoacoustic model of the seafloor. There can be exemptions where the seafloor has a minor effect on long-range sound propagations, such as the case where a source and a receiver are placed at the axis of the underwater sound (SOFAR) channel in deep water. Otherwise, the seafloor must be carefully modelled. When low-frequency (LF) signals are propagating, the modelling must be done up to deep layers in the seafloor because these signals will penetrate deeply, unlike in high-frequency (HF) problems where only the top few meters of the sediment are relevant. It is necessary then to identify the shape and thickness of the layers and what sediments or rocks form them [96]. As explained in the cited work, a complete geoacoustic model must contain the values of the following parameters for each layer of the seafloor, including their variation with range: thickness  $h$ , density  $\rho$ , compressional wave speed  $c_p$ , shear wave speed

$c_s$ , compressional wave attenuation  $\alpha_p$ , and shear wave attenuation  $\alpha_s$ . These values can be obtained by using sediment probes, boreholes, or by geoacoustic inversion. Those procedures are not covered in this project since it is out of its scope. For more information about the theory behind geoacoustic inversion and the capabilities of these techniques, the reader can refer to [97] and [98] respectively. Additionally, some parameters can be calculated from others using the relations between them. For instance, knowing the dispersion relation between the phase speed and attenuation of the compressional and shear waves, and given the values of the other parameters in the corresponding equations, one can be inferred from the other [99, 100].

The bathymetry of the seafloor is a very important element to model the sound transmission. Simulating the sound propagation in range dependent environments (like most real scenarios and two out of the three sites analysed in this project) can be a very complex task and it will affect the choice of the sound propagation model. In these environments, for instance, the effects of mode coupling are very significant [101]. Therefore, using the adiabatic mode approximation will not always give good results. Characteristics of the seafloor are also especially important for accounting for scattering effects [102, 103], but can be difficult to quantify, because of their stochastic nature [104]. Chaotic behaviour can also be found in range dependent acoustic problems when the ray paths are very sensitive to initial conditions, leading to exponential divergence of paths that were initially very proximal to each other [105, 106].

To conclude this section, modelling the propagation of underwater sound is a complex process with many variables linked to the sound source and the propagation environment. Their analysis allows us to choose a suitable propagation model, which will belong to one of the main group of models briefly described in the following sections.

### **2.3.1 Existing underwater sound propagation models**

There are a number of different underwater sound propagation models used by the scientific community. They are suitable for different problems and are

frequently classified according to the approximation employed to solve the Helmholtz equation for the sound pressure  $p$  (Eq. 2.8), where  $k_0$  is the reference wavenumber  $k_0 = \omega/c_0$ ,  $c_0$  is the reference speed of sound,  $\omega$  is the sound frequency, and  $n = c_0/c$  is the refraction index. This equation is the wave equation for a harmonic solution with the form of  $p = p_0 e^{-i\omega t}$ . The equation can also be written in cylindrical coordinates, and it is known as an elliptic wave equation (Eq. 2.9).

$$\Delta p + k_0^2 n^2 p = 0, \quad (2.8)$$

$$\frac{\partial^2 p}{\partial r^2} + \frac{1}{r} \frac{\partial p}{\partial r} + \frac{\partial^2 p}{\partial z^2} + k_0^2 n^2 p = 0. \quad (2.9)$$

The different approximations used to solve the wave equation lead to a general classification of models into five main groups: Parabolic Equation (PE) approximation models, Normal Mode (NM) models, Ray approximation models, Wavenumber Integration (WI) models, and discrete models. All of these model groups are described in detail in [56] and [55]. They have different applicability to environments of deep or shallow waters and also their suitability for high and low frequency signals is different (see page 139 in [56]). Choosing an appropriate model is crucial to obtain reliable results. The five types of models are briefly described in this section. The PE and NM models are explained with more detail given their higher relevance to this project.

There are several algorithms, software tools and interfaces developed for modelling the underwater propagation of sound, which are in general based on the models previously described. For example, The Centre for Marine Science and Technology (CMST) developed the Acoustic Toolbox User interface and Post processor (AcTUP) [107] which provides a menu-based user interface to a variety of underwater acoustic propagation codes.

### Parabolic Equation models:

Current parabolic equation models are based on a high-order energy conserving parabolic approximation of the originally elliptic wave equation (Eq. 2.9) [108-110]. Numerical models based on a PE approximation are most suitable for the problems where the environment is range-dependent and the frequencies are relatively low [56].

The derivation of the standard PE equation as presented in [111] starts by assuming a solution in the form of the product of an envelope function  $\psi(r, z)$  that varies slowly with range, and a range-dependent function  $\varphi(r)$ :

$$p = \psi(r, z) \cdot \varphi(r). \quad (2.10)$$

Then, replacing  $p$  in Eq. 2.9, two equations are obtained: a zero-order Bessel equation for the range-dependent component  $\varphi(r)$  (Eq. 2.11), and an equation for  $\psi(r, z)$  (Eq. 2.12).

$$\frac{\partial^2 \varphi}{\partial r^2} + \frac{1}{r} \frac{\partial \varphi}{\partial r} + \varphi k_0^2 = 0, \quad (2.11)$$

$$\frac{\partial^2 \psi}{\partial r^2} + \frac{\partial^2 \psi}{\partial z^2} + \left( \frac{1}{r} + \frac{2}{S} \frac{\partial \varphi}{\partial r} \right) \frac{\partial \psi}{\partial r} + k_0^2 n^2 \psi - k_0^2 \psi = 0. \quad (2.12)$$

The solution of the Bessel equation for outgoing waves is given by the Hankel function  $\varphi = H_0^{(1)}(k_0 r)$ . Using the asymptotic form of the Hankel function, we obtain:

$$\varphi \approx \sqrt{\frac{2}{\pi k_0 r}} e^{i \left( k_0 r - \frac{\pi}{4} \right)}. \quad (2.13)$$

Replacing now  $\varphi$  in Eq. 2.11 and using the paraxial approximation  $\partial^2 \psi / \partial r^2 \ll 2k_0 \partial \psi / \partial r$ , the standard PE equation is obtained (Eq. 2.14), where

the refraction index  $n = n(z, r, \theta)$  also depends in general on the azimuth angle  $\theta$ :

$$\frac{\partial^2 \psi}{\partial z^2} + 2ik_0 \frac{\partial \psi}{\partial r} + k_0^2 (n^2 - 1) \psi = 0. \quad (2.14)$$

The standard PE equation is valid for small grazing angles. A generalized PE equation can be obtained, if the paraxial approximation is not used (see Eq. 2.15):

$$\frac{\partial \psi}{\partial r} = ik_0 \left( \sqrt{n^2 + \frac{1}{k_0^2} \frac{\partial^2}{\partial z^2}} - 1 \right) \psi = 0. \quad (2.15)$$

PE equations were also derived for elastic media [110].

Different PE solutions use different numerical techniques, such as the split-step Fourier algorithm [111]. One example is the Range-dependent Acoustic Model (RAM) developed by Collins [109] at the Naval Research Laboratory. This model and its variants RAMS and RAMGeo use the split-step Padé solution. RAMS can be used with elastic seafloors and RAMGeo can model sound propagation over a stratified seafloor of multiple layers with the boundaries not necessarily parallel to the sea surface and to each other, with all of the layers supporting only compressional waves (fluid seafloor).

For the derivation of the split-step Padé solution, the operators  $Q$  and  $X$  are defined as (Eqs. 2.16 and 2.17):

$$Q = \sqrt{n^2 + \frac{1}{k_0^2} \frac{\partial^2}{\partial z^2}}, \quad (2.16)$$

$$X = Q^2 - 1. \quad (2.17)$$

The solution of the generalized PE equation for a range  $r + \Delta r$  is given by Eq. 2.18, where  $\sigma = k_0 \Delta r$ :

$$\psi(r + \Delta r) = ei\sigma^{(-1+\sqrt{1+X})}\psi(r). \quad (2.18)$$

The Padé approximation is given by Eq. 2.19, where  $n$  is the term of the expansion and the coefficients are given by Eqs. 2.20 and 2.21:

$$ei\sigma^{(-1+\sqrt{1+X})} \approx 1 + \sum_{j=1}^n \frac{a_{j,n}X}{1+b_{j,n}X}, \quad (2.19)$$

$$a_{j,n} = \frac{2}{2n+1} \sin^2\left(\frac{j\pi}{2n+1}\right), \quad (2.20)$$

$$b_{j,n} = \cos^2\left(\frac{j\pi}{2n+1}\right). \quad (2.21)$$

Replacing this approximation in Eq. 2.22 leads to the split-step Padé solution

$$\psi(r + \Delta r) = \psi(r) + \sum_{j=1}^n \frac{a_{j,n}X}{1+b_{j,n}X}\psi(r). \quad (2.22)$$

### Normal Modes models:

These models solve the cylindrical wave equation (Eq. 2.19) using separation of variables. The solution of the acoustic pressure is assumed to be of the form:

$$p = \psi(z) \cdot \varphi(r). \quad (2.23)$$

The sound pressure  $p$  in the cylindrical wave equation (Eq. 2.24) is replaced with its representation by Eq. 2.23, where the density  $\rho$  is dependent on depth and  $z_s$  is the depth of the source:

$$\frac{1}{r} \frac{\partial}{\partial r} \left( r \frac{\partial p}{\partial r} \right) + \rho(z) \frac{\partial}{\partial z} \left( \frac{1}{\rho(z)} \frac{\partial p}{\partial z} \right) + \frac{\omega^2}{c^2(z)} p = -\frac{\delta(r)\delta(z-z_s)}{2\pi r}. \quad (2.24)$$

After dividing by  $\psi(z) \cdot \varphi(r)$  Eq. 2.24 leads to Eq. 2.25:

$$\frac{1}{\varphi} \left[ \frac{1}{r} \frac{d}{dr} \left( r \frac{d\varphi}{dr} \right) \right] + \frac{1}{\psi} \left[ \rho(z) \frac{d}{dz} \left( \frac{1}{\rho(z)} \frac{d\psi}{dz} \right) + \frac{\omega^2}{c^2(z)} \psi \right] = 0. \quad (2.25)$$

The summation in Eq. 2.25 will be zero if each term equals each other with opposite sign. Given that the first term of the summation is a function of range  $r$ , whereas the second member is a function of depth  $z$ , the only way the summation can be equal to zero is if each term is equal to a constant, denoted as  $k_m^2$ , with opposite signs. Thus, the equations obtained are the range equation and the Sturm-Liouville modal equation, where the eigenfunction  $\psi_m(z)$  of the equation are mode shapes, and the eigenvalues  $k_m^2$  are modal wavenumbers:

$$\begin{aligned} \frac{d^2\varphi(r)}{dr^2} + \frac{1}{r} \frac{d\varphi(r)}{dr} + k_m^2\varphi(r) &= 0, \\ \rho(z) \frac{d}{dz} \left( \frac{1}{\rho(z)} \frac{d\psi_m(z)}{dz} \right) + \left( \frac{\omega^2}{c^2(z)} - k_m^2 \right) \psi_m(z) &= 0. \end{aligned} \quad (2.26)$$

Solving the known eigenvalues problem (e. g. ref. [55]),  $p(r, z)$  can be expressed as a some of mode functions  $\psi_m(z)$  multiplied by the Hankel function of first kind:

$$p(r, z) = \frac{i}{4\rho(z_s)} \sum_{m=1}^{\infty} \psi_m(z_s) \psi_m(z) H_0^{(1)}(k_m r). \quad (2.27)$$

The solution given by Eq. 2.27 is valid only for range independent axisymmetric scenarios, but it can be extended to range dependent scenarios by calculating the modes at different distances and then linking the amplitudes of the modes at one cross-section of the propagation path to the amplitudes at the other cross-section at a larger distance. There are two methods to relate the mode amplitudes, the *mode coupling* method, and the *adiabatic approximation* method. The former accounts for energy exchange between different modes during

propagation, and models using this method are known as *coupled mode (CM) models*. The latter considers that the energy of each mode is transferred only to the same mode in the next cross-section of the environment, but not between modes. The models using this approximation are known as *adiabatic mode models*, and they can be used in underwater sounds channels varying slowly with range where the mode-coupling terms can be assumed to be negligible [56].

### **Ray approximation models:**

These models are based on geometric acoustics. For the Helmholtz equation, a solution based on the product of an amplitude function and a phase function is used. The separation of real and imaginary terms in the Helmholtz equation and the use of geometrical approximation lead to the eikonal equation and transport equation.

These models are efficient in deep water problems, but can be also used for shallow water environments at high acoustic frequencies, when the acoustic wavelength is much smaller than water depth. These models were not used in this project, given that the signals studied have most of their energy in a low frequency range.

### **Wavenumber Integration method:**

This method is similar to the method used to derive the solution of the Helmholtz equation using a NM model, but changing the way the integral is evaluated. The main limitation of the method is that it is applicable primarily to range independent environments, in order to obtain integral representations in each layer using boundary conditions in all of them. There are some variants of the WI method which are applicable to range dependent scenarios [112], but they are computationally expensive. Therefore, models using this method were not used in this project, as some of the environments studied were highly range dependent.

## Finite Difference and Finite Element Methods:

These are two methods based on discretization of the differential wave equation with boundary conditions. The Finite Difference Method (FDM) discretizes the wave equation by substituting the differential operators by finite differences. The Finite Element Method (FEM) discretizes the environment into a number of finite elements. FEM predicts higher levels of backscatter than models like NM, CM, PE and ray-based approximation [113]. This is due to the fact that the wave equation is solved without any approximation except for the discretisation of space and boundaries. However, it is impractical for modelling sound propagation over long distances because of the computational cost.

## 2.4 Prediction of control parameters

One of the principal outputs of the underwater sound propagation modelling is the acoustic pressure field as a function of range and depth  $p(r, z)$ . Knowing  $p(r, z)$ , different parameters of interest can be calculated. In this project  $SEL$  and  $L_{peak}$  were the parameters calculated because they are the main parameters employed to characterize impulsive acoustic noise produced in activities such as seismic surveys, as was explained in section 1.1.3.

This section defines these parameters and shows examples from the scientific literature where existing models led to agreements between the numerical predictions and measurements of the  $SEL$  as a function of range but could not predict accurately  $L_{peak}$ . The group of the selected studies comprises different locations and different propagation models. Moreover, they use different anthropogenic impulsive signals, including airgun array signals, signals from offshore impact pile driving, signals from underwater explosions, and sonar signals.

### 2.4.1 Prediction of the sound exposure level

The sound exposure (the integral in Eq. 1.2) is proportional to the signal energy and hence it characterises variations of sound energy. This means that, as long as the environmental model is appropriate, its prediction with existing deterministic models can be fairly accurate because the energy can be predicted accurately in those circumstances.

The agreement between measurements and predicted values of  $SEL$  has been observed in various studies. Some of them are cited in the next section to show the differences against the prediction of  $L_{peak}$  for the same signals. In addition to those, other examples can be found in results of the simulations with a model based on PE in deep and intermediate depth waters in the Canadian Beaufort Sea [52], and in the results of simulations of airgun signals with a model based on the ray theory in Norwegian waters [114]. In those cases, the prediction of  $SEL$  was achieved with good accuracy.

### 2.4.2 Prediction of the peak pressure level

As was explained in section 1.1.3, predicting  $L_{peak}$  of anthropogenic signals in real environments is necessary in order to comply with current marine noise regulations, but it is not an easy task, as it has been previously noticed by some authors [79, 115-118]. The difficulties mainly arise as a result of the interference between signals propagating along different paths in the ocean sound channel. This effect is noticeably larger for peak pressure than for energy. Moreover, the peak pressure is more affected by variations in environmental characteristics that cannot be modelled with absolute accuracy, such as the roughness of reflecting boundaries, varying sound speed gradients and moving scatterers in the water column (e.g. internal waves). Additionally, most of the existing models do not consider the incoherent component of the sound field and its destructive or constructive interference effects, so the numerically predicted values of  $L_{peak}$  can differ much from measurement data.

## Airgun array signals

An adiabatic mode model was found to perform poorly in peak pressure predictions in deep waters of Western Australia [115]. The prediction of the waveforms of airgun signals generally followed the same pattern as the measurements at shorter distances, but the predicted value of the peaks were noticeably higher at larger distances. The signal energy was much more accurately predicted. The most likely cause of the disagreement for the peaks is that the scattering on the seafloor roughness was not included in the model.

A ray-based model (PlaneRay [119]), despite not being the most appropriate model due to its initial HF approximation, gave a reasonable result for the *TL* of the sound pressure level at frequencies over 50 Hz in comparison with a wavenumber integration model and a PE model [120]. The PlaneRay model also resulted in reasonably good modelling results for the *SEL* of airgun signals in the field of Nordland VII in Vesterålen, Norway [114]. However, for the same signals the modelled levels of the peak pressure were higher than those in the measurements, particularly at long ranges from the source.

## Impact pile driving signals

In a study conducted in Puget Sound in the US state of Washington, using a model based on FEM for the sound generation from pile driving and PE for the sound propagation, the prediction of the peak amplitude was different from the measurements at depths smaller than the approximate depth of the first Mach cone's boundary [92]. This depth is defined in the article as  $z_{Mach} = r \tan \varphi_w$  where  $r$  is the range from the pile and  $\varphi_w = \sin^{-1}(c_w / c_p)$  is the cone angle of the first Mach cone for a sound speed in the water  $c_w$  and a longitudinal wave speed in the pile  $c_p$ .

Measurements of pile driving noise in the Moray Firth (NE Scotland) were made during the installation of wind turbines with the goal of analysing the sound produced and propagated from driven piles, and the potential impacts on marine fauna [121]. The prediction for the peak-to-peak sound pressure level exceeded the measurements at ranges less than 300 m, and underestimated them

at longer distances. The received levels were predicted by subtracting the transmission loss from the source level, and the transmission loss was calculated based on the modelling approach described in [58]. An overestimation of the actual source level was thought to be the reason for the disagreement.

The prediction of  $L_{peak}$  using a model based on wavenumber integration and validated with measurements of offshore pile driving noise in the Baltic Sea exhibited more uncertainty than the prediction of  $SEL$  [122].

### **Active sonar signals**

In a study with active sonar, a statistical approach was used to predict the potential impacts of the peak pressure on marine animals [37]. Two types of signals were used, a single frequency burst and a burst with a swept frequency. Probability density functions were calculated for both types of signal leading to skewed distributions. For the swept frequency signal the mean predicted for the transmission loss differed by 8 dB from the transmission loss calculated with an incoherent sum of arrival amplitudes.

### **Signals from explosions**

Predictions made with a weak shock theory for SUS charges in shallow water also resulted in an overestimation of the peak pressure in comparison with measurements [123]. The energy-related measure used in the same study was the “equivalent energy level” ( $EL$ ), representing the level of the energy flux density resulting from the integration over one second of the RMS pressure [124], also used in [117]. The  $EL$  was calculated and the values obtained were very close to the measurements. The reasons proposed to explain that difference were the loss of coherence after reflection from the boundaries, scattering from bubbles and absorption losses. On the other hand, in a more recent study [125], model predictions of  $L_{peak}$  showed agreement with new experimental data. In this study  $L_{peak}$  was estimated using an equation formulated in earlier research as a function of scaled range with the charge weight. They also presented a new equation for predicting  $SEL$  using an energy flux scaling parameter, and showed

good agreement with the measurements. However, these equations in terms of charge weight cannot be used with other signals.

### 2.4.3 Discussion

Several results have been presented in section 2.4 with significant differences between them. They show differences in the type of signals used, the locations where the studies were conducted, the propagation models used for predictions, and even the causes of disagreements in the obtained results. However, the studies had one characteristic in common: the peak pressure was not correctly predicted.

In this project an alternative method for predicting the peak pressure is presented, based on an empirical equation, as explained in Chapter 5. This model predicts the mean value of  $L_{peak}$  at different ranges. The model is complemented with a statistical method of variations in  $L_{peak}$  using extreme value theory, described in Chapter 7.

This page intentionally left blank

## Chapter 3.

# Experimental airgun array data: Description and processing

**M** easurements from three different seismic surveys using airgun arrays were used in this project. All surveys were conducted in Australian waters but the environments exhibited significant differences in depth and oceanographic parameters, which affected sound propagation. The different data sets are referred through the document by their location, listed below and displayed in Fig. 3.1.

- *Cape Leeuwin*: This survey took place in deep waters over the continental shelf and slope off Cape Leeuwin and Cape Naturaliste in South Western Australia.
- *Dongara*: This survey was carried out in shallow waters close to Dongara, in Western Australia.
- *Bass Strait*: This survey was conducted in medium depth waters in the western part of Bass Strait, between Tasmania and Victoria.

It must be noted that the information about the pile driving data used in this project is not included in this chapter but in Chapter 8, which is exclusively dedicated to offshore piling noise.



Fig. 3.1: Map of Australia showing the three locations where the airgun array seismic surveys were conducted.

## 3.1 Cape Leeuwin

### 3.1.1 Description of the survey

The first data set analysed was obtained from a marine seismic survey carried out for Geoscience Australia during October and November, 2004.

These data were previously used to estimate seafloor properties through geoaoustic inversion of the transmission loss and also to study the airgun signal arrival structure [115].

The source, a linear array of 40 airguns and total volume of 4900 cui, was towed at 8 m below the sea surface along several transects over the continental shelf and slope off Cape Leeuwin and Cape Naturaliste (Fig. 3.2).

Recordings were made in a frequency band of 1-100 Hz at the hydroacoustic station HA01, deployed as part of the International Monitoring System of the Comprehensive Nuclear-Test-Ban Treaty (CTBT). The HA01 station consists of three receivers moored in a nearly equilateral triangular configuration with about 2 km sides (see Fig. 3.3) at 1100 m depth below the sea surface, close to the axis of the *Sound Fixing And Ranging* (SOFAR) channel. The axis of this channel lay at



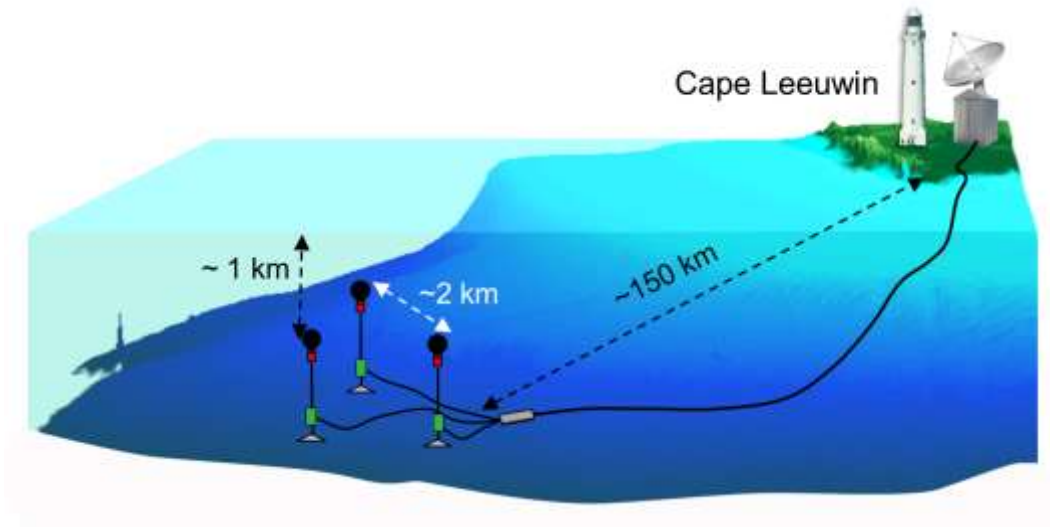


Fig 3.3: Hydrophone array of station HA01 off Cape Leeuwin. Figure based on Alexander Gavrilov's illustration.

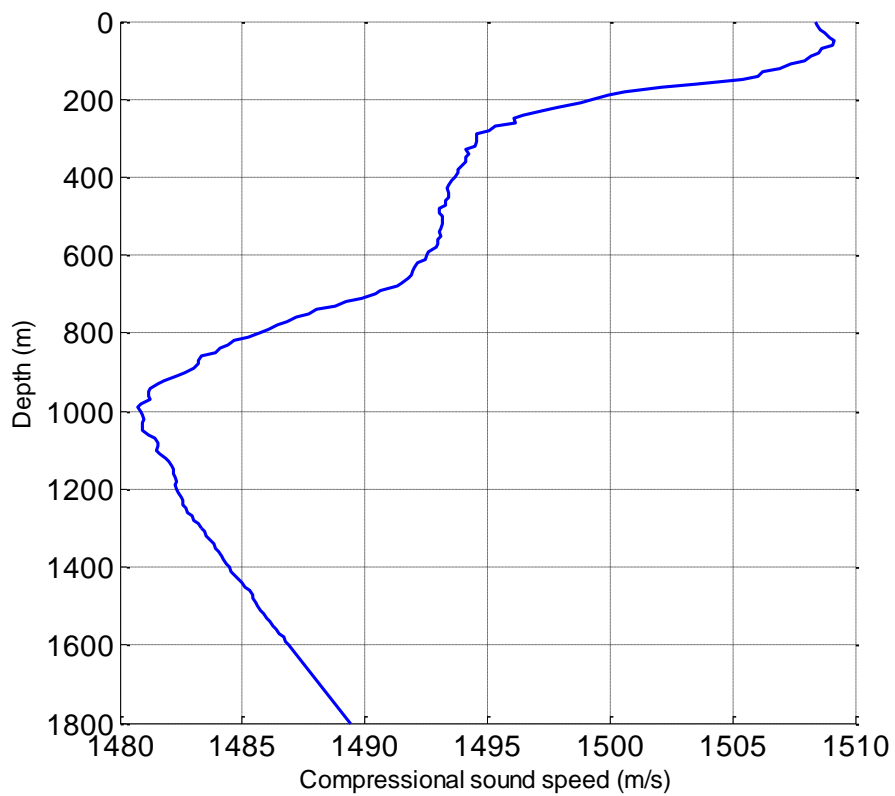


Fig. 3.4: Sound speed profile over the continental slope off Cape Leeuwin measured in November 2005.

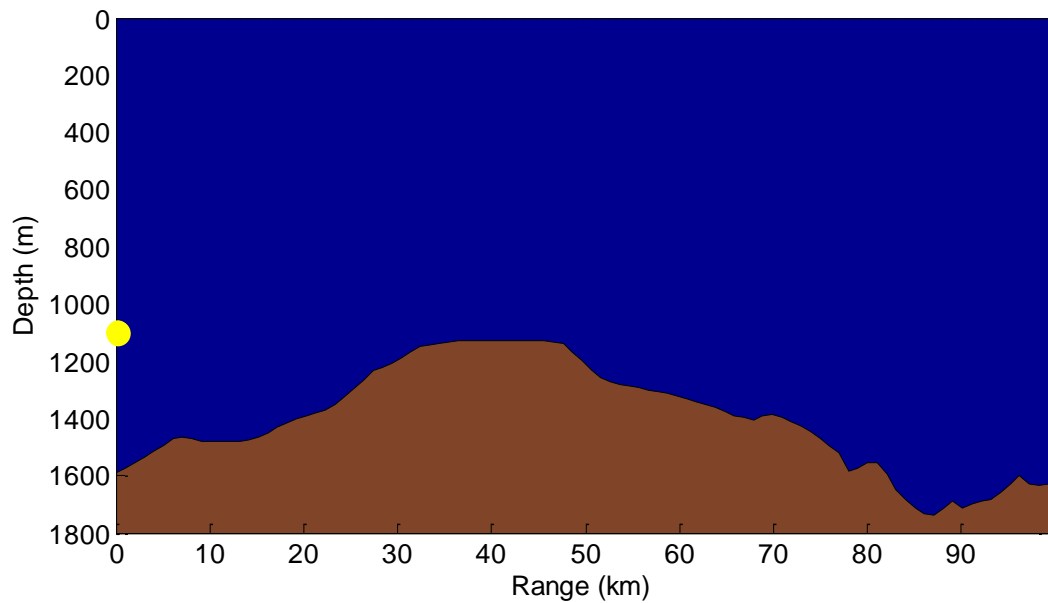


Fig. 3.5: Bathymetry along the acoustic propagation path (highlighted in Fig. 3.2 with a thick red line). The position of the receiver is depicted by a yellow dot at 1100 m from the surface.

### 3.1.2 Signal processing

The recorded signals were low-pass filtered at 100 Hz by an anti-aliasing filter and sampled at a frequency of 250 Hz in the H01 hydroacoustic station.

The signal energy was corrected for background noise by subtracting the noise power measured right before the first signal arrival and multiplied by the time used to calculate the sound exposure of the airgun signal (see the waveform from a single shot in Fig. 3.6).

The spectrum of airgun signals recorded at various ranges from 17 to 90 km was analysed to check the effect of limited bandwidth on  $SEL$  and  $L_{peak}$  values. Reducing the cut-off frequency of low-pass filtering to 90 Hz did not noticeably affect the values of  $SEL$  and reduces the  $L_{peak}$  by less than 1 dB, which means that the limited bandwidth of recording did not significantly affect results of the further analysis.

The sound exposure and peak pressure levels were calculated for each range. Transmission losses associated with each of those measures were also calculated by using the source signal modelled with the airgun array model developed at

CMST (see section 2.2.1.3). The results are presented in Chapter 4 for comparison with simulations, and also in Chapter 5 together with the analysis of signals recorded in the other two locations.

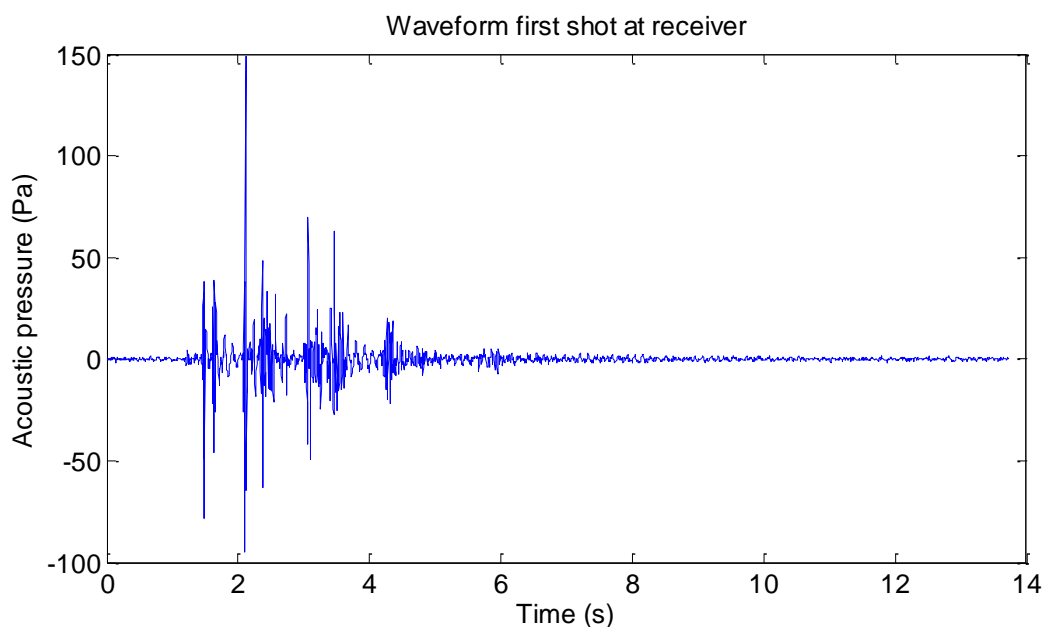


Fig. 3.6: Waveform of the first shot recorded at 16.9 km from the source.

## 3.2 Dongara

### 3.2.1 Description of the survey

This data set was collected during October and November 2003 in an airgun seismic survey in shallow waters of the continental shelf off the Dongara coast, in Western Australia (see map in Fig. 3.7). This was one of the four surveys conducted by RocOil Pty. Ltd during that time period, referred as *Lilian survey* in the field report prepared by CMST [126]. CMST deployed several autonomous acoustic recorders to analyse the possible impact of the noise produced by the airguns on whales, given the simultaneity of the survey and the migration season of humpback whales. The autonomous sound recorders used for these measurements were designed and built by CMST [127]. The recorders were deployed on the seafloor with the hydrophones laid on the bottom. The gain of an impedance matching pre-amplifier in each noise logger was set to be 20 dB.

The underwater noise signal was digitized at a sampling rate of 5 kHz using a 16-bit analogue-to-digital converter. An anti-aliasing filter with a cut-off frequency at 2.2 kHz was applied to the analogue signal before conversion. The total gain of the recording channel was set to be 40 dB. The recorders were programmed to make continuous 200 s long recordings with 300 s intervals between the recording start times.

All recorders were calibrated before deployment by using white noise of known level as an input signal of the recording system with the hydrophone connected in-series to the noise generator. The recorded sea noise signals and their spectra were corrected for the end-to-end frequency response of the recording system, so that the sound pressure and power spectrum density were measured in absolute units ( $\mu\text{Pa}$  and  $\mu\text{Pa}^2/\text{Hz}$  respectively).

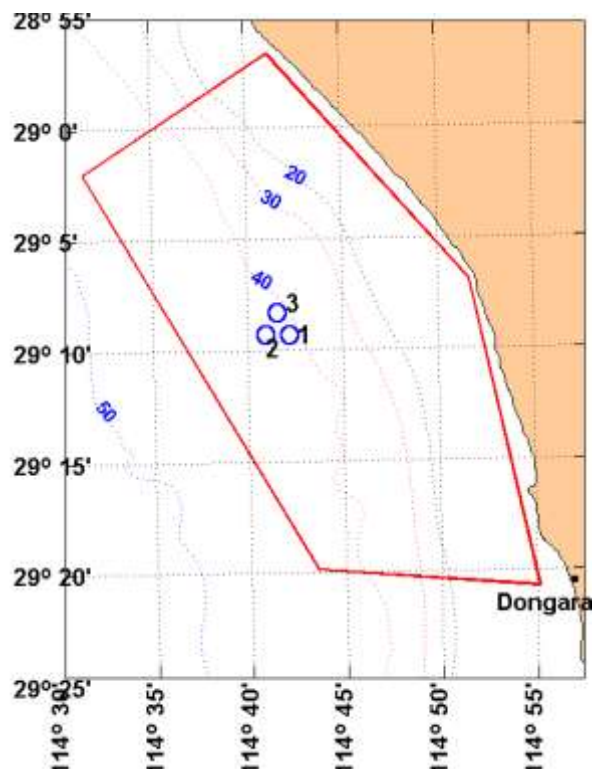


Fig. 3.7: General map of the survey with the location of recorders 1, 2 and 3 [126].

There were three bottom-mounted recorders in a triangular setup. Only data acquired by recorder 1 (Fig. 3.7) were used in this project. This recorder was situated in a water depth of 39 m.

The source, a planar array of 20 airguns (9 active) with overall dimensions 14 by 10 m and total active volume of 1790 cui, was towed 4 m below the sea surface along many tracks (see location of survey shots depicted in blue in Fig. 3.8) and 38563 shots were recorded at a sampling frequency of 5 kHz.

### 3.2.2 Signal processing

For the analysis of the recorded data, six different tracks were selected along three directions (NW, SE and SW-NE) comprising measurements at ranges from approximately 1 to 15 km. In Fig. 3.8 the selected tracks are plotted in red over the map with the locations of all shots fired (in blue). The magenta dot shows the location of the receiver. For the tracks selected, the signals recorded at shorter distances were discarded if their maximum amplitude exceeded the dynamic range of linear amplitude response of the sound recorder. The description of the tracks after data processing, including the number of shots and range span, is presented in Table 3.1.

Table 3.1: Description of tracks after data selection

<b>Track</b>	<b>Number of Shots</b>	<b>Range (km)</b>
<b>1NW</b>	634	1.3-15.1
<b>1SE</b>	551	1.3-14.6
<b>2NW</b>	1137	2.7-15.2
<b>2SE</b>	509	2.7-11.1
<b>3SW</b>	199	1.6-5.5
<b>3NE</b>	388	1.7-9.1

The influence of background noise, including instances of high amplitude impulsive noise from nearby snapping shrimp, on  $SEL$  and  $L_{peak}$  measurements was reduced by low-pass filtering with a cut-off frequency of 230 Hz. The potential impact of the cut-off frequency of 230 Hz on  $SEL$  and  $L_{peak}$  was analysed by comparing measurement results with those obtained with a cut-off frequency of 500 Hz excluding the signal recordings with the presence of snapping shrimp impulses of high amplitude. The difference was of a 0.1 dB order, so this filtering did not have any significant impact on the further correlation analysed.

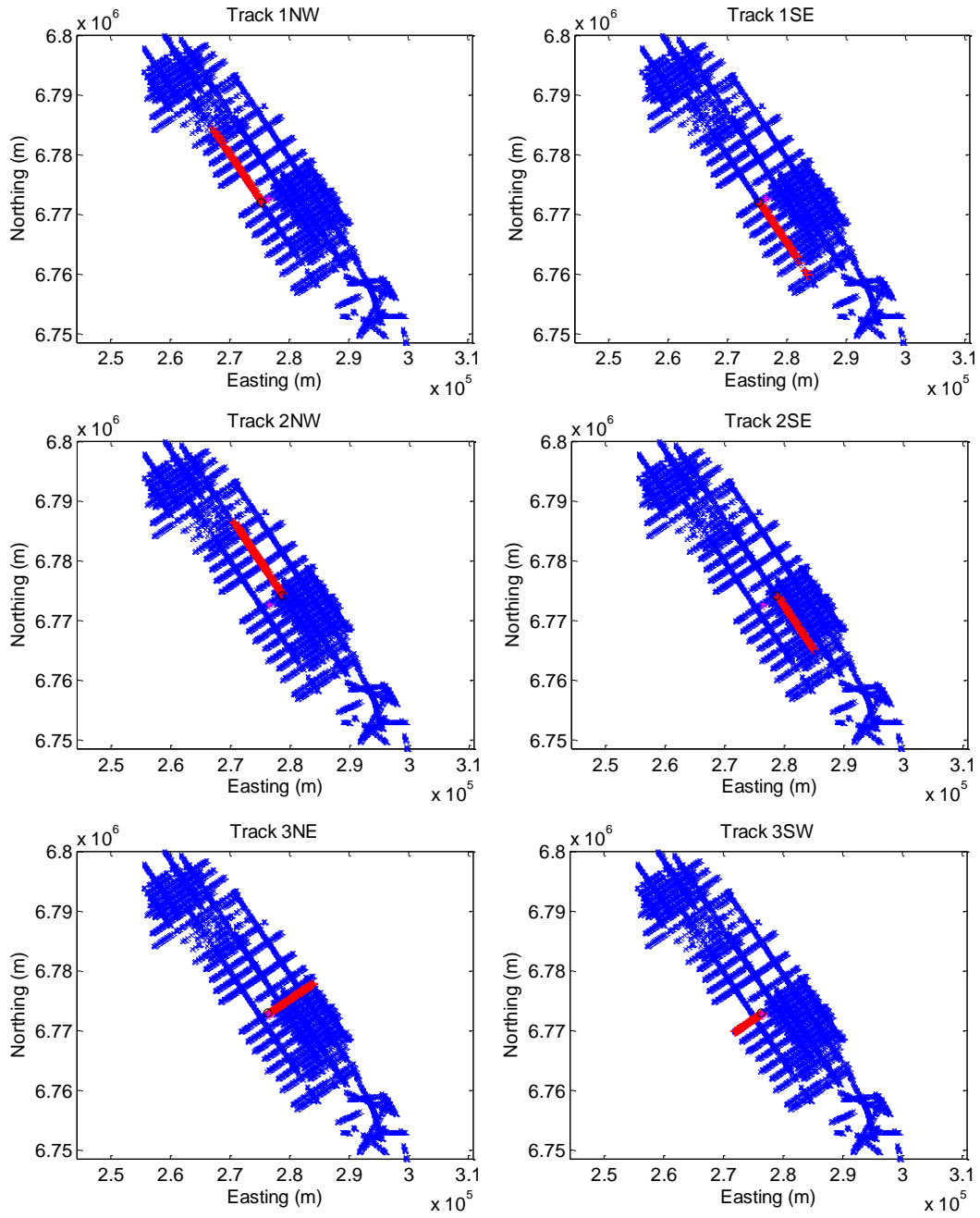


Fig. 3.8: Location of survey shots (blue) and tracks analysed (red). The magenta dots are the receiver location. The coordinates are given in metres for UTM zone 50

## 3.3 Bass Strait

### 3.3.1 Description of the survey

This third data set comprises measurements of airgun signals from the Aragorn gas field seismic survey, which took place at the western side of Bass Strait in 2006. The source was a planar array of 28 active airguns of overall dimensions 15 by 24 m with a total active volume of 3090 cui. The measurements of the signals from this survey were part of a project supported by Origin Energy. An underwater sound recorder developed and built at CMST was used to collect this dataset. The recorder was deployed on the seafloor. The gain of an impedance matching pre-amplifier in each noise logger was set to be 20 dB. The underwater noise signal was digitized at a sampling rate of 6 kHz using a 16-bit analogue-to-digital converter. An anti-aliasing filter with a cut-off frequency at 2.8 kHz was applied to the analogue signal before conversion. The total gain of the recording channel was set to be 20 dB. The recorders were programmed to make continuous 200 s long recordings with 900 s intervals between the recording start times.

The recorder was calibrated before deployment by using white noise of known level as an input signal of the recording system with the hydrophone connected in-series to the noise generator. The recorded sea noise signals and their spectra were corrected for the end-to-end frequency response of the recording system, so that the sound pressure and power spectrum density were measured in absolute units ( $\mu\text{Pa}$  and  $\mu\text{Pa}^2/\text{Hz}$  respectively).

Data from three seismic tracks were used in this study, recorded in a frequency band of 5 Hz to 3 kHz at distances from around 2 to 15 km from the source. The geographic location of Track 1 is displayed in Fig. 3.9. Tracks 2 and 3 were very close and parallel to Track 1.

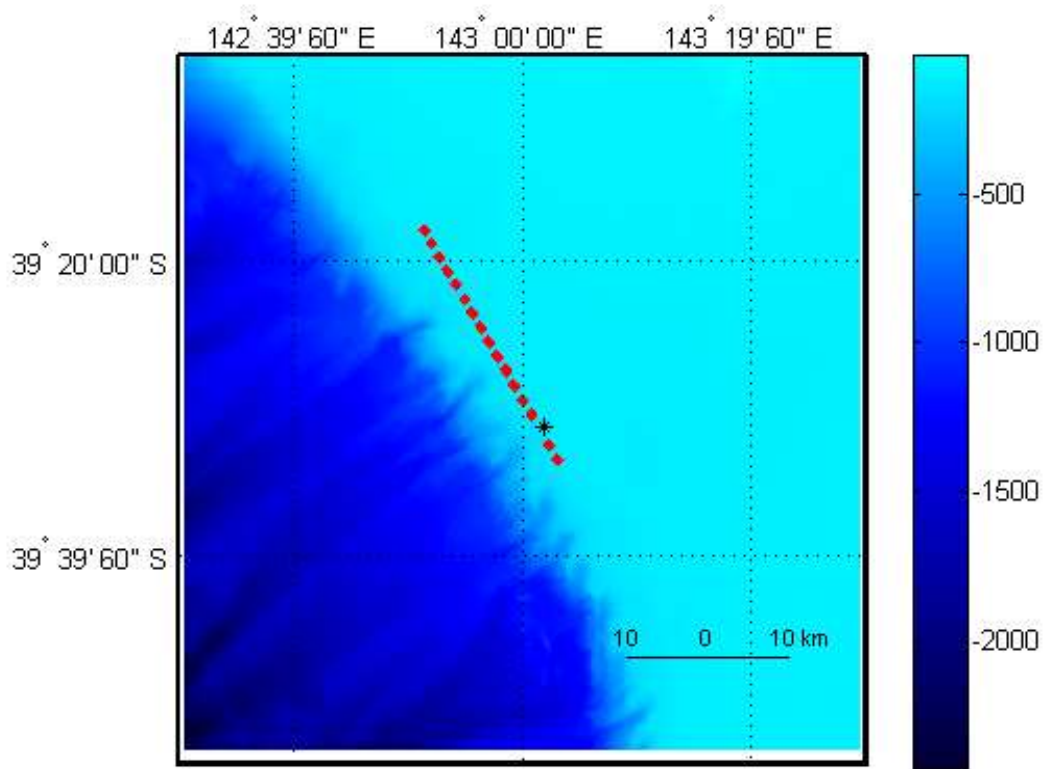


Fig. 3.9: Track 1 of Bass Strait survey.

### 3.3.2 Signal processing

Figure 3.10 shows an example of the waveform received at different distances from Track 1. Signals measured at distances greater than 13 km in all three tracks were discarded as their SNR was too low.

The number of shots taken from each track is presented in Table 3.2 together with the ranges of measurements. The bathymetry along each track is shown in Fig. 3.11 together with the sea depths at the locations of the selected shots after processing of signals. Both of them were obtained from the Geoscience Australia Bathymetry/Topography Grid data (2005) using the locations of the receiver and the furthest shot location.

Table 3.2: Description of tracks after processing

Track	Number of shots	Range (km)
1	175	1.96-12.74
2	150	1.52-12.90
3	150	2.82-11.51

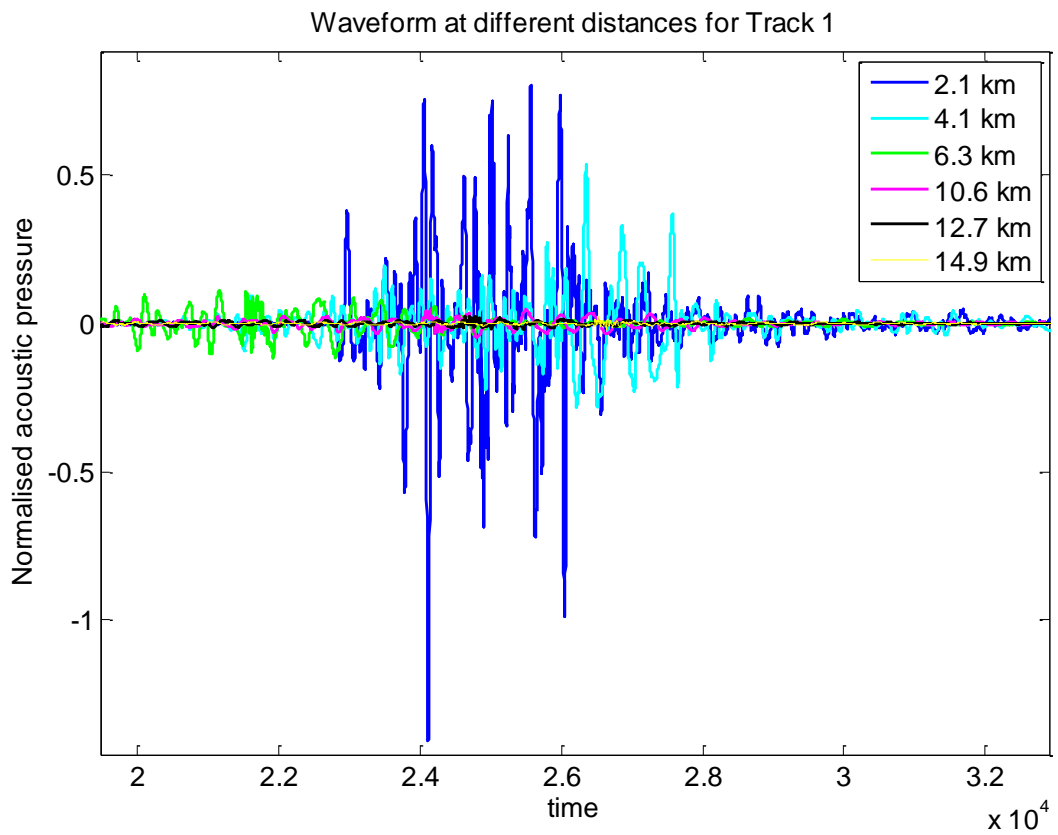


Fig. 3.10: Waveform measured at different distances from the source.

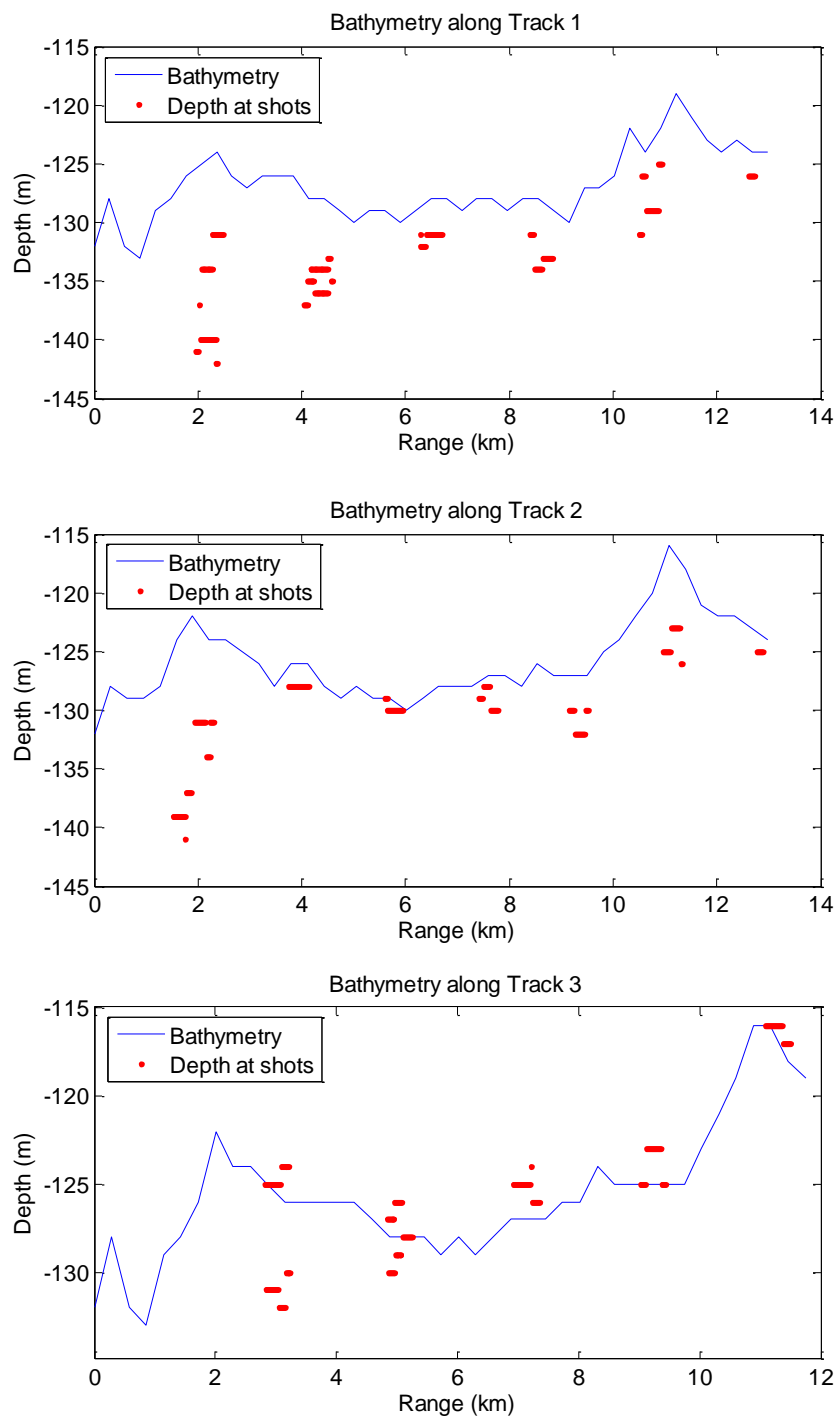


Fig. 3.11: Bathymetry (blue line) along transects from the sound receiver to the furthest shot location of seismic tracks 1 (top), 2 (middle) and 3 bottom. Red dots show sea depth at the location of each shot of the three seismic tracks versus distance to the receiver. Note that the sound propagation paths from different shorts were not fully coincident with the seismic tracks. Therefore the sea depth at shot locations differs from that measured at the same distance from the sound receiver in the direction to the furthest shot.

## Chapter 4.

# Modelling of sound propagation: Numerical simulation using the data of Cape Leeuwin

**S**imulation results of sound propagation from an airgun array, including the modelling of the source, are presented in this chapter. The environment chosen to be modelled was the Cape Leeuwin site because not only was this data set recorded with a fine range grid but it is also the one that comprises measurements to the longest ranges. These characteristics are important given that the results of the simulation are compared with the experimental data to determine afterwards the goodness of the model and the prediction capabilities for different metrics.

### 4.1 Description of the simulations

#### 4.1.1 Sound propagation modelling

The main models available to numerically simulate the propagation of underwater sound were described in 2.3.1. Considering the domains of applicability of such models, explained in [56], the most suitable propagation models for LF sound signals in deep waters (characteristics of this survey) would be models based on the NM and PE solutions. In a range dependent environment, like that over the continental slope of Cape Leeuwin, a model based on the PE approximation is the most appropriate. In contrast, the NM

model, although applicable, has some limitations for this type of environment: with respect to the accuracy, if the adiabatic approximation is used, or on the computationally efficiency in the case of coupled NM.

Two propagation models were used to model the sound propagation. The first model is RAMGeo, a range-dependent PE algorithm for fluid seabeds, capable of modelling effects in the sound field resulting from mode coupling [55]. The second model is an adiabatic mode model, which does not include mode coupling. Even though the former was expected to produce the most accurate results, the second model was used for comparison with the first model and the experimental data.

Transfer functions (sound field as a function of frequency and range) were calculated using each model on a frequency grid spanning the band from 5 to 100 Hz with an increment of 0.05 Hz. The increment was first estimated based on the maximum possible signal spread due to multipath propagation, which governs the signal duration and can be determined from the measurements or numerically predicted via modelling. Then it was refined after testing different values and finding 0.05 Hz to be the best compromise between accuracy and computational cost. The sound speed profile and bathymetry described in section 3.1.1 were included in both models. Range grids were different in each model except for the maximum value, which was determined by the bathymetry data; for the adiabatic mode model the minimum range was approximately 50 m, and the same value was used as the range increment. For RAMGeo, it was possible to use a finer grid without too high a computational cost. The minimum value chosen was 100 m, and the increment was 10 m. The depth grid used for RAMGeo was 100 points with an increment  $dz = \lambda / \Lambda_z$  where the wavelength  $\lambda$  is calculated for the minimum value of the sound speed and  $\Lambda_z$  is a constant value of 30, a value determined to increase the computational efficiency while maintaining convergence of data. The maximum depth (Eq. 4.1) was determined as the maximum value of the bathymetry data plus a bottom section proportional to the wavelength in the bottom  $\lambda_{bottom}$ . The wavelength was calculated for the maximum value of the sound speed and the constant  $\Lambda_z$  was assigned to be 100, since the output on the sound field for the tested frequency of 100 Hz was not

significantly different for larger values. For RAMGeo, which uses the split-step Padé solution, the number of Padé terms was selected to be 6.

$$Z_{\max} = \max(Z_{\text{bathy}}) + \Lambda_Z \lambda_{\text{bottom}}. \quad (4.1)$$

After obtaining the transfer functions, waveforms were calculated with a method based on Fourier synthesis of solutions of the wave equation in the frequency domain, a technique often employed in broadband modelling. This process is necessary to calculate the sound waveform and the peak pressure of it.

### 4.1.2 Source

The source signal was modelled using a variation of the airgun bubble model [85] originally developed for a single gun and later expanded into a model of sound emission from an airgun array developed at CMST [87], explained in section 2.2.1.3.

The modelled array was a linear array of 40 airguns of different sizes with 4900 cui total volume, towed at 8 m below the sea surface. The vertical directivity of the array was modelled for elevation angles varying from 0 degrees (horizontal plane) to 90 degrees (vertically downward) with an increment of 5 degrees. As the array was towed almost along the sound transmission path, the azimuth angle was about 180 degrees, which is almost equivalent to 0 degrees, given the axial symmetry of the array's directivity pattern. The source signal used for modelling of sound propagation is shown in Fig. 4.1, obtained for 0 degrees elevation and 0 degrees azimuth.

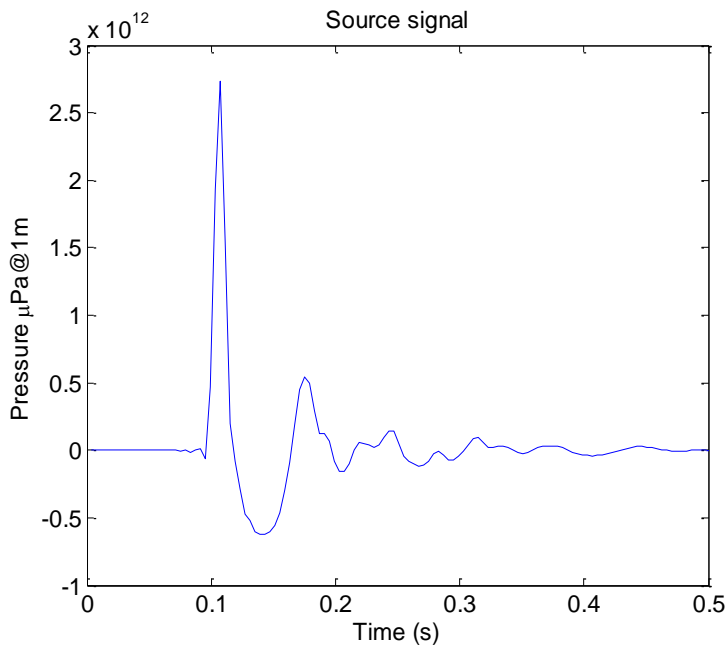


Fig. 4.1: Modelled source signal for 0 degrees elevation and 0 degrees azimuth.

### 4.1.3 Geoacoustic model

The seafloor was modelled as a fluid half-space with parameters previously estimated by geoacoustic inversion [115]. These parameters correspond to medium-to-coarse sand with the compressional wave speed  $c_p = 1850$  m/s and sediment density  $\rho = 2000$  kg/m<sup>3</sup>. The compressional wave attenuation in the sediment  $\alpha_p$  was assumed to have a linear dependence on frequency, and the value estimated from geoacoustic inversion was 0.28 dB/ $\lambda$ . In this project different values of this coefficient were tested and it was found that a value of 0.5 dB/ $\lambda$  gave the best agreement in comparison with the experimental data for the transmission loss associated with the sound exposure level (defined in the following subsection). The transmission loss of the energy for different compressional wave attenuations using RAMGeo and the adiabatic mode model is shown in Fig C.1.1 (Appendix C).

#### 4.1.4 Calculated metrics

The transmission loss as a function of range was calculated for the sound exposure and for peak pressure after simulation of the waveform.

The transmission loss associated with the sound exposure level ( $TL_E$ ) is defined as the difference between the source sound exposure level  $SL_E$  (the sound exposure level referred to a distance of 1 m from an equivalent point source) and the sound exposure level at the receiver,  $SEL$ :

$$TL_E = SL_E - SEL \text{ dB}, \quad (4.2)$$

where

$$SL_E = 10 \log_{10} \left( \int_0^T p_{source}^2 dt \right) \text{ dB re } 1 \mu Pa^2, \quad (4.3)$$

and  $p_{source}$  being the source signal.

An equivalent expression is defined to account for the attenuation of the peak pressure with distance, and it will be referred to as the transmission loss associated with the peak pressure ( $TL_{peak}$ ). It is calculated by subtraction of the received peak pressure level ( $L_{peak}$ ) from the source peak pressure level ( $SL_{peak}$ ), which is the peak pressure level of the source signal referred to  $r = 1$  m:

$$TL_{peak} = SL_{peak} - L_{peak} \text{ dB}, \quad (4.4)$$

where

$$SL_{peak} = 20 \log_{10} \left( \max |p_{source}(t)| \right) \text{ dB re } 1 \mu Pa. \quad (4.5)$$

### 4.1.5 Numerical prediction results and comparison with measurements

The resulting values from simulation of the transmission loss vs. range are compared with the experimental data in Fig 4.2.

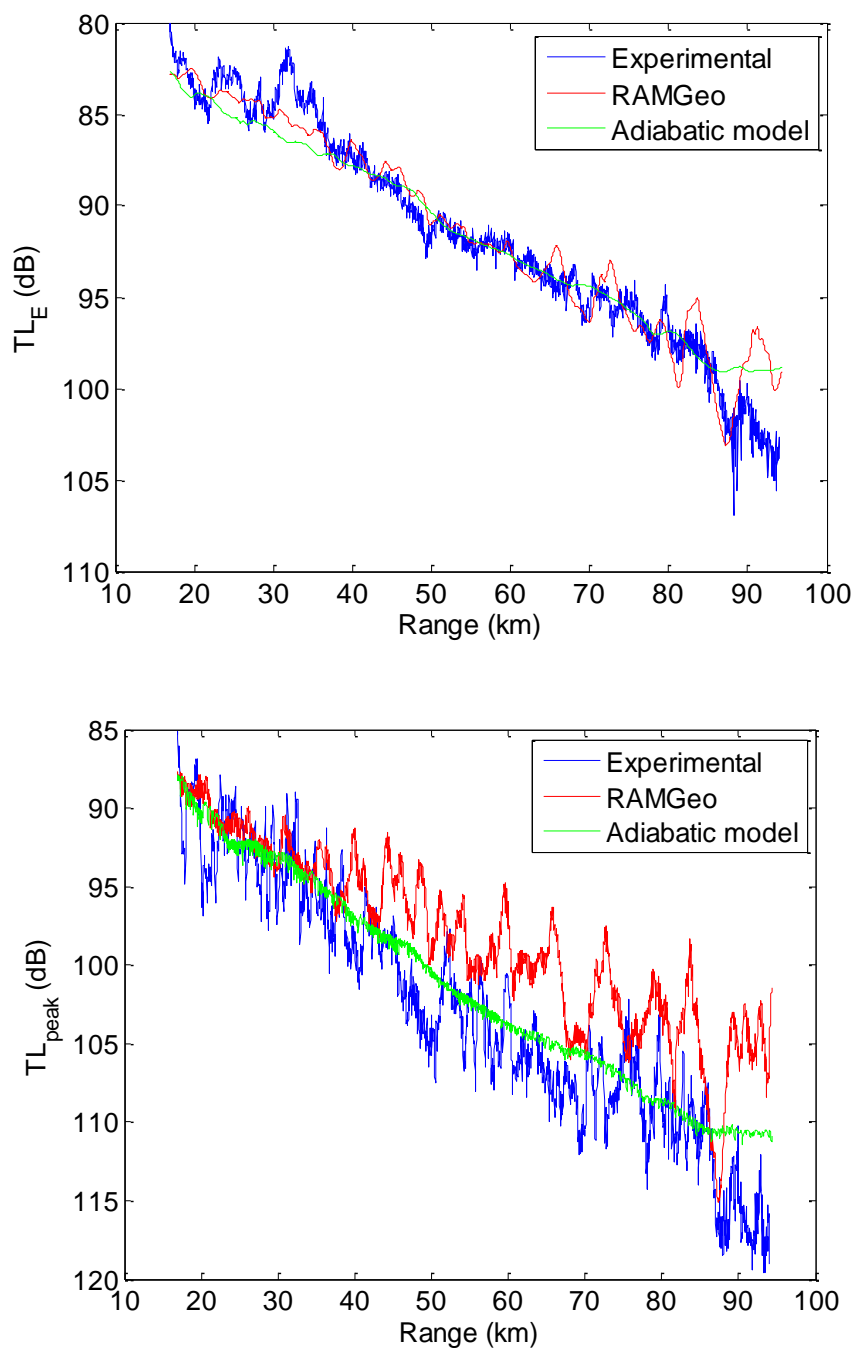


Fig. 4.2: Comparison of the transmission loss obtained from the experimental data and simulations with RAMGeo and adiabatic mode model. The  $TL$  is shown for the sound exposure level (top) and peak pressure level (bottom).

Both propagation models predict a similar decay rate for  $TL_E$ , which is close to the measured decay as well. However, it must be noted that the curve predicted with RAMGeo looks more similar to the measurement data because it shows more fluctuations around the average decay rate than the adiabatic mode model. The difference observed between the measurements and predictions is most likely due to an oversimplified model of the seafloor.

For  $TL_{peak}$ , however, both models predict slower decay rates than that in the experimental data. Although the average slope of the decay predicted by the adiabatic mode model is closer to the measurements than the RAMGeo prediction, the latter predicts spatial fluctuations more similar in the amplitude to those observed in the experimental data, which the adiabatic mode model does not predict.

The transmission loss was also calculated in octave bands to analyse the dependence on frequency (Fig. 4.3). RAMGeo makes the most accurate prediction for  $TL_E$  in the frequency band of 20-40 Hz at ranges below 90 km. In the same range interval the prediction in the frequency band of 10-20 Hz for  $TL_E$  is also fairly good. More deviation from the measured data can be observed in the higher frequency band of 40-80 Hz for the same metrics.

For  $TL_{peak}$ , RAMGeo predicts the closest decay to the measurements in the frequency band of 10-20 Hz between approximately 50 and 80 km. In the other frequency bands the prediction differs more from the experimental data. With regard to the prediction with the adiabatic mode model, no significant differences can be observed in the different frequency bands for both  $TL_E$  and  $TL_{peak}$ .

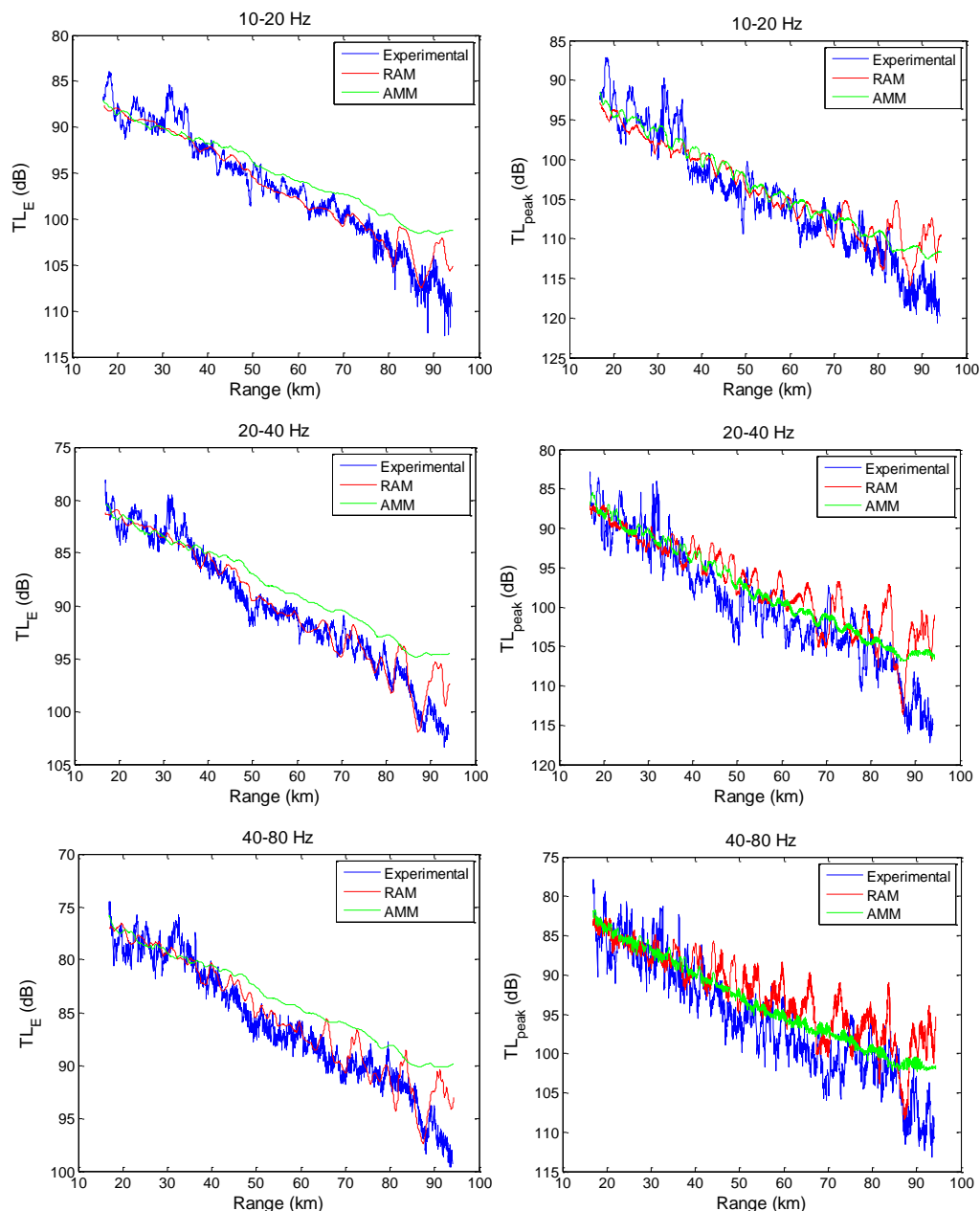


Fig. 4.3: Comparison of the transmission loss obtained from experimental data and simulations with RAMGeo and adiabatic mode model (AMM) in octave bands 10-20 Hz (top), 20-40 Hz (middle), 40-80Hz (bottom).  $TL$  for sound exposure (left);  $TL$  for peak pressure (right).

## 4.2 Concluding remarks

The sound exposure level, which is proportional to the logarithm of signal energy, can be predicted with satisfactory accuracy using the existing underwater acoustic models when the environmental parameters are known to a certain extent, as seen in the results presented in this chapter. However, these models are not capable of predicting the peak pressure level in a sufficiently accurate way.

Simulations showed that RAMGeo and the adiabatic mode model predict a similar decay rate for the sound exposure level, which is close to the measured decay. RAMGeo offers a more realistic prediction result because it allows for coupling of signals propagated with different modes in contrast to the adiabatic mode model. The difference between the measured and modelled  $TL$  slopes is thought to be a consequence of some inaccuracies in the bathymetry and geoacoustic model of the seabed.

Both models predict slower decay rates of the peak pressure in the numerically simulated signal waveforms than the experimental data. In spite of that, RAMGeo is considered to give a better result than the adiabatic mode model because it predicts a spatial pattern closer to the measured data.

This page intentionally left blank

## Chapter 5.

# Empirical analysis of airgun array signals and semi-empirical prediction of peak pressure

“It is beautiful here, my friend; every day I discover even more beautiful things (...) I want to paint it all (...) I start to see and understand (...) I can see nature and I can catch it all... it is by observation and reflection that I discover how”.

- Claude Monet

**W**ith the purpose of having a better understanding of the correlation between the peak pressure level and the sound exposure level, measurements from the three seismic surveys described in Chapter 3 were analysed. The study started from analysing each data set individually. The results from these analyses led to a generalised analysis of all measurements together.

An initial statistical analysis is also presented in this chapter for the individual data sets and for all sets combined in a single set. A full statistical study with a theoretical foundation is covered in Chapter 7 with the analysis of the fluctuations of  $L_{peak}$  around the mean value. In this chapter, the difference  $\Delta L_{peak} = L_{peak} - L_{peak}^{emp}$ , where  $L_{peak}$  is the experimental measurements of the peak

pressure level and  $L_{peak}^{emp}$  is the empirical prediction, is calculated for all ranges. The distribution of this difference was analysed. For each data set, a histogram of  $\Delta L_{peak}$  and a plot of the Cumulative Density Function (CDF) are presented, together with the best fit of a normal distribution. In addition, a one-sample Kolmogorov-Smirnov (K-S) test is conducted to examine the goodness of the fit, where the hypothesized distribution is a normal distribution.

## 5.1 Preliminary empirical results

Results published in the underwater acoustic literature (see section 2.4.2) and, moreover, the simulation results obtained during this project and presented in Chapter 4, suggest that the available underwater sound propagation models cannot accurately predict the peak pressure level of impulsive signals at long distances from the source.

Signals measured over the continental slope off Cape Leeuwin are used in this section to exemplify the different behaviour of the sound exposure and peak pressure with range. Signals received at similar distances from the source could be expected to have similar values of  $SEL$  and also similar values of  $L_{peak}$ . However, that is true for the signal energy and hence for the  $SEL$ , which fluctuates to a lesser extent than the instantaneous and peak pressure in a randomly varying ocean, as mentioned in section 2.1 and considered in detail based on a stochastic signal theory in Chapter 7, but not for  $L_{peak}$  because the peak pressure value is strongly affected by multipath effects in this type of environment [114]. This is demonstrated in Fig. 5.1 with signals recorded at approximately 17 and 83 km from the source. Two signals received at around 17 km (Fig 5.1 - left panel) have very similar values of  $SEL$  (only 1 dB difference) while the  $L_{peak}$  values are different by 6 dB. The same effect takes place at long distances where more arrivals interfere with each other. This can be seen in the waveforms recorded at around 83 km (Fig 5.1 - right panel). The  $SEL$  varies again by 1 dB, while the difference in the  $L_{peak}$  is 5 dB.

Correlation between  $L_{peak}$  and  $SEL$  could be expected as they both depend on sound pressure in the signal which decays with distance from the sound source in the ocean through propagation (spreading and absorption) losses. However, the exact relation between them is not evident. This is analysed in this chapter.

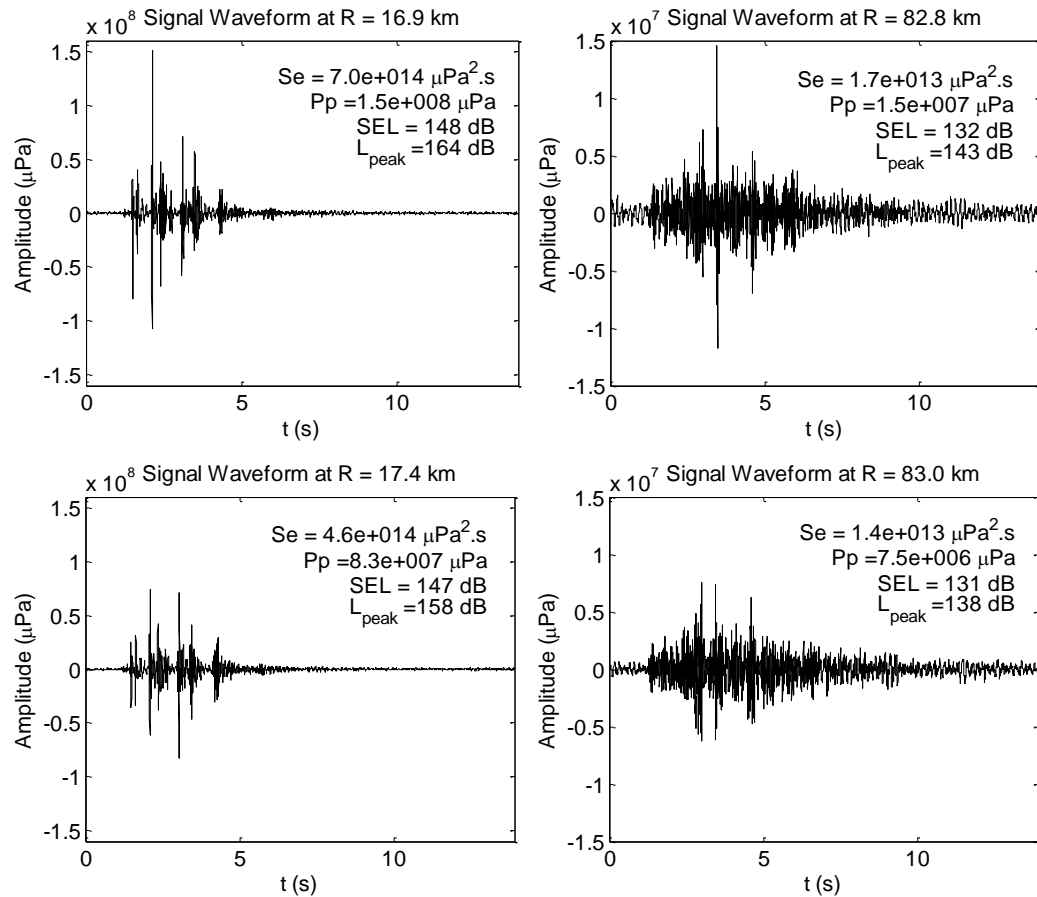


Fig. 5.1: Waveforms of airgun array signals received at different distances from the source: short distances 17.4 km, and 16.9 km (left panels), and long distances 82.8 km and 83.0 km (right panels).

## 5.2 Individual data sets

### 5.2.1 Cape Leeuwin

The experimental  $TL_E$  and  $TL_{peak}$  are plotted as a function of range in Fig. 5.2.  $TL_{peak}$  decreases with range noticeably faster than  $TL_E$ . The main cause of this difference is spreading and scattering of individual signal arrivals associated with different rays or groups of modes, which was observed in the measured waveform at longer ranges.

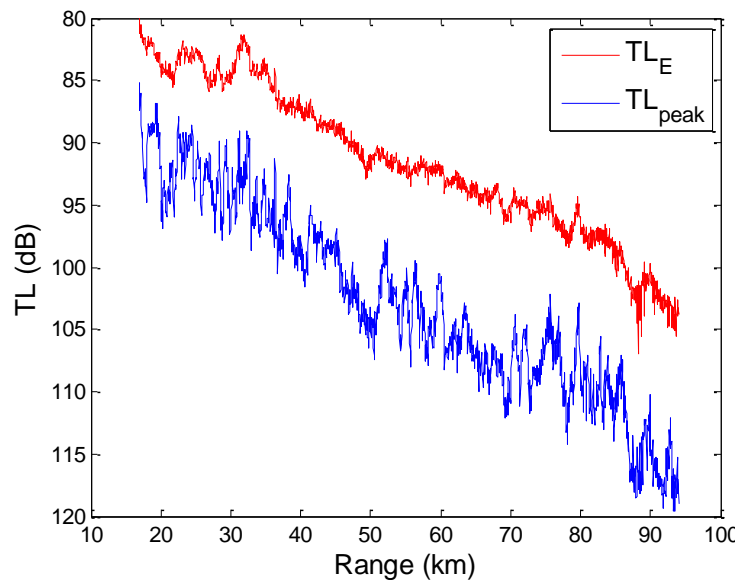


Fig. 5.2: Experimental transmission loss of the sound exposure and the peak pressure levels.

$L_{peak}$  measurements are plotted against  $SEL$  in Fig. 5.3. Strong correlation between these two characteristics is evident from the result shown in this figure. A linear regression of these data results in an empirical equation Eq. 5.1, where the regression coefficients have the values  $A = 1.24$  and  $B = -24.0$  dB re  $1 \mu\text{Pa}$ , obtained with a root-mean-square residual of 1.9 dB. Being rigorous, one must notice that the coefficient  $A$  is not exactly dimensionless, but it has units of dB re  $1 \mu\text{Pa}/\text{dB re } 1 \mu\text{Pa}^2\cdot\text{s}$ . However, these units are hereinafter omitted for simplicity. The value of  $A$  being greater than 1 is expected because  $L_{peak}$  decreases faster than  $SEL$ .

$$L_{peak}^{emp} = A \cdot SEL + B \text{ dB re } 1 \mu\text{Pa} . \quad (5.1)$$

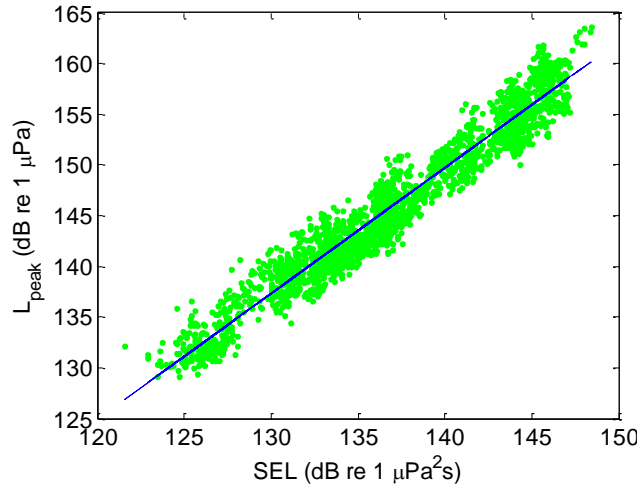


Fig. 5.3: Measured peak pressure level versus sound exposure level and the line from best linear fit.

Similar correlation was previously observed in two different works, but it was not used as a predictive tool in any case. In [75] fluctuations of signals at 400 Hz from the ASIAEX experiment were studied. The average intensity and peak pressure were measured, and the correlation between them was shown. However, it was not quantified through an equation. In the second study [46], measurements of pile driving noise at two different locations in Port Phillip Bay, Victoria, Australia, were analysed. The authors presented a linear equation relating the peak-to-peak level ( $L_{p-p}$ ) and the  $SEL$ , obtaining a slope ( $A$  in Eq. 5.1) of 1.12 and an offset ( $B$  in Eq. 5.1) of 12.3 dB, which are different from the values obtained for the regression coefficients in this study. The difference between  $L_{p-p}$  and  $L_{peak}$  is about 6 dB. Therefore, their regression coefficients in Eq. 5.1 would be  $A = 1.12$  and  $B = 6.3 \text{ dB re } 1 \mu\text{Pa}$ . The difference in the value of  $B$  was believed to be a consequence of the very different environments and sound sources.

The empirical equation (Eq. 5.1) with the coefficients  $A = 1.241$  and  $B = -24.0 \text{ dB re } 1 \mu\text{Pa}$  was applied to the  $SEL$  measurements to obtain  $L_{peak}^{emp}$ . The result is

shown in Fig. 5.4. The agreement between the empirical prediction and the measured data is fairly good, except for the amplitude of fluctuations which are governed by the *SEL* fluctuations in the empirical prediction.

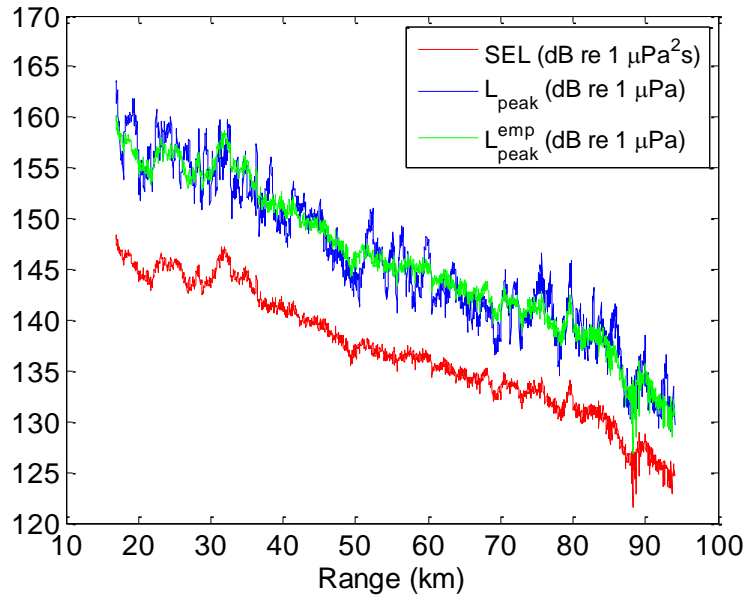


Fig. 5.4: Sound exposure level, peak pressure level and empirical prediction of peak pressure level from sound exposure level.

The difference  $\Delta L_{peak}$  was calculated for all ranges and its distribution was analysed. A one-sample Kolmogorov-Smirnov (K-S) test [128] was conducted to determine the goodness of the fit. This test uses as a null hypothesis that the tested samples could belong to a random value distributed with a hypothesized CDF. In this case, the hypothesized distribution is a normal distribution. The results of this test are two parameters: the hypothesis status  $h$  and the  $p$ -value of the hypothesis  $p$ . The former will have the value of either 1 or 0, where 1 means that the null hypothesis is rejected at the 5% significance level. The latter will have a value within the range of  $[0, 1]$ , where lower values represent more uncertainty about the null hypothesis. The result of the K-S test rejected the hypothesis of the normal distribution. However, when comparing the measured and best-fit CDF plots, the measurements could be approximated by the model normal distribution.

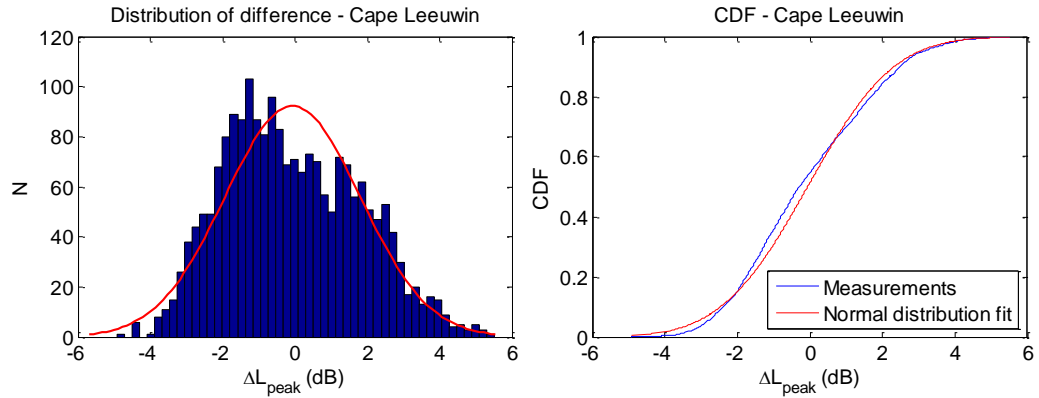


Fig. 5.5: Distribution of  $\Delta L_{peak}$  for Cape Leeuwin measurements and its best fit by a normal distribution. (a) Histogram and best-fit by normal Probability Density Function (PDF) (red line), (b) Cumulative Density Function (CDF). Parameters of the normal distribution fit: mean  $\mu = -0.07$  dB and standard deviation  $\sigma = 1.87$  dB. Results of K-S test:  $h = 1$ ,  $p = 0.000006$ ,  $\alpha = 0.05$ .

## 5.2.2 Dongara

$TL_E$  and  $TL_{peak}$  were calculated for the signals recorded from each of the six seismic tracks. They are shown in Fig 5.6 as a function of range.

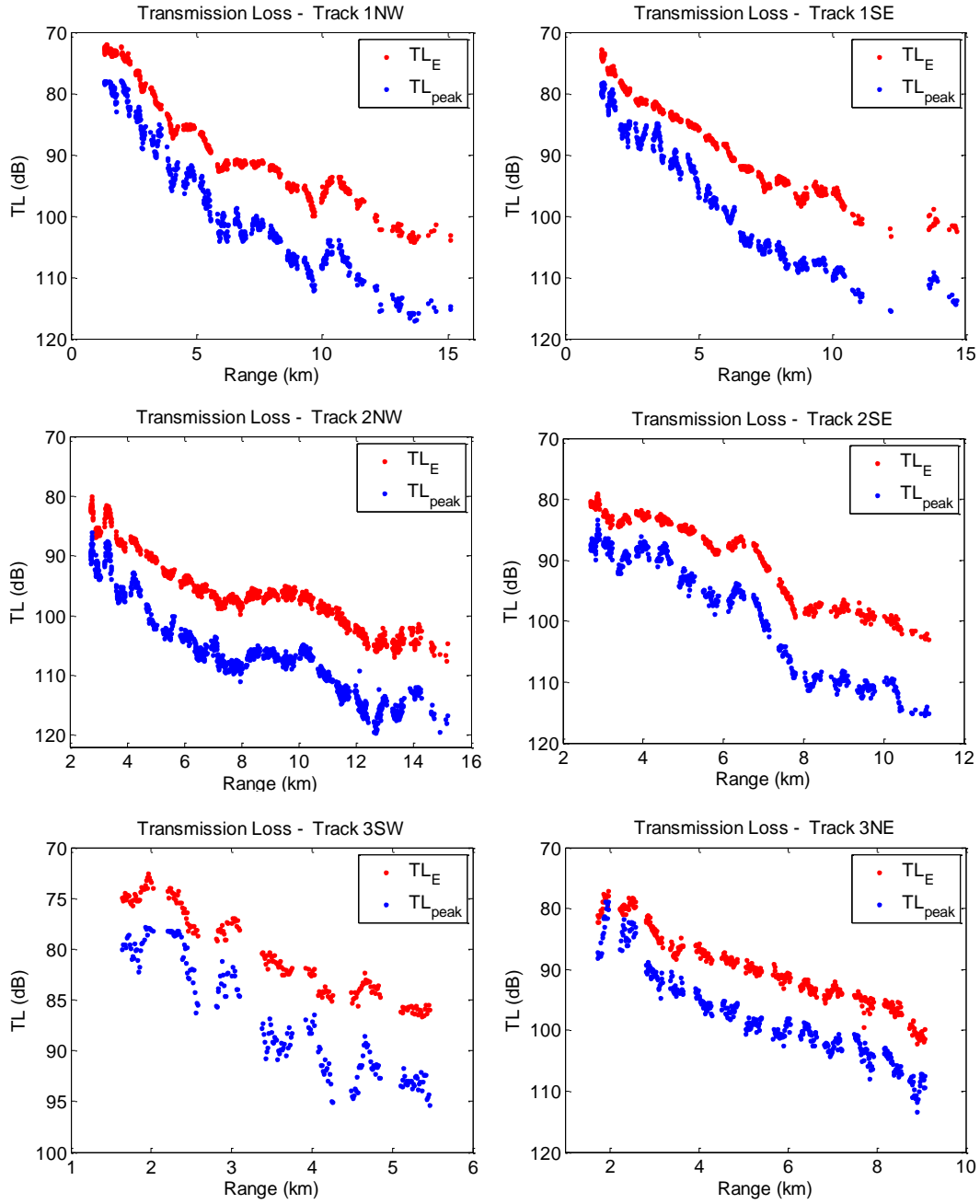


Fig. 5.6: Experimental transmission loss of the sound exposure and peak pressure levels for each of the six seismic tracks.

The analysis of the correlation between  $L_{peak}$  and  $SEL$  was separately done for each line. A linear dependence was newly observed, as expected (Fig. 5.7). Therefore,  $L_{peak}$  can be predicted using Eq. 5.1. The coefficients of the best linear fit for each track are shown in the Table 5.1, being  $A$  the slope,  $B$  the offset and  $RMSR$  the root-mean-square residual. The measured  $SEL$ ,  $L_{peak}$  and the  $L_{peak}$

predicted from  $SEL$  using Eq. 5.1 are plotted together in Fig. 5.8. The agreement between the empirical prediction and experimental data is good in general for all lines and ranges with the same exception for fluctuations, explained in the analysis of the previous data set.

Finally, the difference between the measurements and predictions of  $L_{peak}$  was calculated and its distribution was analysed. The results of the K-S test accept the hypothesis of normal distribution for all lines except for track 1NW. However, the value  $p$  for line 1NW is not small, which means that the hypothesis of rejection is not strong.

Table 5.1: Regression coefficients of Dongara data

Track	A	B (dB)	RMSR (dB)
1NW	1.244	-24.9	1.2
1SE	1.303	-32.5	1.4
2NW	1.213	-19.9	1.2
2SE	1.329	-35.3	1.2
3SW	1.284	-29.5	1.1
3NE	1.201	-17.2	1.4

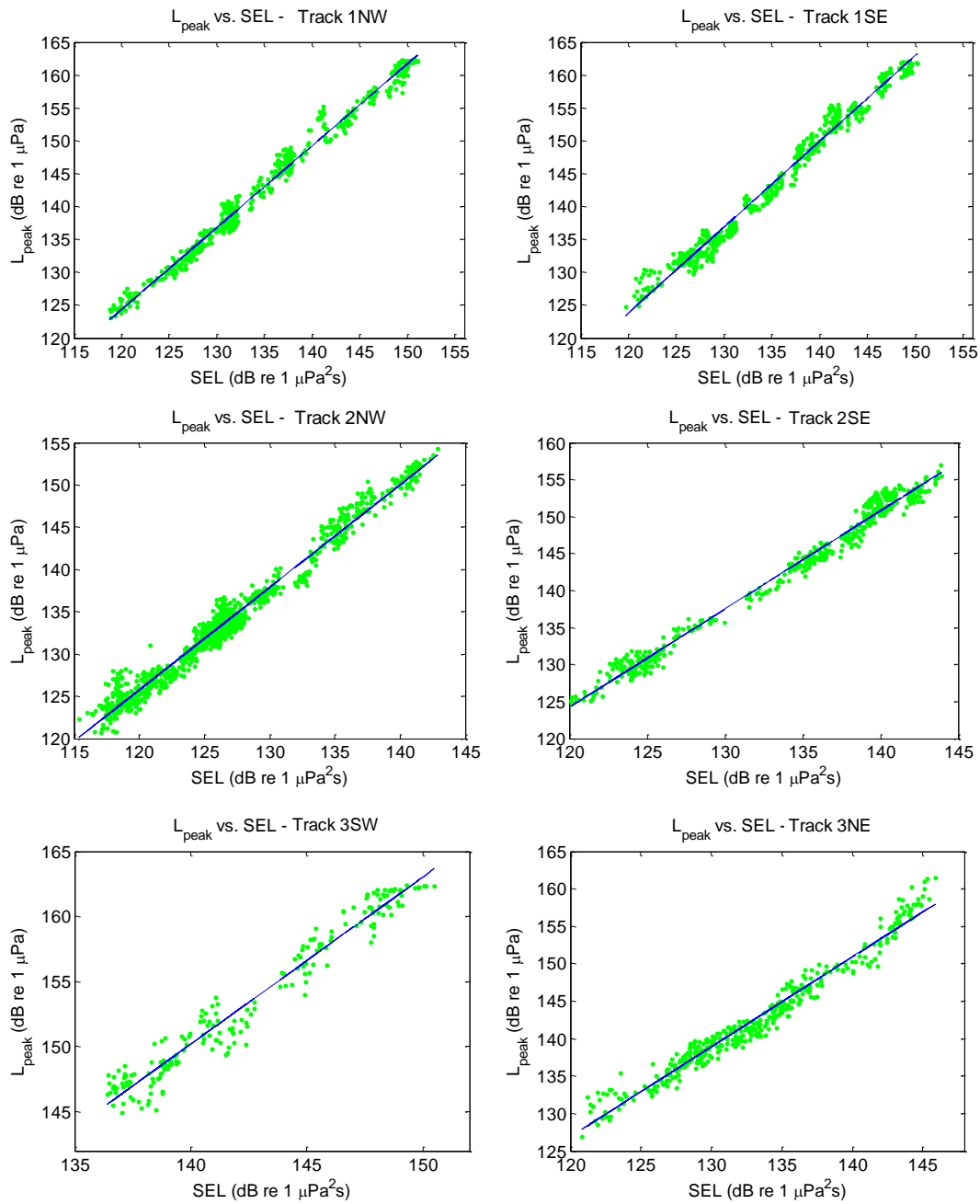


Fig. 5.7:  $L_{peak}$  vs.  $SEL$  and regression line for each of six selected tracks of the Dongara survey.

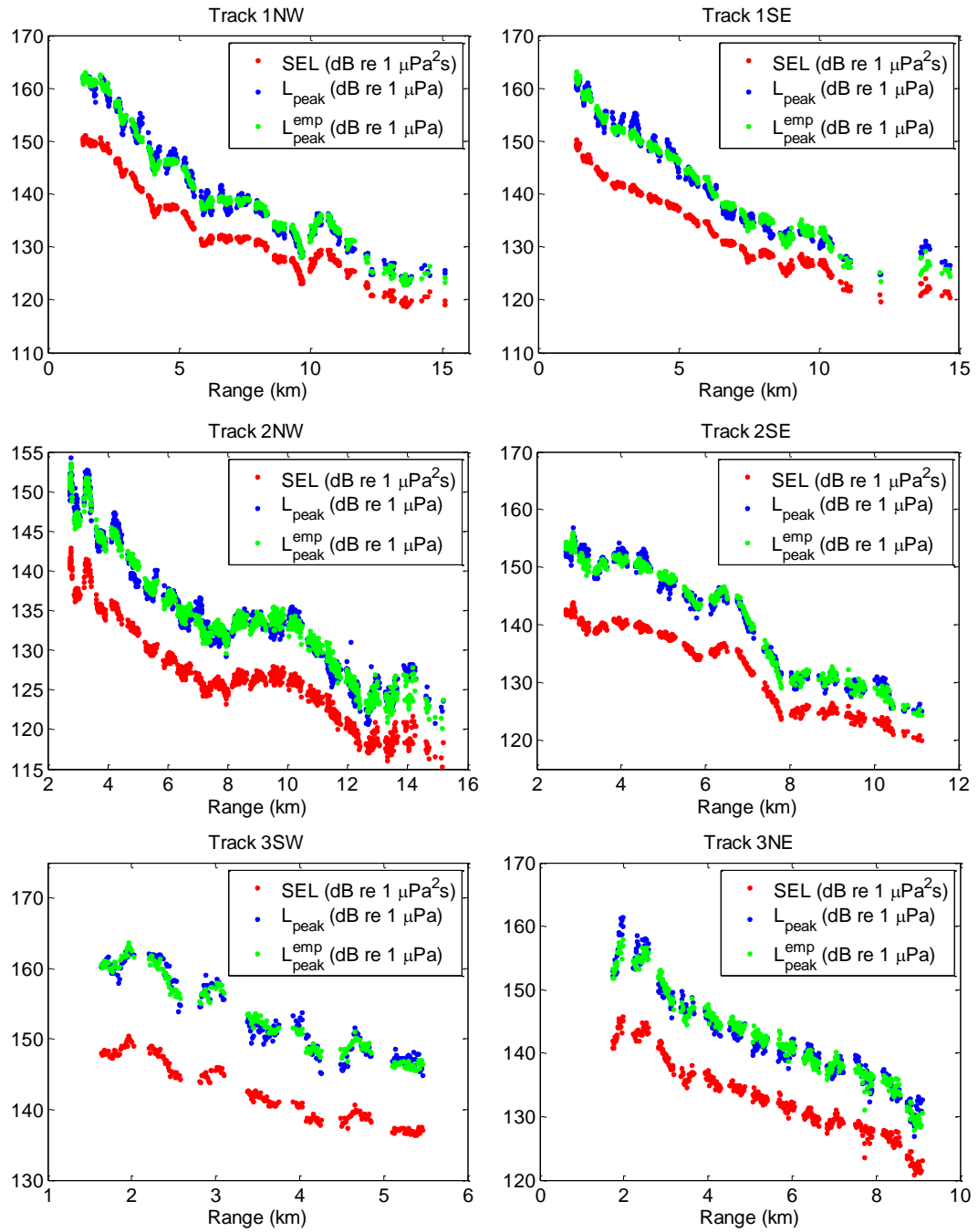


Fig. 5.8: Sound exposure level, peak pressure level and empirical predictions of peak pressure level for each selected line of the Dongara survey.

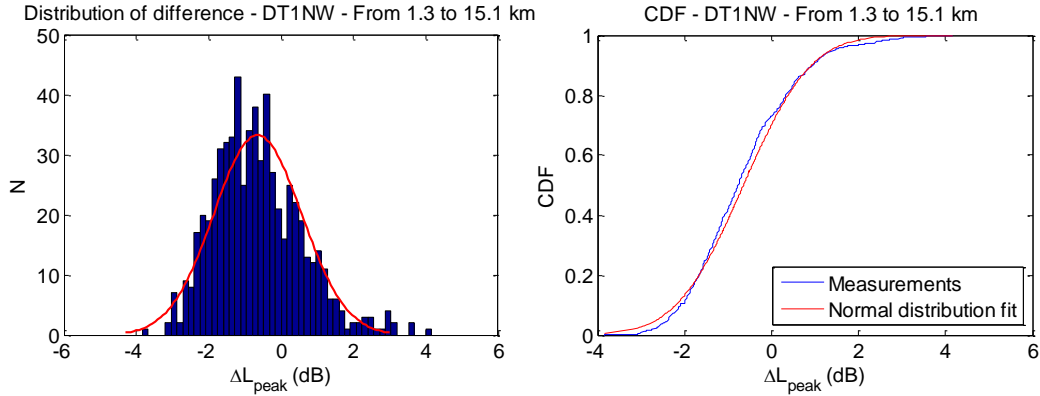


Fig. 5.9: Distribution of  $\Delta L_{peak}$  for Track 1NW of Dongara measurements. (a) Histogram of experimental data and best fit by normal PDF (red line), (b) CDF. Parameters of the normal distribution fit:  $\mu = -0.65$  dB,  $\sigma = 1.22$  dB. Parameters of K-S test:  $h = 1$ ,  $p = 0.025150$ ,  $\alpha = 0.05$ .

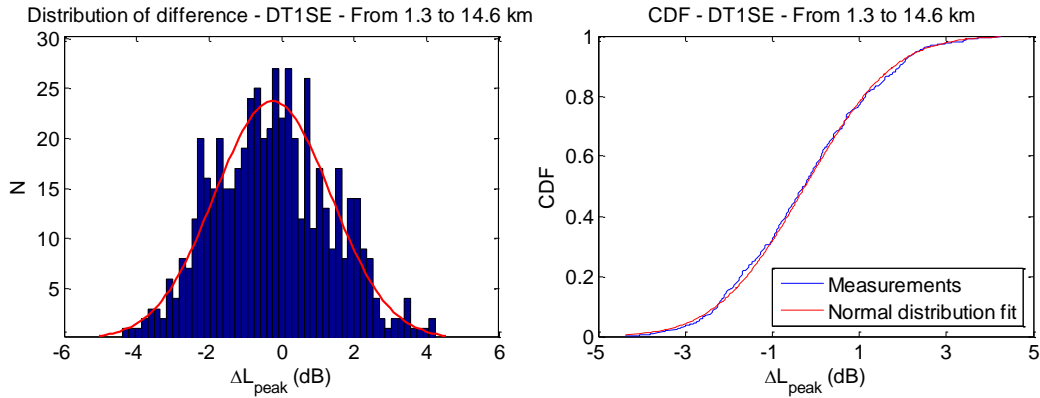


Fig. 5.10: Distribution of  $\Delta L_{peak}$  for Track 1SE of Dongara measurements. (a) Histogram of experimental data and best fit by normal PDF (red line), (b) CDF. Parameters of the normal distribution fit:  $\mu = -0.24$  dB,  $\sigma = 1.60$  dB. Parameters of K-S test:  $h = 0$ ,  $p = 0.618343$ ,  $\alpha = 0.05$ .

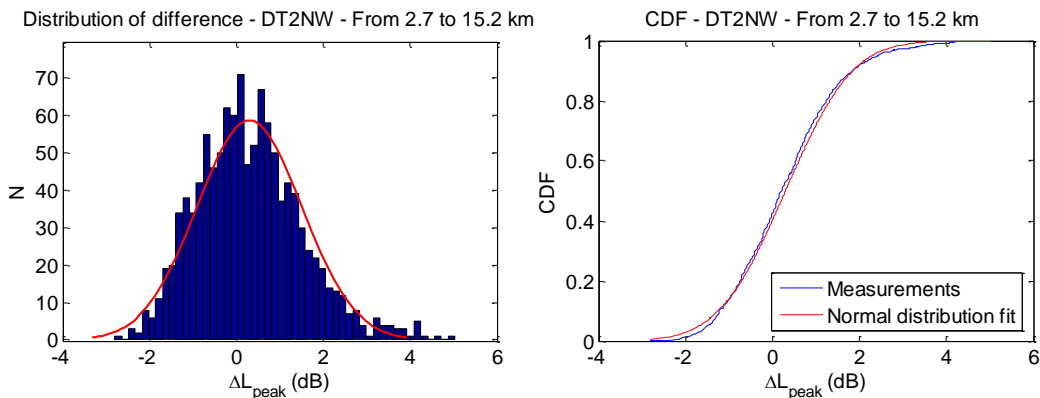


Fig. 5.11: Distribution of  $\Delta L_{peak}$  for Track 2NW of Dongara measurements. (a) Histogram of experimental data and best fit by normal PDF (red line), (b) CDF. Parameters of the normal distribution fit:  $\mu = 0.30$  dB,  $\sigma = 1.21$  dB. Parameters of K-S test:  $h = 0$ ,  $p = 0.110303$ ,  $\alpha = 0.05$ .

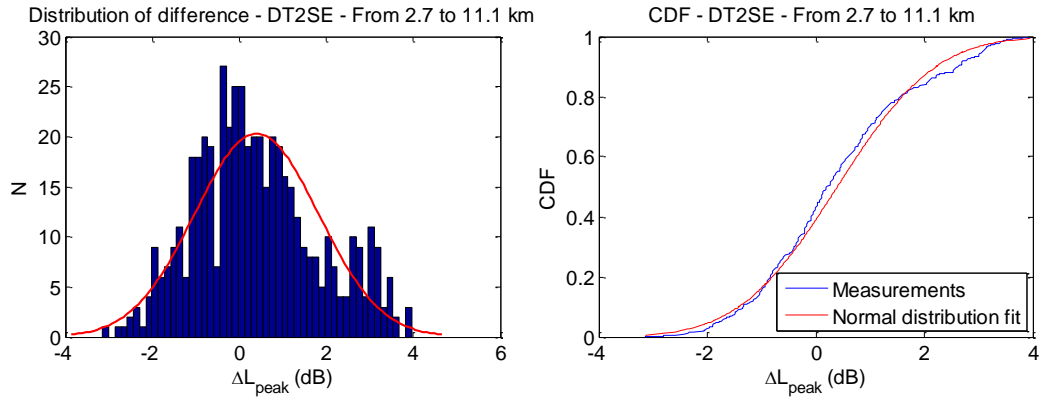


Fig. 5.12: Distribution of  $\Delta L_{peak}$  for Track 2SE of Dongara measurements. (a) Histogram of experimental data and best fit by normal PDF (red line), (b) CDF. Parameters of the normal distribution fit:  $\mu = 0.39$  dB,  $\sigma = 1.42$  dB. Parameters of K-S test:  $h = 0$ ,  $p = 0.070417$ ,  $\alpha = 0.05$ .

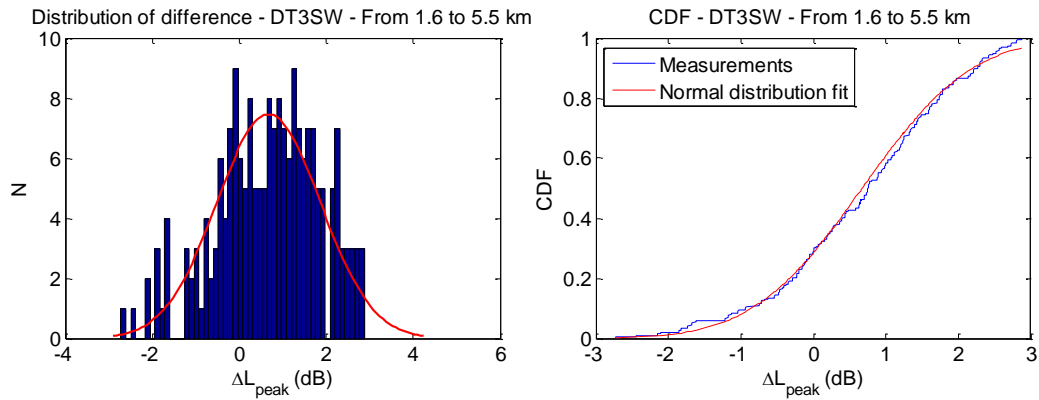


Fig. 5.13: Distribution of  $\Delta L_{peak}$  for Track 3SW of Dongara measurements. (a) Histogram of experimental data and best fit by normal PDF (red line), (b) CDF. Parameters of the normal distribution fit:  $\mu = 0.67$  dB,  $\sigma = 1.19$  dB. Parameters of K-S test:  $h = 0$ ,  $p = 0.664172$ ,  $\alpha = 0.05$ .

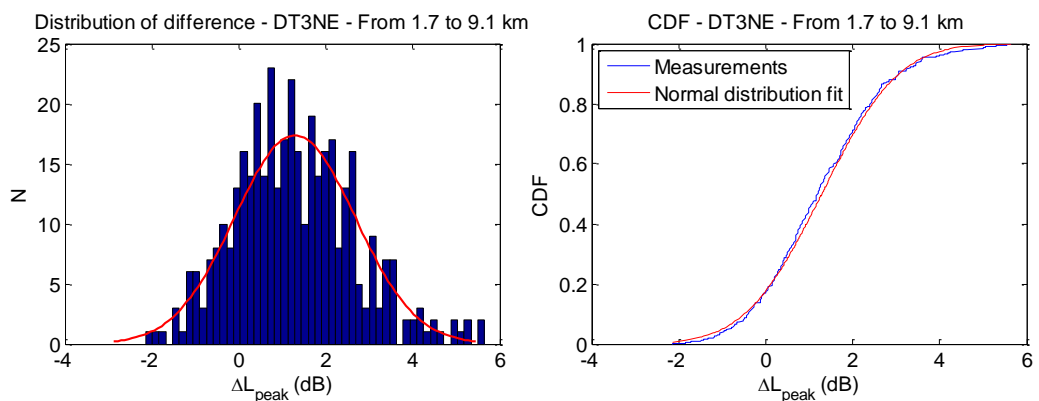


Fig. 5.14: Distribution of  $\Delta L_{peak}$  for Track 3NE of Dongara measurements. (a) Histogram of experimental data and best fit by normal PDF (red line), (b) CDF. Parameters of the normal distribution fit:  $\mu = 1.29$  dB,  $\sigma = 1.39$  dB. Parameters of K-S test:  $h = 0$ ,  $p = 0.607051$ ,  $\alpha = 0.05$ .

### 5.2.3 Bass Strait

$TL_E$  and  $TL_{peak}$  were calculated vs. range for each of the three tracks. They are represented in Fig. 5.15.

The measured values of  $L_{peak}$  were plotted against the corresponding values of  $SEL$  for each range (Fig. 5.16). Similarly to the previous analysis, a linear dependence was observed.  $L_{peak}$  can therefore be predicted from  $SEL$  using Eq. 5.1. The coefficients of the linear regression for each line are presented in Table 5.2. The values of the coefficients are very similar to those obtained in the previous analysis of airgun signals in the other two different environments.

The  $SEL$  and  $L_{peak}$  measured and the  $L_{peak}$  predicted from  $SEL$  using Eq. 5.1 are plotted together in Fig. 5.17. The agreement between the empirical predictions and the measurements is reasonably good. The distribution of  $\Delta L_{peak}$  is also analysed and the hypothesised normal distribution was accepted in all tracks based on the K-S test results.

Table 5.2: Regression coefficients of Bass Strait data.

Track	A	B (dB)	RMR (dB)
Track 1	1.241	-25.8	1.2
Track 2	1.222	-21.8	1.2
Track 3	1.175	-15.7	1.2

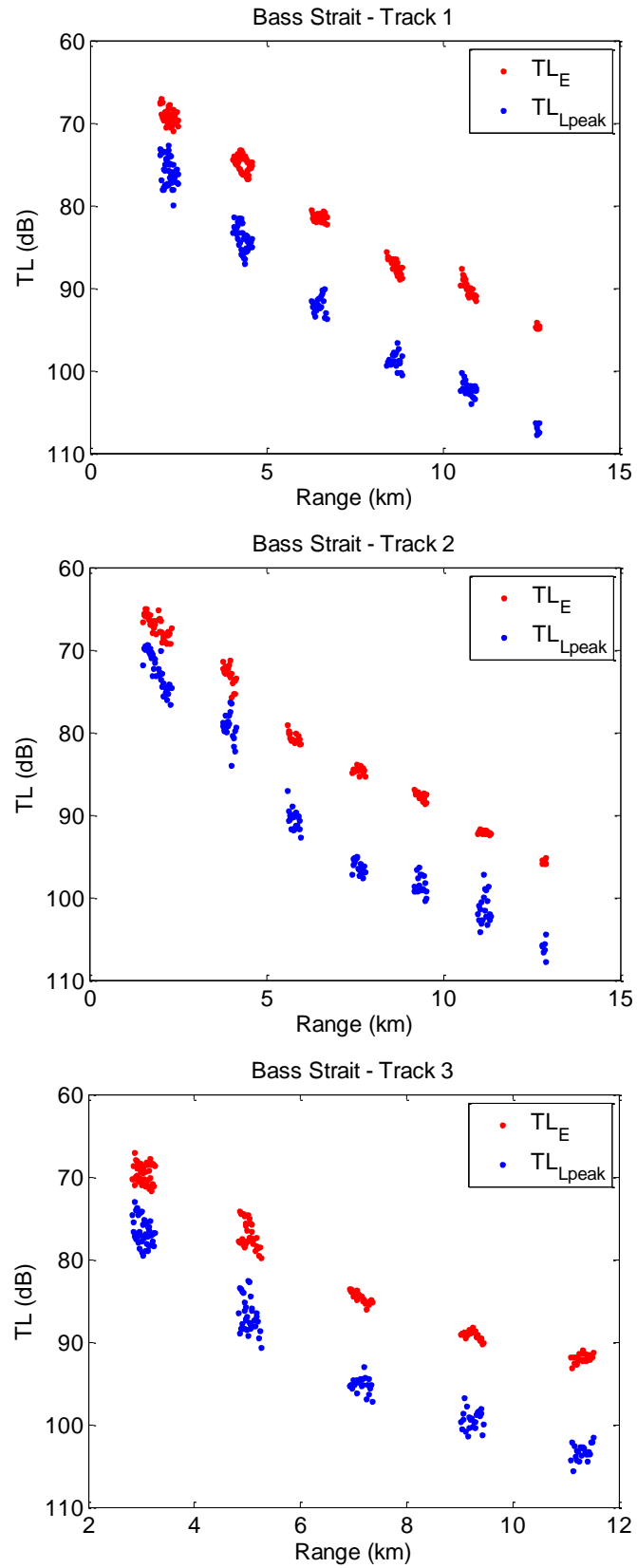


Fig. 5.15: Experimental transmission loss of the sound exposure and the peak pressure levels measured in Bass Strait: Track 1 (top), Track 2 (centre), and Track 3 (bottom).

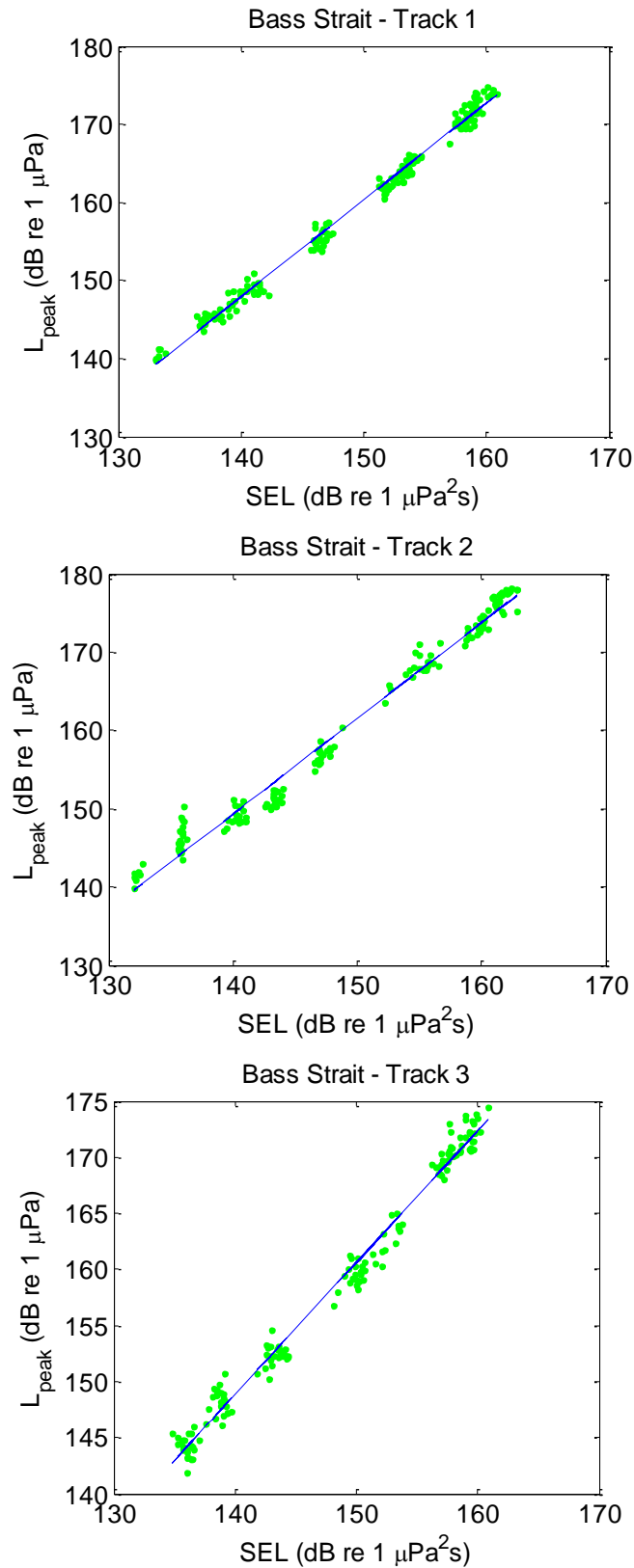


Fig. 5.16:  $L_{peak}$  vs.  $SEL$  and regression line from Bass Strait data: Track 1 (top), Track 2 (centre), and Track 3 (bottom).

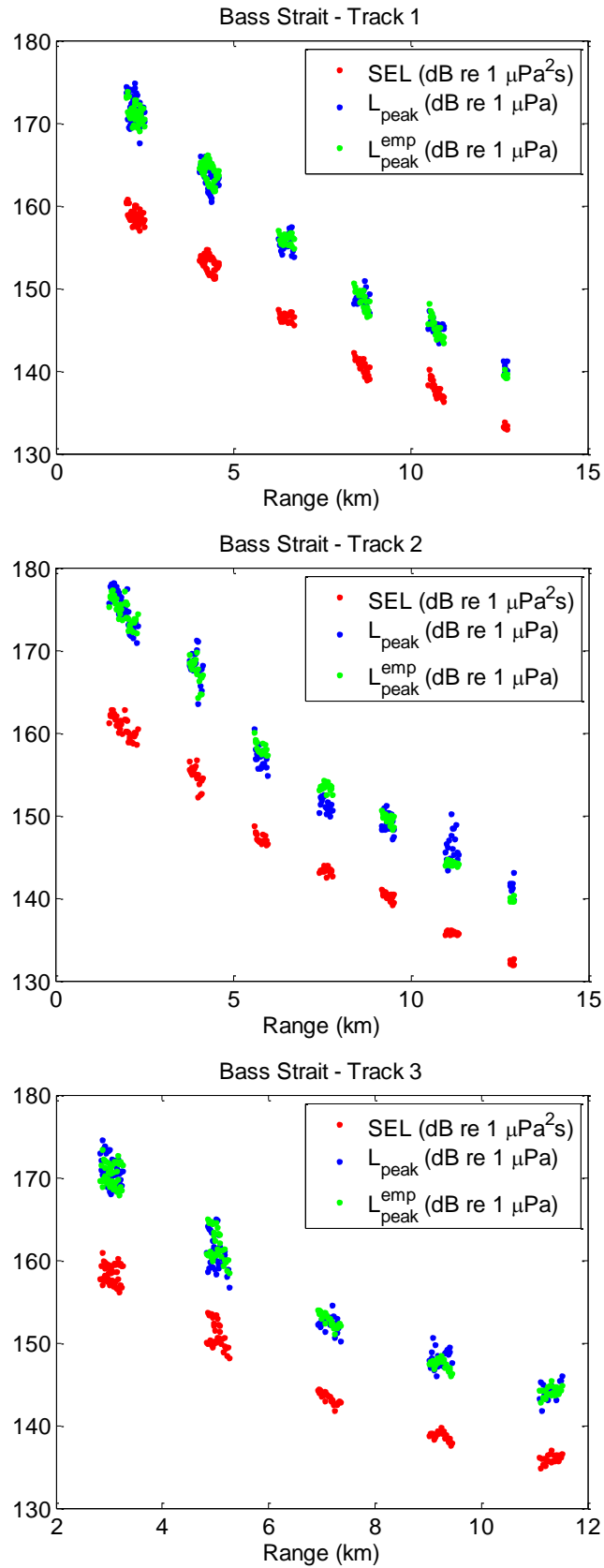


Fig. 5.17:  $SEL$  (red), measured  $L_{peak}$  (blue) and empirical predictions of  $L_{peak}$  (green) from Bass Strait data. Track 1 (top), Track 2 (centre), and Track 3 (bottom).

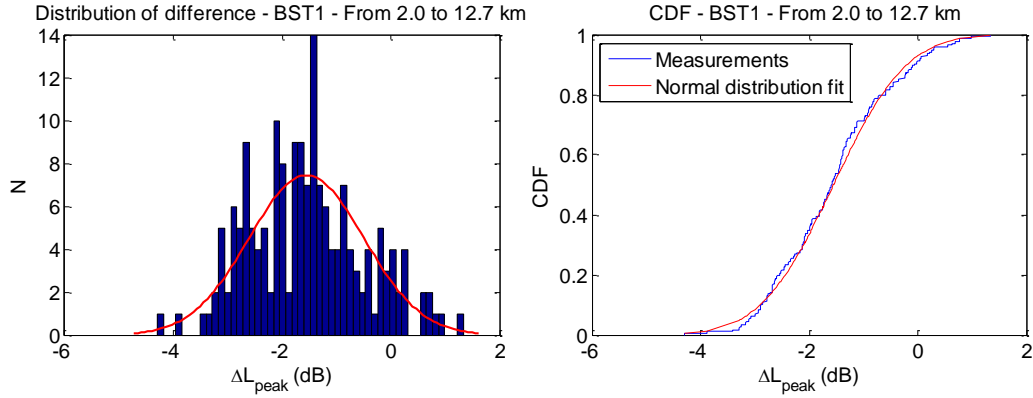


Fig. 5.18: Distribution of  $\Delta L_{peak}$  for Track 1 of Bass Strait measurements. (a) Histogram of experimental data and best fit by normal PDF (red line), (b) CDF. Parameters of the normal distribution fit:  $\mu = -1.55$  dB,  $\sigma = 1.06$  dB. Parameters of K-S test:  $h = 0$ ,  $p = 0.553056$ ,  $\alpha = 0.05$ .

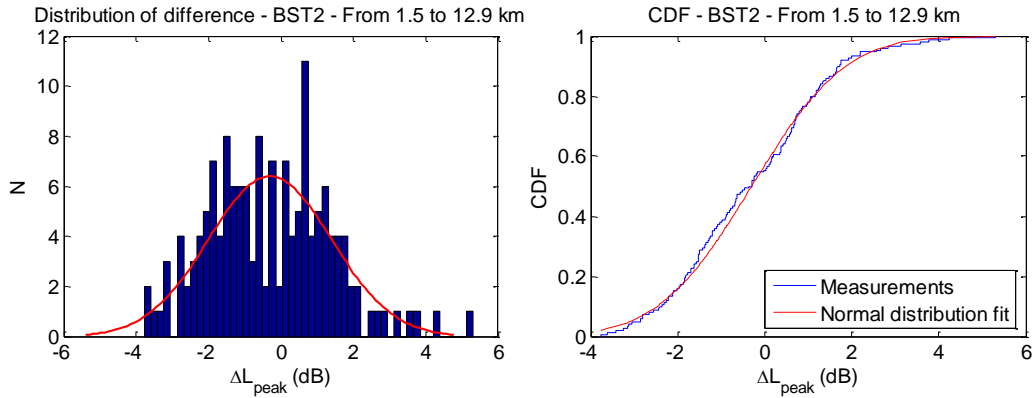


Fig. 5.19: Distribution of  $\Delta L_{peak}$  Track 3 of Bass Strait measurements. (a) Histogram of experimental data and best fit by normal PDF (red line), (b) CDF. Parameters of the normal distribution fit:  $\mu = -0.30$  dB,  $\sigma = 1.69$  dB. Parameters of K-S test:  $h = 0$ ,  $p = 0.747970$ ,  $\alpha = 0.05$ .

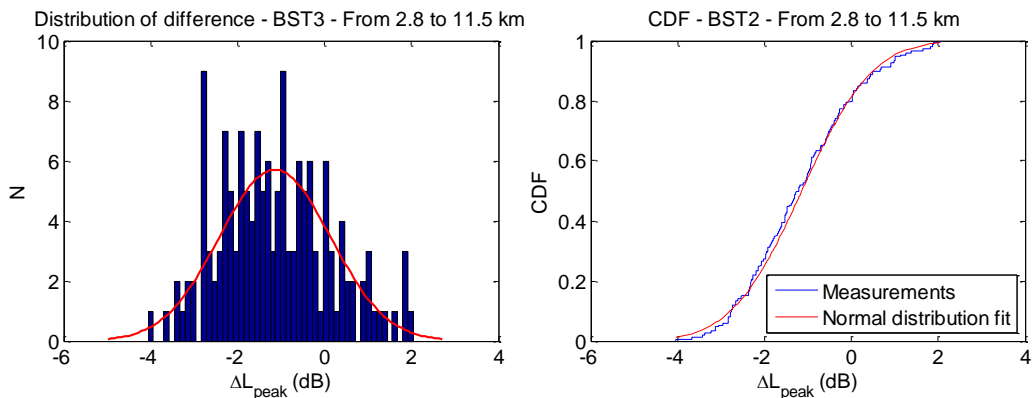


Fig. 5.20: Distribution of  $\Delta L_{peak}$  for Track 3 of Bass Strait measurements. (a) Histogram of experimental data and best fit by normal PDF (red line), (b) CDF. Parameters of the normal distribution fit:  $\mu = -1.14$  dB,  $\sigma = 1.28$  dB. Parameters of K-S test:  $h = 0$ ,  $p = 0.849395$ ,  $\alpha = 0.05$ .

## 5.2.4 Discussion

The analysis of airgun signals from the three seismic surveys leads to the following conclusions:

1. There is strong correlation between  $SEL$  and  $L_{peak}$  in all environments. Therefore, a linear empirical equation can be used to relate both units and predict  $L_{peak}$  from  $SEL$ .
2. The values of the coefficients  $A$  from the linear regressions result from the physics of sound propagation in an ocean channel. They were found to be nearly independent of the environment.
3. The values of the coefficient  $B$  obtained from the linear regression are very similar for the surveys conducted in different marine environments. These values are expected to be dependent primarily on the sound source parameters rather than characteristics of the underwater sound channel, which will be discussed in Chapter 6.
4. The results of the K-S tests for the distributions of  $\Delta L_{peak}$  for each individual track in all three environments showed that the variations of  $\Delta L_{peak}$  could be reasonably well approximated by the normal distribution, with two exceptions - the track off Cape Leeuwin, and track 1NW of the Dongara survey. In the former case, despite the rejection of the normal distribution hypothesis, the CDF shows a similarity between measurements and modelled normal distribution. In the latter case, the value obtained for  $p$  was not small, which means that the hypothesis of normal distribution was rejected, but not strongly.

## 5.3 Generalised analysis of data sets

### 5.3.1 Overview

All data presented in section 5.3 were combined to create a new set referred to

as a “Combined data set”, presented in Table 5.3.

The mean values of the regression coefficients and their standard deviation for all tracks in all three surveys are:  $\langle A \rangle = 1.25 \pm 0.05$  and  $\langle B \rangle = -24 \pm 6$  dB re 1  $\mu$ Pa. These values indicate that the slope of the linear regression does not experience significant variations, but the offsets is subject to relatively large variation. However, such large variation of the offset  $B$  resulted from the reference point in the linear regression (Eq. 5.1) being at  $SEL = 0$  dB. However, the actual  $SEL$  values of the measured signal vary from 115 to 163 dB, which is an interval significantly distant from 0 dB. Therefore, any slight change in the slope  $A$  will cause a big change in the offset  $B$ , but will not result in a significant change in  $L_{peak}^{emp}$  within the interval of the observed  $SEL$  variation. So, the selection of the reference point for the offset  $B$  within this interval should significantly reduce the offset variation. This can be expressed by a modified linear equation Eq. 5.2, equivalent to Eq. 5.1 as follows:

$$L_{peak}^{emp} = A \cdot (SEL - C) + B'. \quad (5.2)$$

In this equation, the constant  $C$  is chosen to be the mean value of the  $SEL$  variation:  $C = \langle SEL \rangle = 135$  dB re 1  $\mu$ Pa<sup>2</sup> s, and  $B'$  is the new offset, which is the value of  $L_{peak}$  where  $SEL = C$ . The values of  $B'$  for each track are also shown in Table 5.3. The mean and standard deviation were calculated and the result was  $\langle B' \rangle = 143.3 \pm 0.8$  dB re 1  $\mu$ Pa. The variation in the offset changed from 6 dB to 0.8 dB just by changing the reference point in  $SEL$  from 0 dB to its average value of 135 dB.

The pairs of regression coefficients in Eq. 5.2 are indeed similar for all tracks in all locations. This suggests that a common set of the regression coefficients can be used to predict  $L_{peak}$  from  $SEL$  for all locations analysed in this study. The goal is obtaining an equation with generalised coefficients that can be applied to predict  $L_{peak}$  of airgun array signals in different marine environments.

Equation 5.2 was tested for all environments previously studied, and the goodness of the fit is discussed using a statistical approach.

Table 5.3: Experimental data from all surveys.

<b>Data</b>	<b>Number of Shots</b>	<b>Range (km)</b>	<b>A</b>	<b>B (dB)</b>	<b>B' (dB)</b>	<b>RMSR (dB)</b>
<b>Cape Leeuwin</b>	2071	16.9-94.3	1.241	-24.0	143.4	1.9
<b>Dongara - Track 1NW</b>	634	1.3-15.1	1.244	-24.9	142.5	1.2
<b>Dongara - Track 1SE</b>	551	1.3-14.6	1.303	-32.5	143.0	1.4
<b>Dongara - Track 2NW</b>	1137	2.7-15.2	1.213	-19.9	143.5	1.2
<b>Dongara - Track 2SE</b>	509	2.7-11.1	1.329	-35.3	144.3	1.2
<b>Dongara - Track 3SW</b>	199	1.6-5.5	1.284	-29.5	143.3	1.1
<b>Dongara - Track 3NE</b>	388	1.7-9.1	1.201	-17.2	144.0	1.4
<b>Bass strait - Track 1</b>	175	2.0-12.7	1.241	-25.8	141.6	1.2
<b>Bass strait - Track 2</b>	150	1.5-12.9	1.222	-21.8	142.9	1.2
<b>Bass strait - Track 3</b>	150	2.8-11.5	1.175	-15.7	143.6	1.2

### 5.3.2 Analysis

The measurements of  $L_{peak}$  are plotted against the  $SEL$  in Fig. 5.21. All pairs  $(SEL, L_{peak})$  from the surveys presented in Table 5.3 (column 1) are included as a single set, without distinguishing the origin.

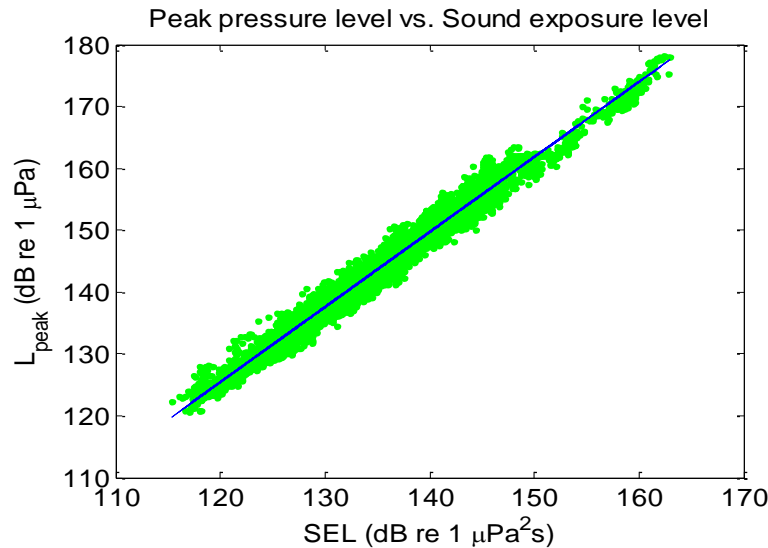


Fig. 5.21: Experimental  $L_{peak}$  vs.  $SEL$  in dB (green dots) and the linear regression line (blue) from all measurement data.

It must be noted that now the coefficients obtained from the best linear fit are not specific to any site, they are generalised regression coefficients. Their values are  $A_G = 1.213$  and  $B_G = -20.1$  dB re 1  $\mu\text{Pa}$ , obtained with a root-mean-square residual of 1.6 dB and a 95% confidence interval of  $\pm 0.005$  and  $\pm 0.6$  dB for  $A_G$  and  $B_G$  respectively ( $R^2$  statistic value of 0.9771). These coefficients are equivalent to the coefficients  $A = 1.213$ ,  $B' = 143.3$  dB re 1  $\mu\text{Pa}$  and  $C = 135$  dB re 1  $\mu\text{Pa}^2 \cdot \text{s}$  in Eq. 5.2.

### 5.3.3 Application of the generalised equation to all environments

The empirical prediction of  $L_{peak}$  from the  $SEL$  measurements using Eq. 5.1

was verified for all tracks, using the generalised coefficients  $A_G$  and  $B_G$  and, for comparison, the specific coefficients  $A$  and  $B$  obtained for each track. Figures 5.22 to 5.24 show the prediction results for each environment compared to the experimental data. It can be seen that the predictions of  $L_{peak}$  with the generalised coefficients in Eq. 5.1 is as nearly as good as the predictions using the specific coefficients for each environment. The results suggest that there is no need to obtain new specific coefficients  $A$  and  $B$  for each survey. The empirical equation with the generalised coefficients can offer a good approximation for the prediction of  $L_{peak}$  of airgun signals, independently of the environment, as seen in the results. However, further testing with data from other seismic surveys is required.

Let us notice that the linear dependence and regression coefficients found from this analysis are valid for measurement ranges from about 1 km to nearly 100 km. At shorter distance, where multipath and/or scattering effects are not determinative, the correlation between  $L_{peak}$  and  $SEL$  can be somewhat different. Additional measurements from different seismic surveys are needed to examine this correlation, particularly at shorter distances.

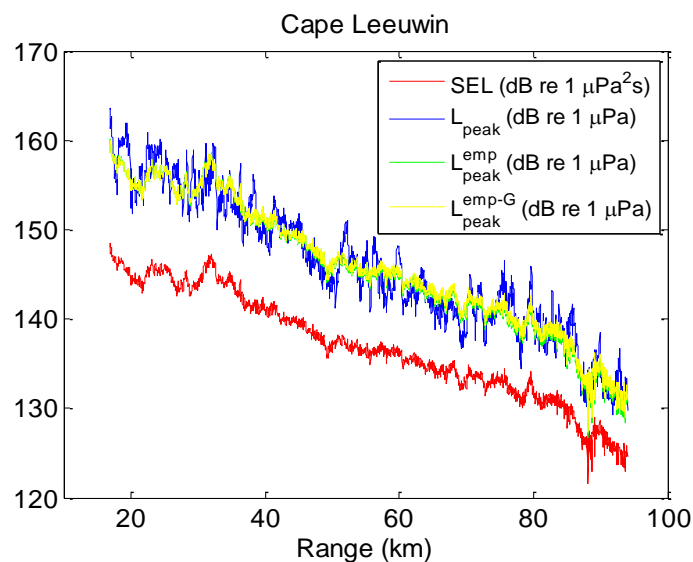


Fig. 5.22: Measured sound exposure level (red), measured peak pressure level (blue), empirical prediction of peak pressure level from  $SEL$  with the specific regression coefficients (green), and empirical prediction of peak pressure level from  $SEL$  with the generalised regression coefficients (yellow) in Eq. 5.1 for the Cape Leeuwin data.

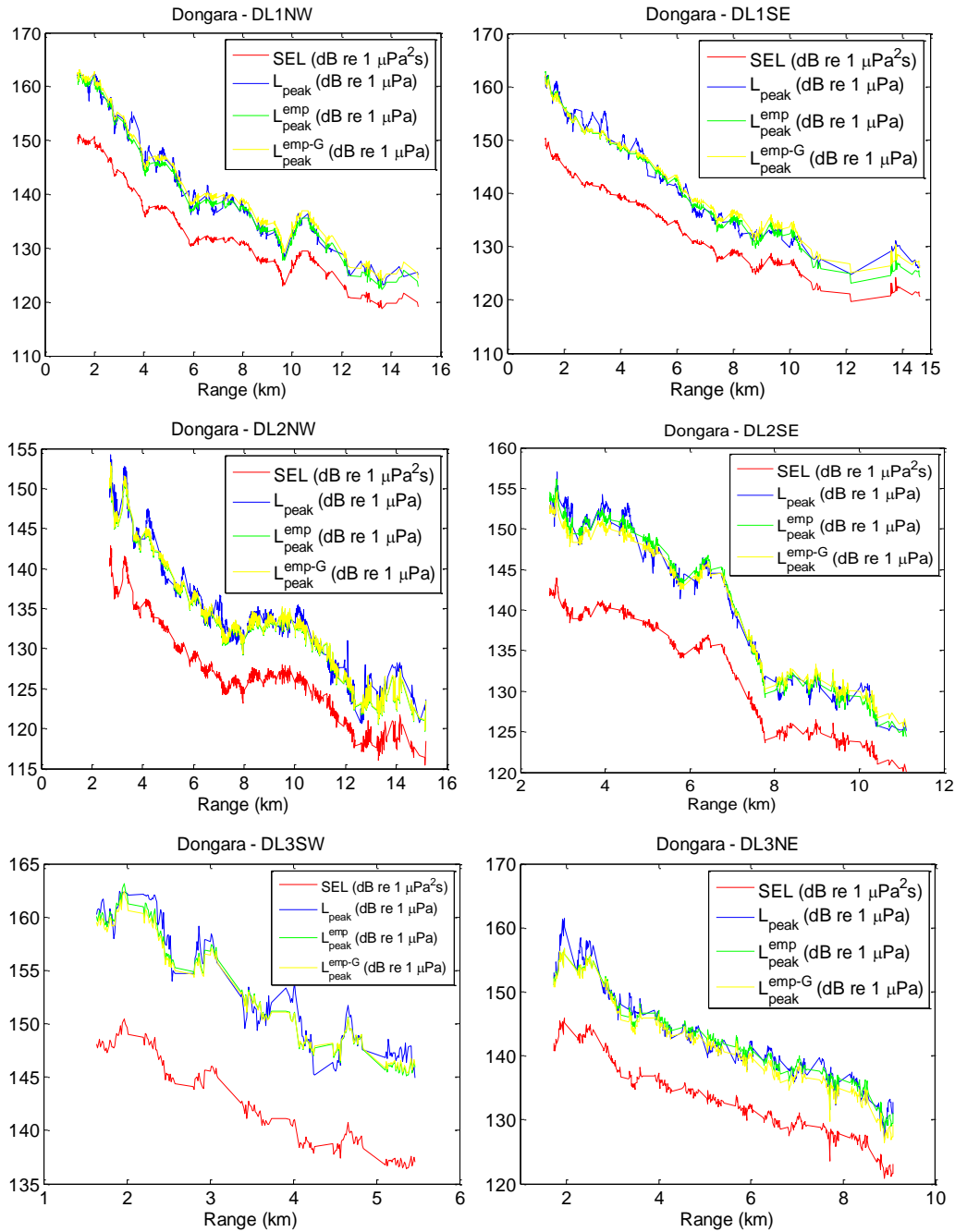


Fig. 5.23: Measured sound exposure level (red), measured peak pressure level (blue), empirical prediction of peak pressure level with the specific regression coefficients (green), and empirical prediction of peak pressure level with the generalised regression coefficients (yellow) for all tracks of the Dongara data set.

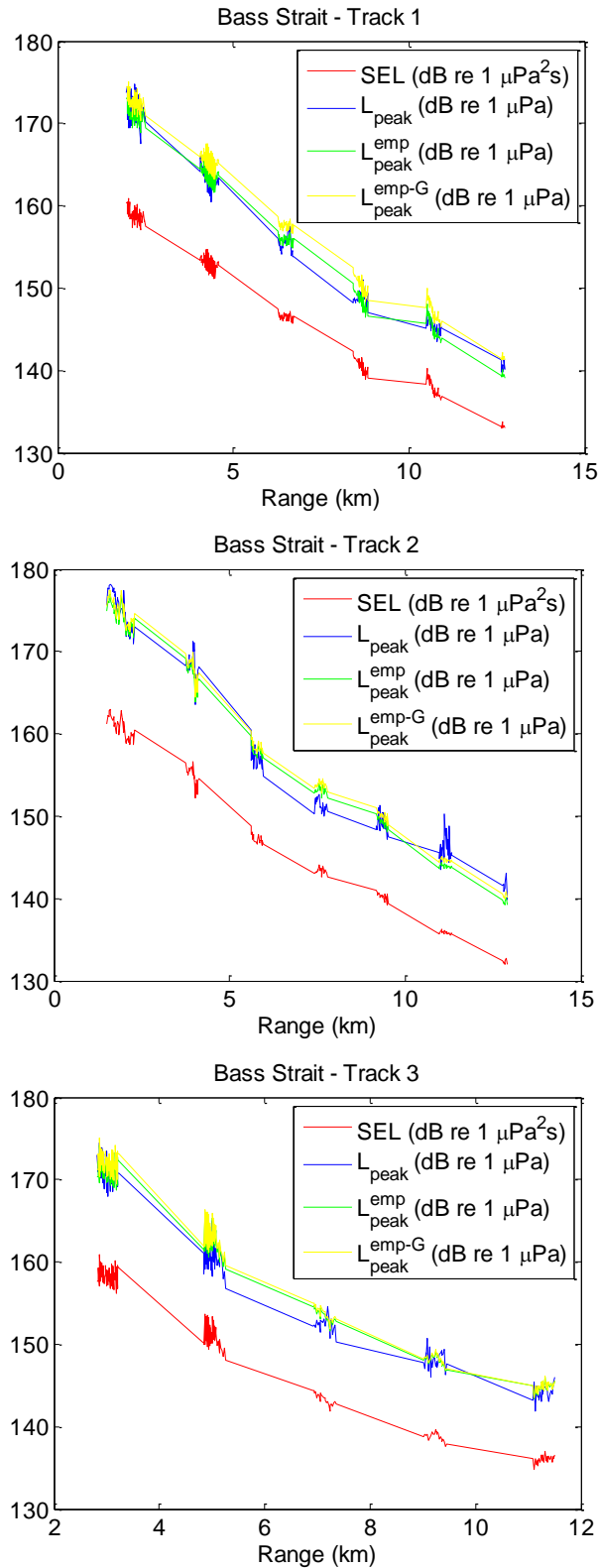


Fig. 5.24: Measured sound exposure level (red), measured peak pressure level (blue), empirical prediction of peak pressure level with the specific regression coefficients (green), and empirical prediction of peak pressure level with the generalised regression coefficients (yellow) for Tracks 1 (top), 2 (centre) and 3 (bottom) of the Bass Strait measurements.

### 5.3.4 Statistical analysis

The difference  $\Delta L_{peak}$  between the measured and empirically predicted peak pressure levels was calculated for the generalised data set and its distribution was analysed, following the same procedure as for the individual data sets. The analysis was done for different groups of data:

- Firstly, for the combined data in the entire range span.
- Secondly, for different range intervals.

The results obtained for the parameters of the normal distribution, mean  $\mu$  and standard deviation  $\sigma$ , and the results of the Kolmogorov-Smirnov test,  $h$  and  $p$ , are presented on Table 5.4. They are also indicated in the caption of each figure.

Table 5.4: Parameters of normal distribution fit and K-S test for generalised data set at different ranges.

Range (km)		$\bar{\mu}$ (dB)	$\bar{\sigma}$ (dB)	$h$	$p$
<b>All</b>	[1.3, 94.0]	0.00	1.64	1	0.000666
<b>Short</b>	[1.3, 15.0]	0.04	1.50	0	0.080153
<b>Medium</b>	[15.0, 68.0]	-0.12	1.90	1	0.000006
<b>Long</b>	[68.0, 94.0]	0.04	1.81	0	0.073123

#### Distribution of $\Delta L_{peak}$ for all data

The distribution of the difference  $\Delta L_{peak}$  for the combined data set in the entire range span is presented in Fig. 5.25. The result of the K-S test indicates that the hypothesized normal distribution is rejected at the confidence level  $\alpha = 0.05$ .

It can be observed in the histogram that the distribution is slightly skewed and this is the major cause of the rejection. However, looking at the CDF plot, one can see no significant difference between the measured and the hypothesized normal CDFs. Therefore, we could say that a normal distribution with  $\mu = 0.00$  dB,  $\sigma = 1.64$  dB offers a reasonable approximation for the combined data set, and hence, the value of the 68% of the  $\Delta L_{peak}$  will likely lie within the interval  $(\mu - \sigma, \mu + \sigma)$ , which is  $\pm 1.64$  dB.

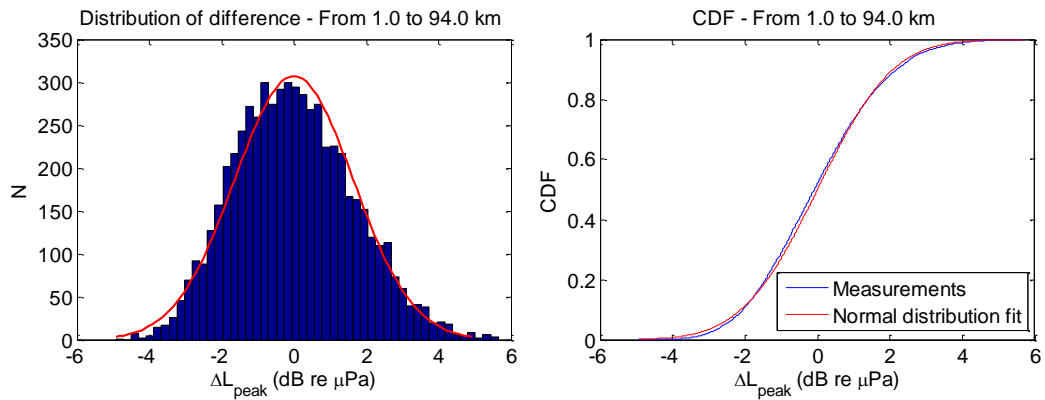


Fig. 5.25: Distribution of  $\Delta L_{peak}$  with all data and fit to a normal distribution. (a) Histogram of measure data and its best fit by normal distribution PDF (red line), (b) CDF. Parameters of the normal distribution fit:  $\mu = 0.00$  dB,  $\sigma = 1.64$  dB. Parameters of K-S test:  $h = 1$ ,  $p = 0.000666$  with  $\alpha = 0.05$ .

### Distribution of $\Delta L_{peak}$ in different range intervals

The combined data set is not uniformly distributed with range, as it is shown in Fig. 5.26. The number of recordings made at shorter distances was significantly larger than that at longer distances.

The results of analysis for different range intervals specified in Table 5.4 are shown in Figures from 5.27 to 5.29. These results demonstrate that a normal distribution is a good approximation for the data at short and long ranges, based on the results of the K-S test. This is evident for short ranges where the histogram reveals a shape resembling a normal distribution, but it is not that evident from the histogram for long ranges. At long ranges, the amount of data is not big enough to show a well-defined shape for the histogram, but the CDF follows very closely the theoretical normal fit for the distribution. In the case of medium

ranges, the K-S test rejects the hypothesized normal distribution with a confidence level of  $\alpha = 0.05$ . Despite the different verdict regarding the hypothesis, the result is very similar to the long ranges case, where not many data were available. The experimental CDF shows slightly larger deviation from the hypothesized CDF, but the normal distribution CDF could be used to approximate it.

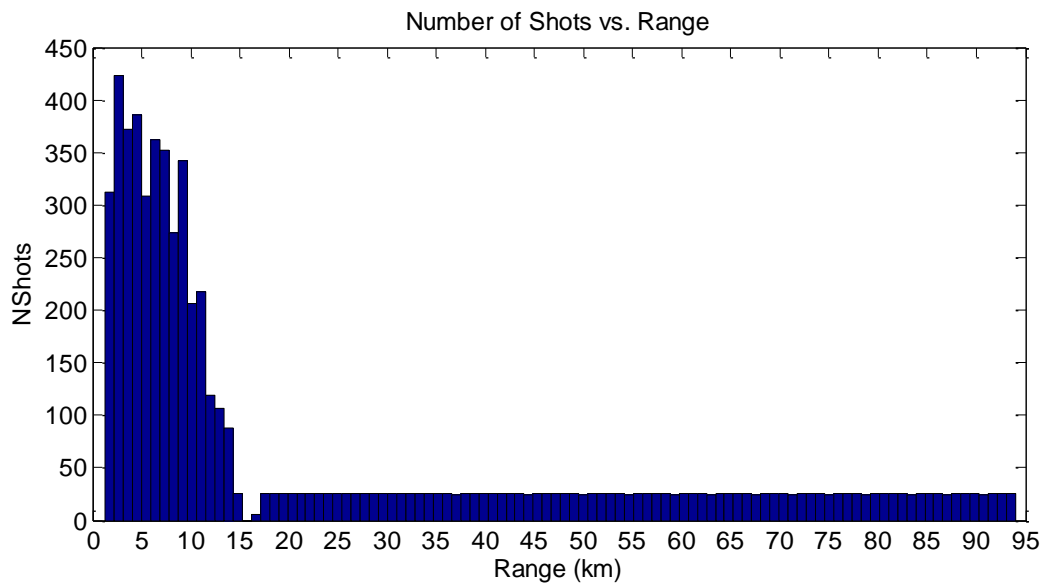


Fig. 5.26: Distribution of the number of shots with range from all tracks used for analysis.

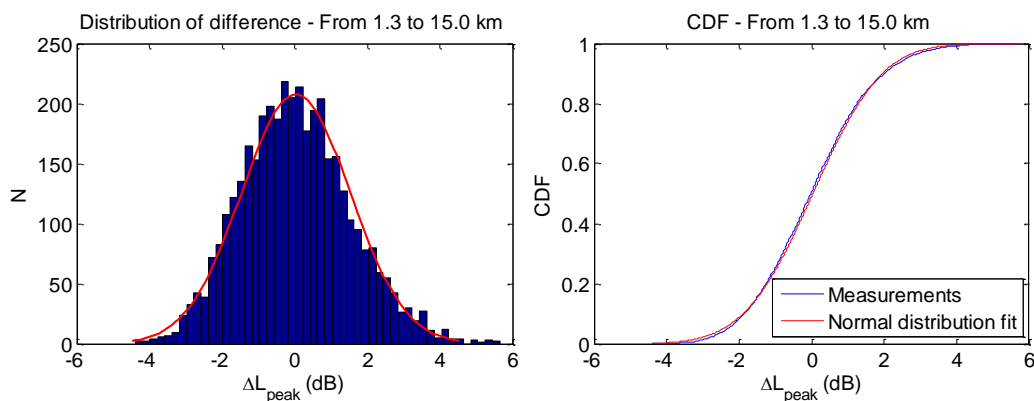


Fig. 5.27: Distribution of  $\Delta L_{peak}$  for short ranges (in the range interval [1.3, 15.0] km) and fit to a normal distribution. (a) Histogram of measure data and its best fit by normal distribution PDF (red line), (b) CDF. Parameters of the normal distribution fit:  $\mu = 0.04$  dB,  $\sigma = 1.50$  dB. Parameters of K-S test:  $h = 0$ ,  $p = 0.080153$ ,  $\alpha = 0.05$ .

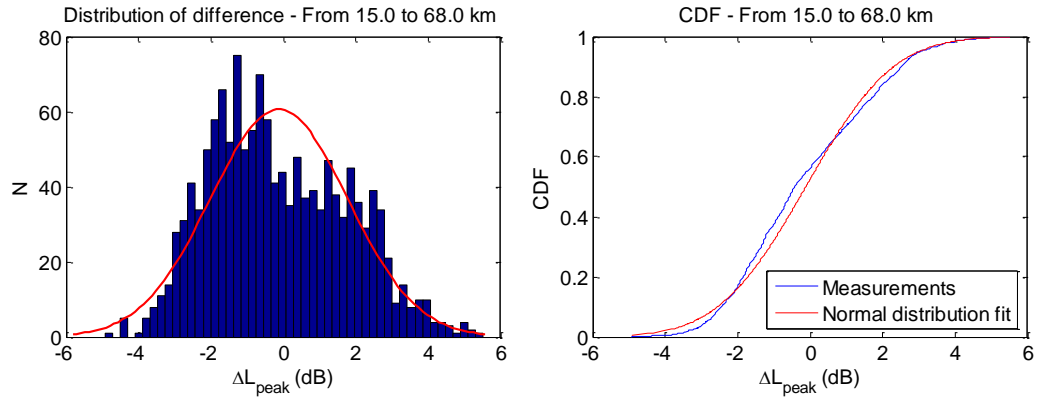


Fig. 5.28: Distribution of  $\Delta L_{peak}$  for medium ranges (in the range interval [15.0, 68.0] km) and fit to a normal distribution. (a) Histogram of measure data and its best fit by normal distribution PDF (red line), (b) CDF. Parameters of the normal distribution fit:  $\mu = -0.12$  dB,  $\sigma = 1.90$  dB.

Parameters of K-S test:  $h = 1$ ,  $p = 0.000006$ ,  $\alpha = 0.05$ .

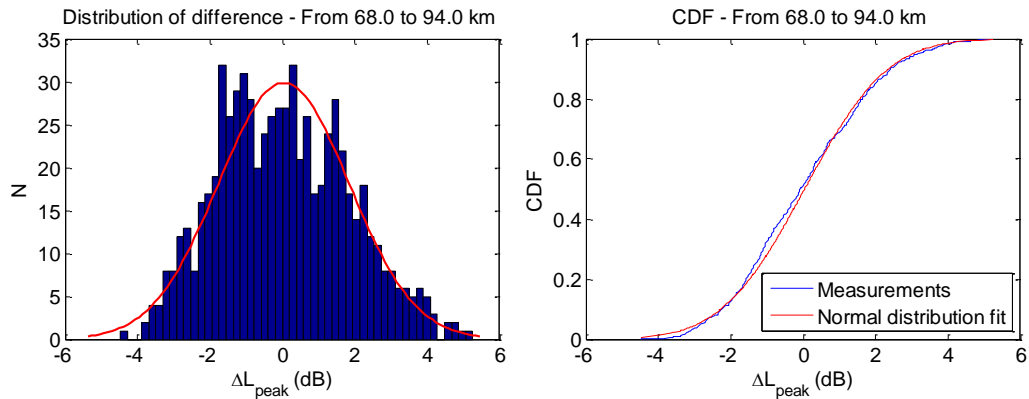


Fig. 5.29: Distribution of  $\Delta L_{peak}$  in the range interval [68.0, 94.0] km and fit to a normal distribution. (a) Histogram of measure data and its best fit by normal distribution PDF (red line), (b) CDF. Parameters of the normal distribution fit:  $\mu = 0.03$ ,  $\sigma = 1.81$  dB. Parameters of K-S test:  $h = 0$ ,  $p = 0.073123$ ,  $\alpha = 0.05$ .

## 5.4 Semi-empirical prediction

The previous sections of this chapter showed how the empirical equation (Eq. 5.1) with the generalised regression coefficients  $A_G$  and  $B_G$  can be used to predict  $L_{peak}$  from  $SEL$  measurements. This section presents a method to predict  $L_{peak}$ , using Eq. 5.1, when measurements of  $SEL$  are not available, which was the main goal of this project.

The method presented here is based on:

1. The capability of the existing underwater sound propagation models to predict  $SEL$  with a sufficient accuracy when the environmental parameters are known, as demonstrated in section 2.4.1.
2. The use of the empirical linear equation (Eq. 5.1) with the generalised coefficients  $A_G$  and  $B_G$ .

### 5.4.1 Description of the algorithm

The method proposed to predict  $L_{peak}$ , referred to as “semi-empirical prediction” consists of three main steps (see Fig. 5.30).

1. The sound field of the airgun array is modelled at different ranges using an appropriate underwater sound channel model, including the water column and bottom, and an appropriate underwater acoustic propagation model for the corresponding environment.
2.  $SEL$  is calculated as a function of range.
3. To predict the mean (most probable) value of  $L_{peak}$  as a function of range, the empirical equation (Eq. 5.1) with the generalised coefficients  $A_G$  and  $B_G$  is applied to the values of  $SEL$  obtained from the numerical modelling of the sound field.

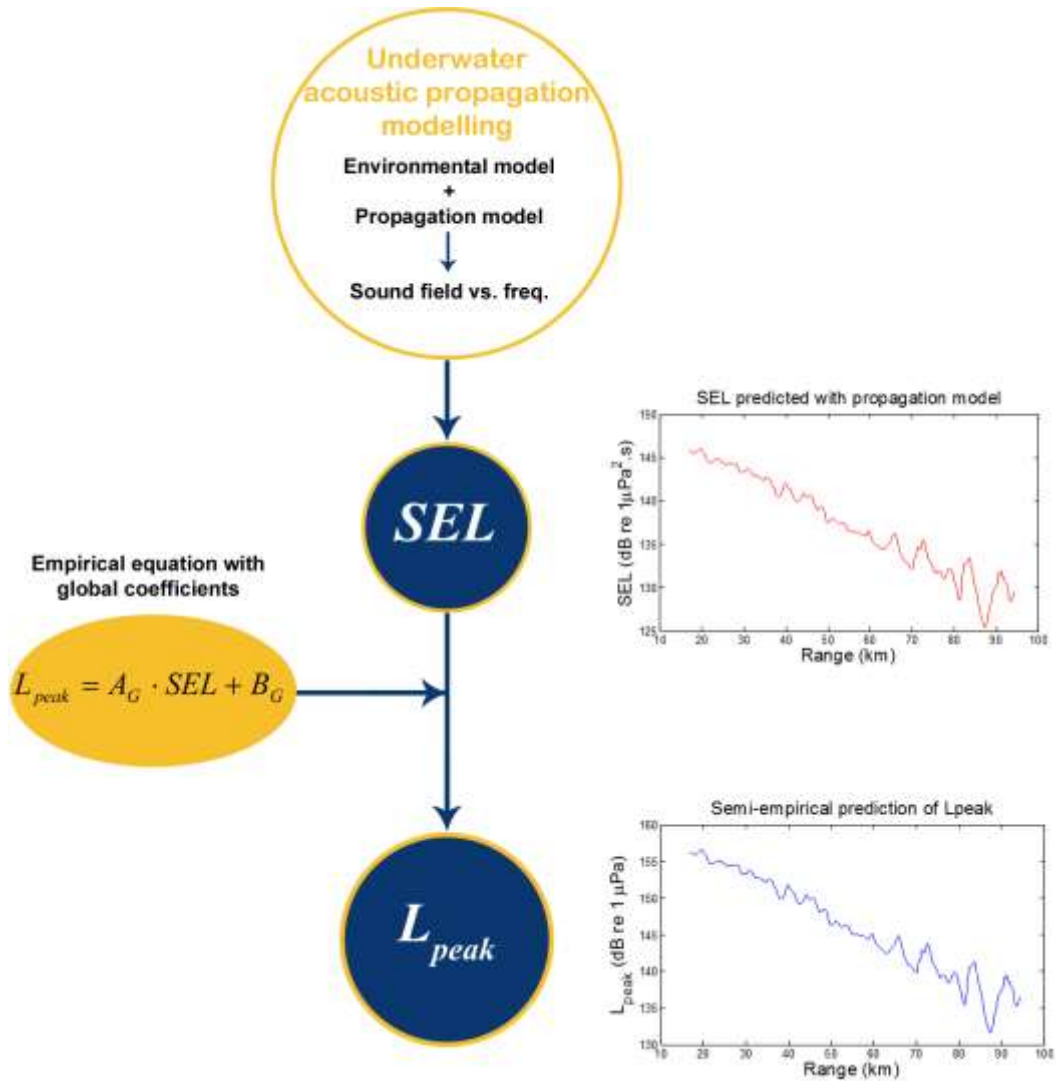


Fig. 5.30: Visualization of semi-empirical prediction algorithm.

## 5.4.2 Application of the algorithm

The following figures show the results of the semi-empirical prediction for the data measured in the Cape Leeuwin survey. The underwater acoustic model used for predicting  $SEL$  was RAMGeo since it was found to be the most accurate model for that particular scenario (see Chapter 4).

Figure 5.31 shows the measurements of  $L_{peak}$  (blue), the prediction obtained directly from the signal waveform, which was synthesised from RAMGeo modelling results for the sound field (red), and the semi-empirical prediction

obtained with the generalised empirical equation (Eq. 5.1) and the  $SEL$  numerically predicted by RAMGeo (yellow). Although the pattern of the semi-empirical prediction for the range variation of  $L_{peak}$  is somewhat different from the measurement data, this method predicts a much closer decay rate than the direct numerical prediction of the waveform. This is especially important at longer distances, where the prediction from the numerically simulated waveform differs significantly from the measurements because of the scattering and spreading effects of signals propagating along different paths. Therefore, from a modelling perspective, the method presented here to predict  $L_{peak}$  is more accurate than using directly a traditional propagation model.

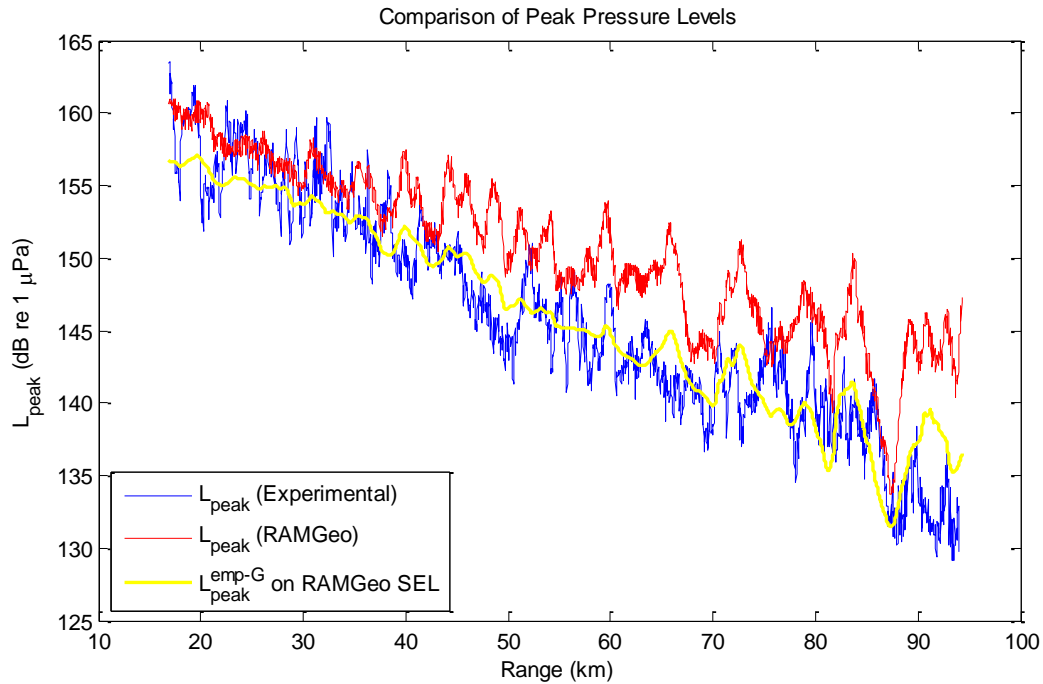


Fig. 5.31: Peak pressure level vs range. Measurements (blue); prediction obtained directly from the waveform simulated using RAMGeo (red); and semi-empirical prediction obtained using the linear equation (5.1) with the generalised coefficient and the numerically predicted  $SEL$  values (yellow).

### 5.4.3 Statistical analysis

The difference  $\Delta L_{peak}$  between the experimental and semi-empirically predicted values of  $L_{peak}$  was calculated. The histogram of the experimental data distribution of  $\Delta L_{peak}$  and PDF and CDF of the best fit by a normal distribution are shown in Fig. 5.32. The difference between the semi-empirical prediction and the measurements of  $L_{peak}$  is nearly normally distributed with the mean and standard deviation of 0.09 dB and 2.79 dB respectively.

The probability of  $L_{peak}$  to stay below a chosen threshold can be calculated, as a first approximation, using the prediction of the mean value given by Eq. 5.1 and the width  $\sigma$ . Chapter 7 presents a theoretical foundation for modelling fluctuations of  $L_{peak}$  around its mean value.

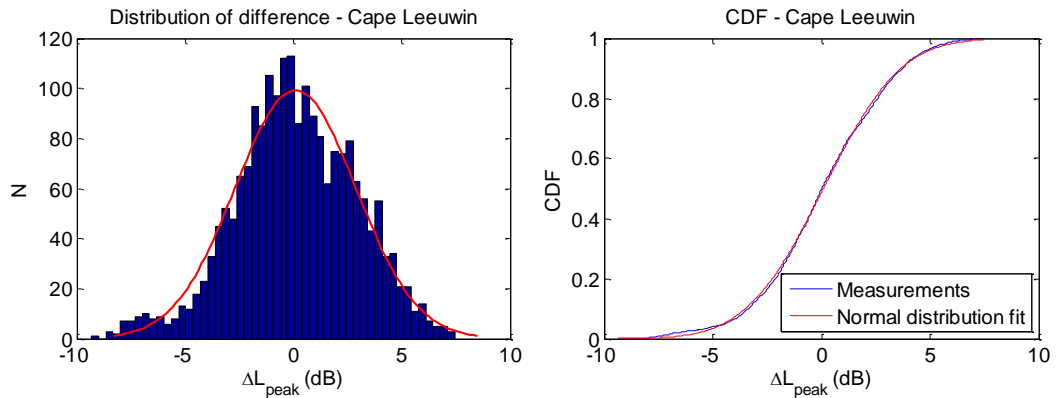


Fig. 5.32: Distribution of  $\Delta L_{peak}$ , being this the difference between the measurements and the semi-empirical prediction using the linear equation with the generalised coefficients and RAMGeo modelling results for the Cape Leeuwin data. (a) Experimental histogram and PDF (red line) of the best normal distribution fit, (b) CDF and its fit. Parameters of the normal distribution fit:  $\mu = 0.09$  dB,  $\sigma = 2.79$  dB. Parameters of K-S test:  $h = 1$ ,  $p = 0$ ,  $\alpha = 0.05$ .

## 5.5 Concluding remarks

An empirical linear equation with generalised coefficients was obtained to correlate the peak pressure level  $L_{peak}$  of airgun array signals with the  $SEL$  values measured in different marine environments at distances from about 1 km to nearly 100 km. At shorter distances the correlation between the peak pressure and sound exposure levels can be somewhat different, depending in particular on water depth. Additional testing with further measurements is required.

Variations of the difference between the predictions of  $L_{peak}$  from  $SEL$ , using the empirical equation, and the measurements follow a nearly normal distribution with the mean of about 0 dB and standard deviation of 1.64 dB.

For numerical prediction of  $L_{peak}$ , a semi-empirical method is proposed. It applies the empirical equation with generalised coefficients to the  $SEL$  values numerically predicted with a suitable underwater acoustic model. For the Cape Leeuwin environment and the PE code RAMGeo for numerical modelling, the difference with the measurements followed a nearly normal distribution of 0.09 dB mean and 2.79 dB standard deviation.  $L_{peak}$  predicted directly from the waveform modelled using RAMGeo exceeded the measured values by more than 10 dB at certain distances greater than 48 km and the difference varied from -2.5 and 14.6 dB at ranges between 70 and 94 km.

Therefore, the prediction obtained with the semi-empirical method was proved to be significantly more accurate than the result obtained by direct application of an underwater acoustic model.

## Chapter 6.

# Analysis of single airguns and airguns arrays as acoustic sources

The correlation between  $SEL$  and  $L_{peak}$  was considered in Chapter 5 for impulsive signals from different seismic surveys using airgun arrays. It was shown that the dependence of these two measures can be well approximated by linear regression with similar coefficients for all tracks and locations regardless of water depth and other environmental parameters. As a result of the generalised analysis, two regression coefficients (slope  $A_G$  and offset  $B_G$ ) were derived for predicting  $L_{peak}$  from  $SEL$ . While the values of each  $A$  and  $A_G$  being greater than 1 are a consequence of  $L_{peak}$  decreasing faster than  $SEL$  in an underwater sound channel due to multipath sound propagation and sound scattering by randomly varying environmental parameters, the offset  $B$  is expected from a general physical point of view to be governed primarily by properties of the acoustic source rather than characteristics of the environment. Further measurements of acoustic signals from different source types, received at different distances and azimuth angles, and propagated in different acoustic environments are required to confirm that statement. However, such a study is beyond the scope of this project because of time constraints and the lack of available measurements.

This chapter investigates characteristics of individual airguns and airgun arrays as an underwater sound source via modelling. No propagation effects are

considered in this chapter, and therefore no direct comparison with results obtained in other chapters is made.

Source signals were modelled using the numerical model of sound emission from single airguns and airgun arrays developed at the CMST [87] based on the bubble oscillation model [85], which was described in Section 2.2.1.3. Figures with calibration of signals are presented for airgun arrays to prove the accuracy of the model and therefore the reliability of the results obtained.

## 6.1 Single airguns

The source signal was modelled for five single airguns with standard volumes of 10, 20, 50, 150, and 350 cui. The airguns were assumed to be fired at the surrounding hydrostatic pressure at a typical depth of 7 m below the sea surface and with internal chamber pressure of 2000 psi. As an example, the modelled waveform and spectrum of the signal produced by a single airgun of 150 cui in an infinite body of water are shown in Fig. 6.1.

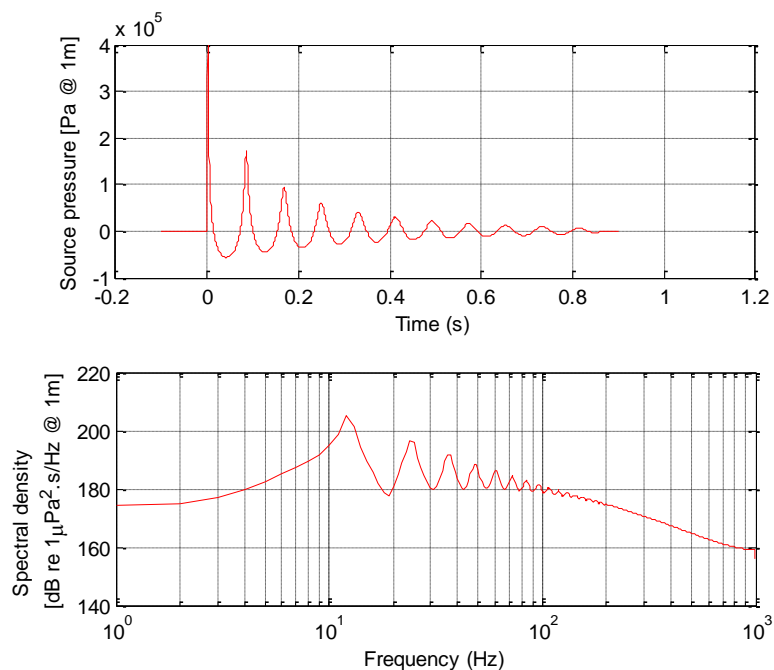


Fig. 6.1: Waveforms (top) and energy spectral level (bottom) of a signal for a single airgun of 150 cui predicted by the CMST airgun model. The signal reflected from the sea surface (ghost) is not included.

A single airgun in an infinite body of water is an omnidirectional acoustic source. In this case, the coefficient  $A$  in the linear regression equals unity ( $A = 1$ ), as changes in both  $SEL$  and  $L_{peak}$  with the distance from the source are governed only by the spherical spreading loss and there is no change to the shape of the signal as it propagates. Hence:

$$L_{peak} = SEL + B \text{ dB re } 1\mu\text{Pa} . \quad (6.1)$$

The sound energy and consequently the sound exposure increases linearly with the product of the volume and chamber pressure of an airgun [129]. This is demonstrated in Fig. 6.2 (left panel), where the sound exposure calculated from the sound signals modelled at 1 m from airguns is plotted against the airgun volume at a constant chamber pressure. In an ideal airgun, where a pressurized ideal gas is instantaneously discharged from the chamber, the peak acoustic pressure is theoretically proportional to the cube root of the airgun volume [85]. However, in more physically realistic airgun models with a finite discharge time, the peak pressure is rather proportional to the square root of the volume, as predicted by the CMST model and illustrated in Fig. 6.2 (right panel). Therefore, the square of the peak pressure is expected to have a linear dependence on volume, as the sound exposure does for a constant chamber pressure.

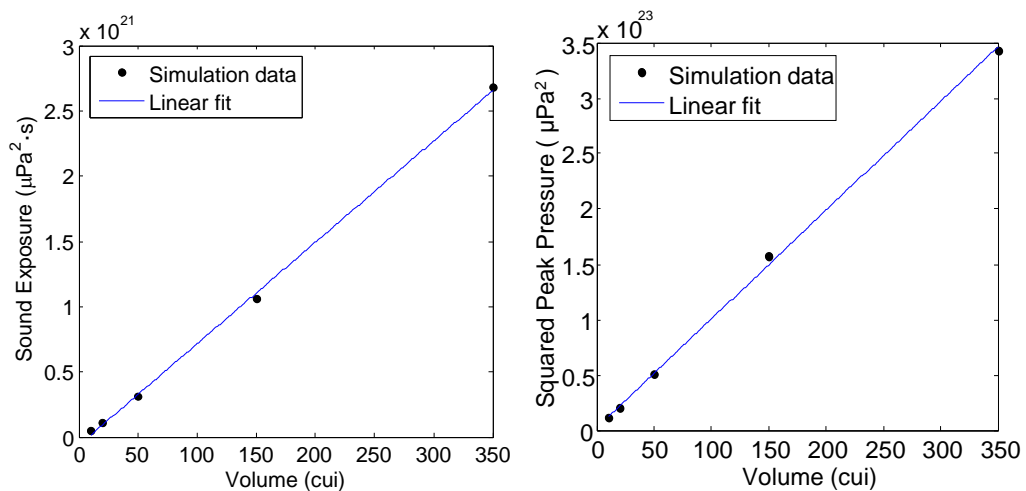


Fig. 6.2: Left: Sound exposure level vs. volume for five single airguns. Right: Squared peak pressure vs. volume for the same single airguns.

Consequently, this implies that the coefficient  $B$  for signals from single airguns is expected to be independent of airgun volume at a constant chamber pressure. Figure 6.3 shows the coefficient  $B$  estimated using Eq. 6.1 and the sound exposure and peak pressure modelled for different airgun volumes. Although there is some gradual decay in the estimated coefficient  $B$  with an increase of volume, the overall change of  $B$  is less than 3 dB over a large range of volumes from 10 to 350 cui.

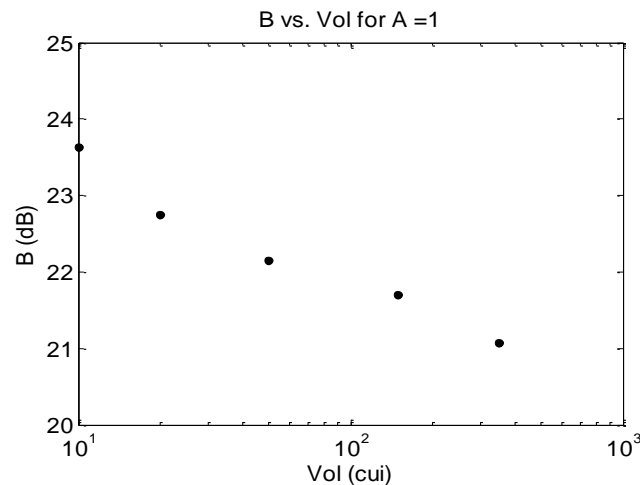


Fig. 6.3: Coefficient  $B$  vs Volume for  $A = 1$  for single airgun signals in semi-logarithmic scale.

## 6.2 Airgun arrays

### 6.2.1 Description of the arrays

A set of five arrays, either used or proposed for real seismic surveys, was used to model the sound emission. The set comprises a variety of geometries, volumes and firing depths, as shown in Table 6.1. Plan views of the arrays are given in Fig. 6.4.

The signals were modelled at a  $90^\circ$  elevation angle (horizontal direction), which is more relevant to sound propagation over long distances than the vertical direction. Unlike single guns, airgun arrays are directional sound sources, so to examine the variations of the regression coefficient  $B$  with the azimuth angle, the modelling of signals was done for azimuth angles from  $0^\circ$  to  $360^\circ$  with an increment of  $5^\circ$ . It is important to notice the following: most of the

measurements of signals from the seismic surveys used in this study and presented in Chapter 3, were done in the direction of sound propagation close to the direction of the seismic vessel track, i.e. at azimuth angles of either  $0^\circ$  or  $180^\circ$  relative to the array orientation, as shown in Fig. 6.4. This means that the azimuth angle did not have much effect on the measurements of the correlation between  $L_{peak}$  and  $SEL$ . For other azimuth angles the coefficient  $B$  is expected to be different, as the time offset between signals from individual guns is different, which affects the peak pressure to a much greater extent than the energy of emitted sound.

Table 6.1: Description of airgun arrays

Array Number	Geometry	Volume (cui)	Firing depth (m)
1	Horizontal and planar	2360	9
2	Horizontal and planar	3460	7
3	Horizontal and planar	4230	7
4	V-shaped in vertical plane	5085	6 and 9
5	Horizontal and planar	6300	10

Only for verification purposes, the signal emitted from each array at a  $0^\circ$  elevation angle (vertical downward direction) was also modelled and the ghost signal reflected from the sea surface was included in the model to make a comparison with the example waveform numerically predicted, verified and provided by the operators of the modelled airgun arrays. The signals were modelled in the far field and then the amplitude was scaled to 1 metre from an equivalent point source based on spherical spreading loss, as explained in section 2.2.1.3. The plots with a comparison of the modelled signals and those provided by the operator for each array, including the waveform and spectra, are shown in Figs. 6.5 to 6.9.

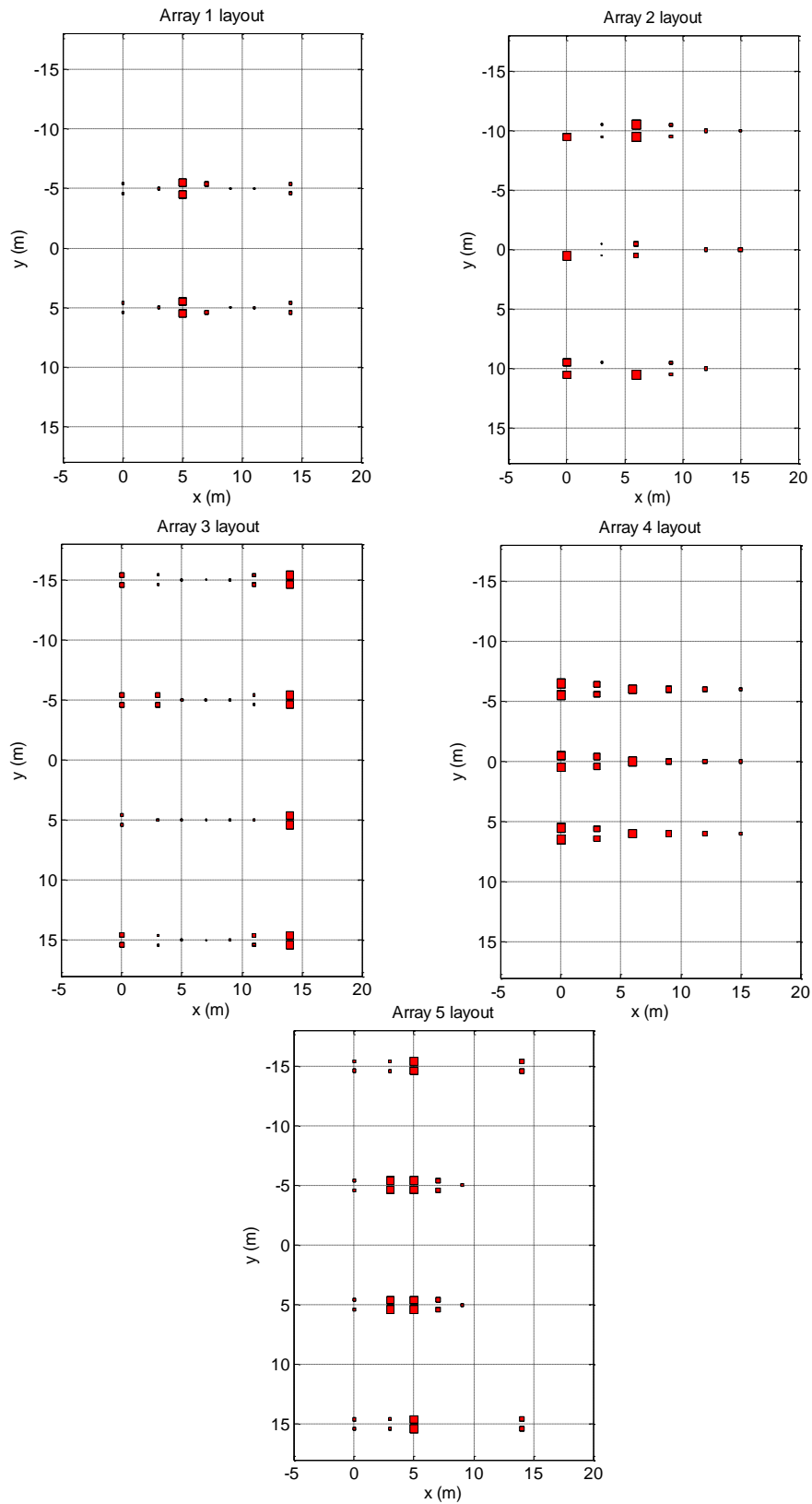


Fig. 6.4: Horizontal layout of airgun arrays. Array elements are shown much larger than actual size, comparing to the distance between the guns, but are scaled proportional to the cube root of their volume.

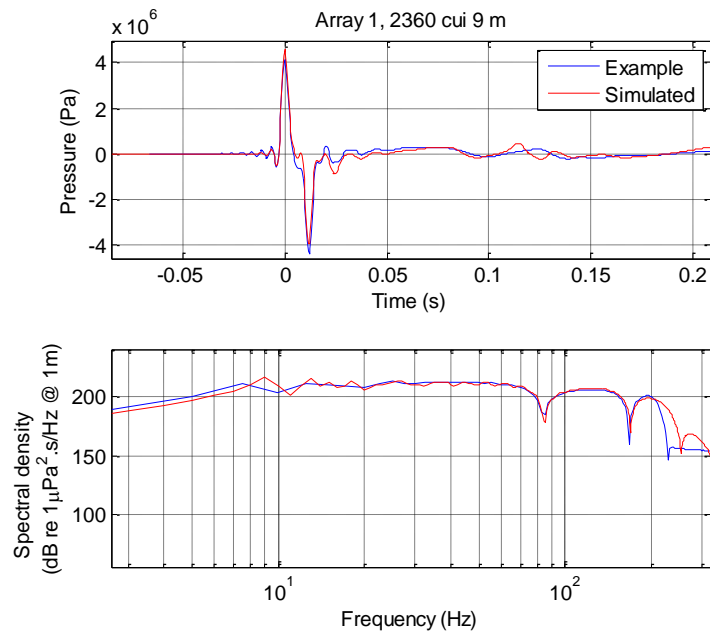


Fig. 6.5: Comparison between the waveforms (top) and energy spectral level (bottom) for Array 1 towed at 9 m below the sea surface. The example (measured) signal for the vertically downward direction (blue) and the signal predicted by the CMST's airgun array model (red).

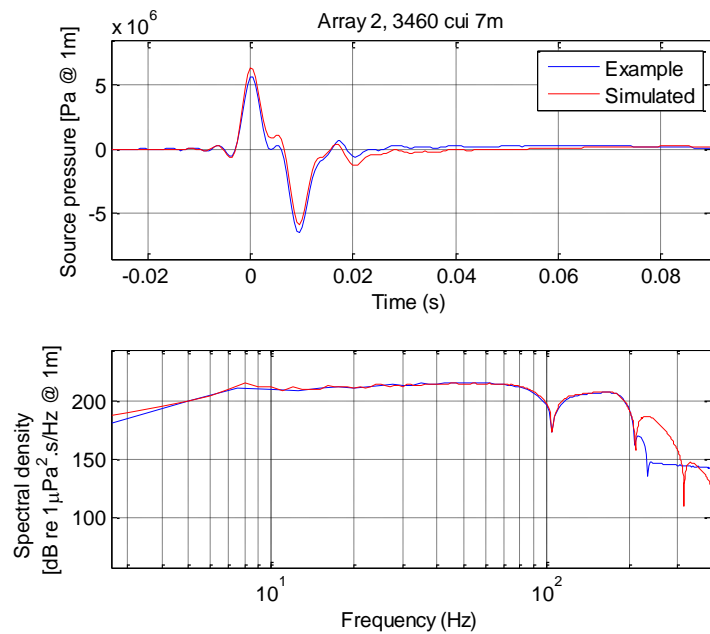


Fig. 6.6: Comparison between the waveforms (top) and energy spectral level (bottom) for Array 2 towed at 7 m below the sea surface. The example (measured) signal for the vertically downward direction (blue) and the signal predicted by the CMST's airgun array model (red).

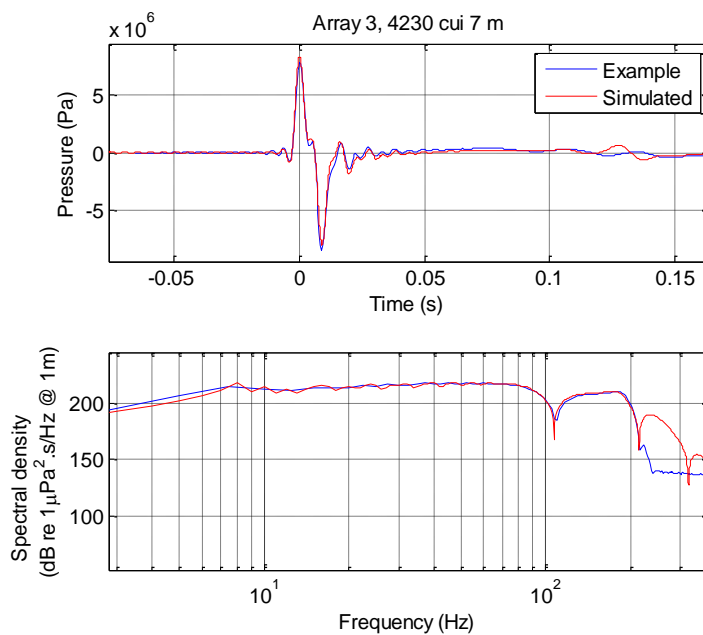


Fig. 6.7: Comparison between the waveforms (top) and energy spectral level (bottom) for Array 3 towed at 7 m below the sea surface. The example (measured) signal for the vertically downward direction (blue) and the signal predicted by the CMST's airgun array model (red).

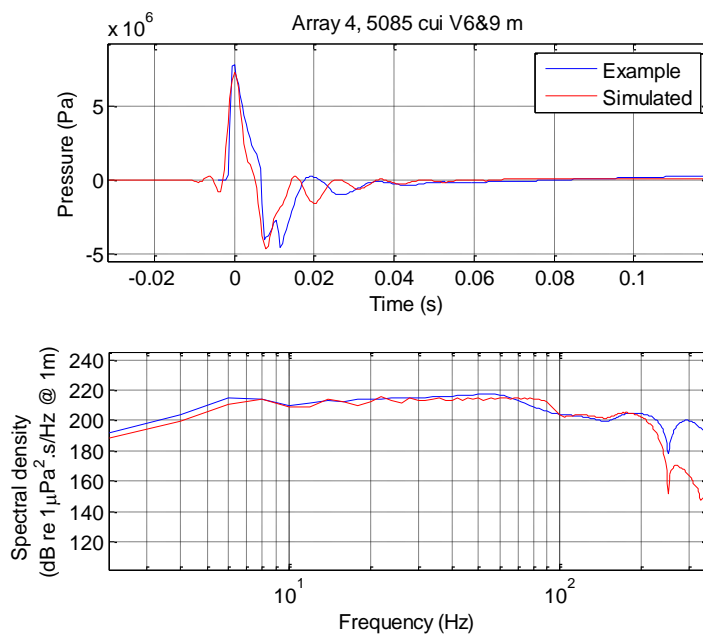


Fig. 6.8: Comparison between the waveforms (top) and energy spectral level (bottom) for Array 4 towed at 6 and 9 m (V-shaped) below the sea surface. The example (measured) signal for the vertically downward direction (blue) and the signal predicted by the CMST's airgun array model (red).

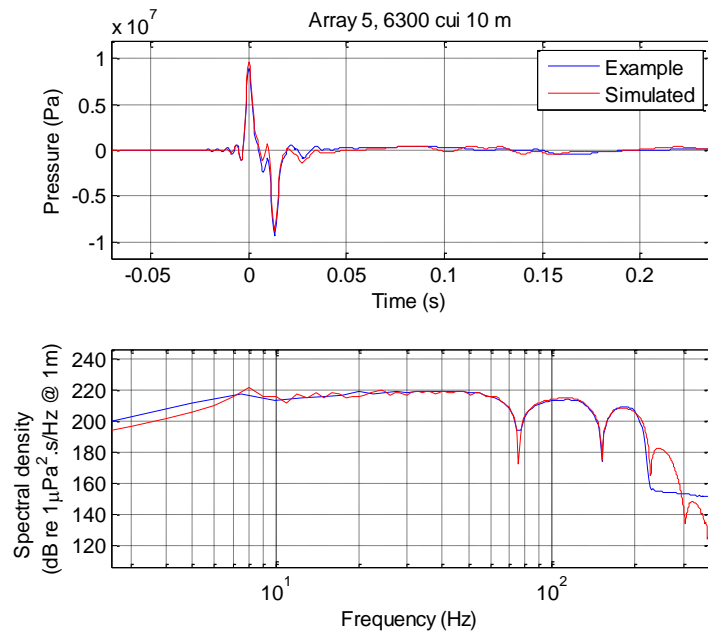


Fig. 6.9: Comparison between the waveforms (top) and energy spectral level (bottom) for Array 5 towed at 10 m below the sea surface. The example (measured) signal for the vertically downward direction (blue) and the signal predicted by the CMST's airgun array model (red).

## 6.2.2 Correlation between peak pressure level and sound exposure level for different azimuth angles

The coefficient  $B$  in the correlation between  $L_{peak}$  and  $SEL$  of a sound signal emitted by an airgun array is expected to be dependent on azimuth angle as a result of the array directionality. This is expected for signals propagating in an ocean channel, but also at the source. The lack of measurements over a range of azimuth angles limits the analysis of the azimuth dependence of regression coefficients in real underwater sound channels; however, this can be analysed for the modelled signals emitted by airgun arrays, which are presented in this chapter. The effects of surface or seabed reflections were excluded.

Figure 6.10 shows the coefficient  $B$  as a function of volume for  $A = 1$ , for an elevation angle of 90 degrees and azimuth angle 0, 45 and 90 degrees. One can see that the  $B$  coefficient appears to have a weak volume dependence in the interval from 2300 to 3600 cui, which depends on azimuth. This result is similar to what was obtained for single airguns.

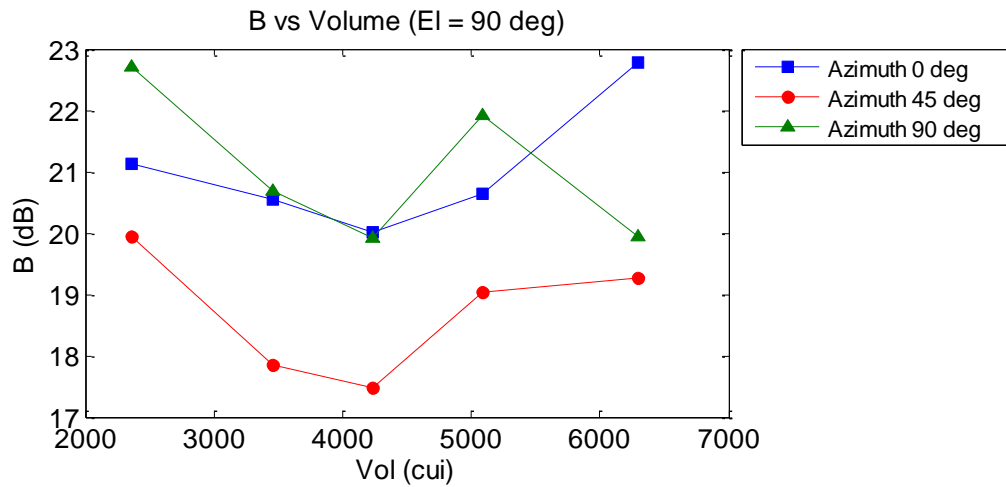


Fig. 6.10: Coefficient B vs Volume for A = 1 for airgun array signals.

The difference in the variations of  $L_{peak}$  and  $SEL$  with azimuth angle  $\theta$  is illustrated in Fig. 6.11 representing polar diagrams of  $SEL$  and  $L_{peak}$  for all five arrays from Table 6.1. It is clear from these diagrams that  $L_{peak}$  is much more dependent on azimuth angle than  $SEL$ , which varies slowly with  $\theta$ . For all arrays, the primary maxima occur at  $0^\circ$  and  $180^\circ$ , and the secondary maxima at  $90^\circ$  and  $270^\circ$  or viceversa. At these directions in the far field, the signals are emitted in phase from individual linear sections (sub-arrays) of a rectangular planar array and consequently produce higher peak pressure levels, whereas the signal energy (and hence  $SEL$ ) of a superposition of signals from individual guns is much less sensitive to signal phase.

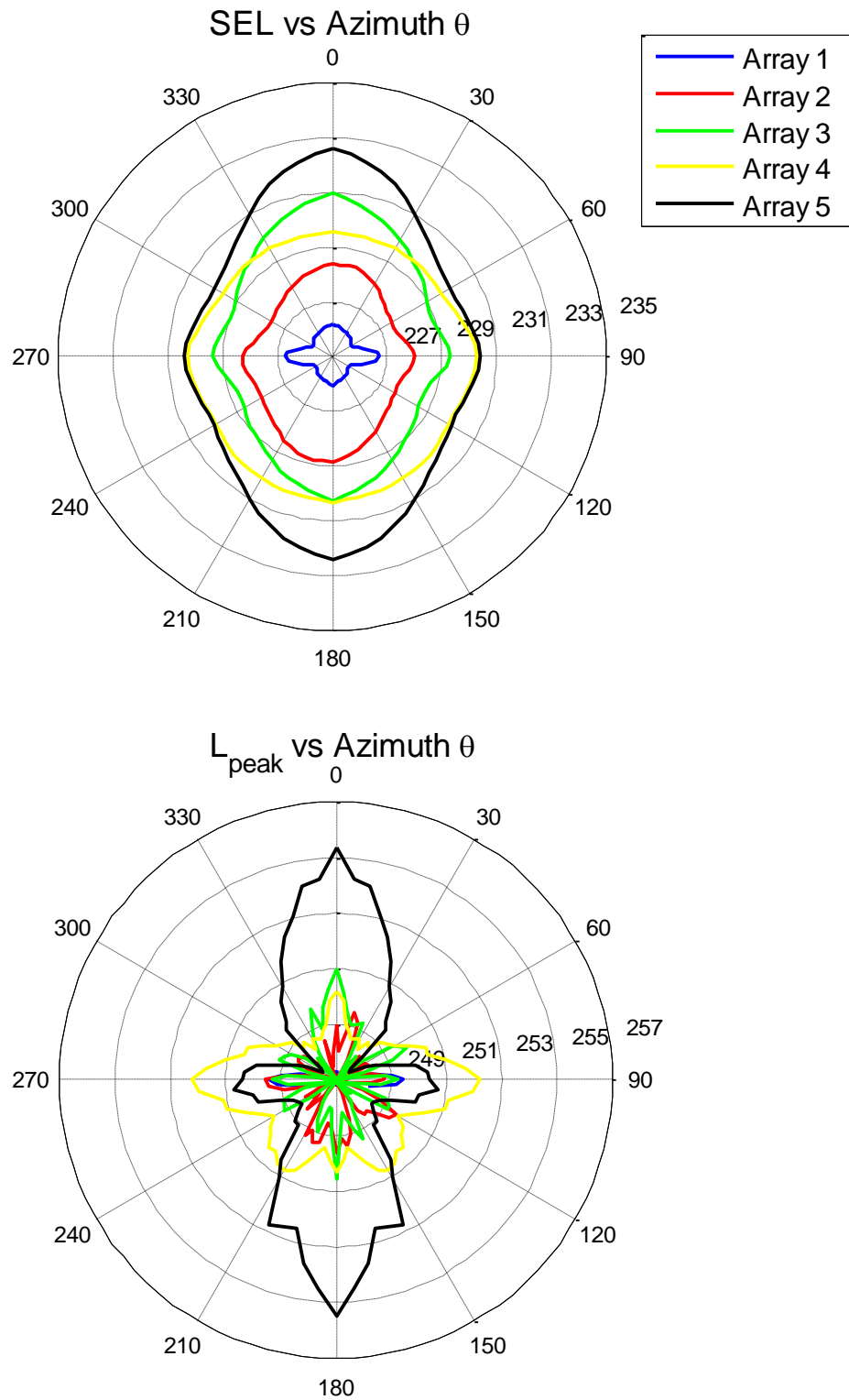


Fig. 6.11: Variation of  $SEL$  in dB re 1  $\mu\text{Pa}^2\cdot\text{s}$  (top blue) and  $L_{\text{peak}}$  in dB re 1  $\mu\text{Pa}$  (bottom red) vs azimuth angle in degrees, calculated for source signals modelled for Array 5.

The linear equation Eq. 6.1 to predict  $L_{peak}$  from  $SEL$  at different ranges can be corrected now for azimuth angles different from  $0^\circ$  by including a term  $\beta(\theta)$ , which is specific to each individual airgun array. This function represents the difference between the difference of  $L_{peak}$  and  $SEL$  at  $0^\circ$  and  $L_{peak}$  and  $SEL$  at the azimuth of interest (see Eq. 6.2).

$$\beta(\theta) = (L_{peak}(0) - SEL(0)) - (L_{peak}(\theta) - SEL(\theta)). \quad (6.2)$$

Then Eq. 6.1 is replaced with Eq. 6.3, which has a corrected coefficient  $B'(\theta) = B - \beta(\theta)$ , when the azimuth angle is different from  $0^\circ$ .

$$L_{peak}(\theta) = SEL(\theta) + B - \beta(\theta) = SEL(\theta) + B'(\theta). \quad (6.3)$$

As an example, the function  $B'(\theta)$  was calculated for the five arrays and it is represented in Fig. 6.12.

The application of a similar equation with the corrected coefficient  $B'(\theta)$  to predict  $L_{peak}$  at different distances from the source following the procedure explained in Chapter 5 (including the coefficient  $A$  as in Eq. 5.1) would require empirical verification with a comprehensive set of measurements at different azimuth angles. If applicable, the function  $\beta(\theta)$  could be calculated using the signals modelled for each specific array and for the azimuth angle between the seismic transect and sound propagation directions.

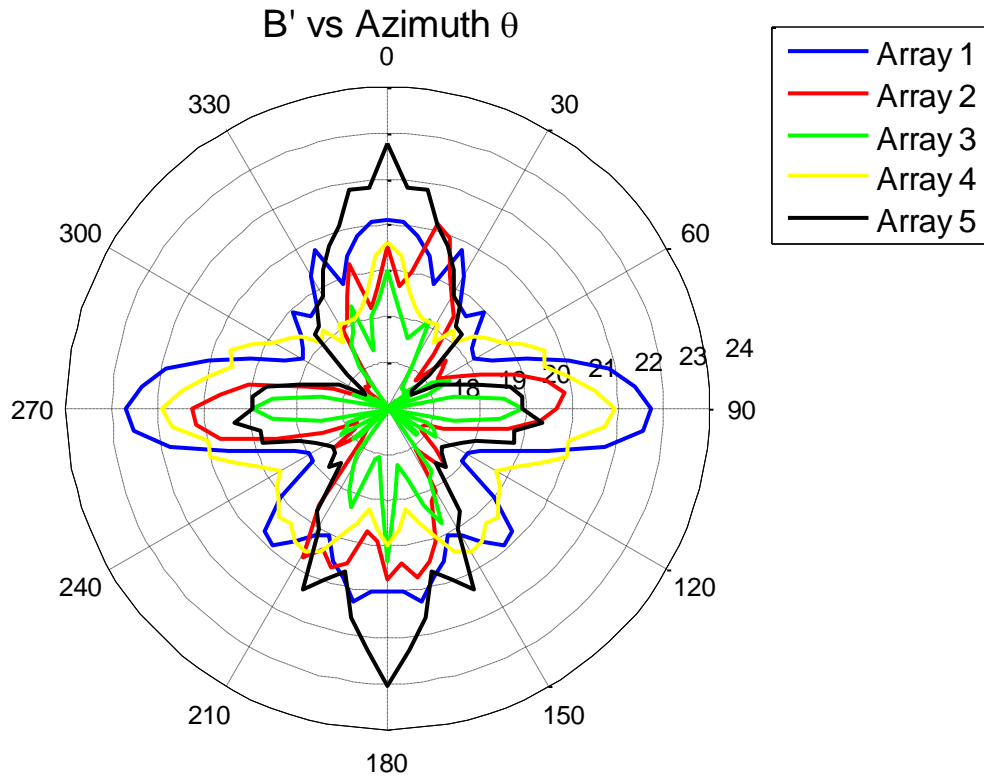


Fig. 6.12:  $B'$  vs azimuth angle in degrees, calculated for source signals modelled for Array 5.

### 6.3 Concluding remarks

The analysis of the sound signals modelled for single guns demonstrated that the sound exposure and the squared peak pressure are linearly dependent on the gun volume.

The analysis of both single guns and airgun arrays showed that the coefficient  $B$  is nearly independent of the volume of the guns or arrays.

The variation of  $L_{peak}$  with the azimuth angle was shown to be significantly larger than the variation of  $SEL$  for an array used as an example. At the directions of the maxima in the far field, the signals are emitted in phase from individual airgun lines producing higher  $L_{peak}$ , while the  $SEL$  is much less sensitive to signal phase.

A simple approximation to correct for the variation of the relation between  $L_{peak}$  and  $SEL$  of the source signal with azimuth angle was implemented by

including an additional term  $\beta(\theta)$  in Eq. 5.1 to correct the offset. The function  $\beta(\theta)$  is calculated for the azimuth of interest and it is specific of the airgun array. The approximation suggested needs to be tested using signals recorded at different azimuth angles relative to the orientation of an airgun array.

All airgun arrays in this study had the same internal pressure, and therefore no correction was needed in the generalized equation to account for it, in contrast to the analysis for pile driving noise, where an extra term is added to allow for the effect of variation in multiple piling parameters as explained in Chapter 8 and published in [130].

# Chapter 7.

## Fluctuations of peak pressure around the mean value

“Absolute calm is not the law of ocean.  
And it is the same with the ocean of life”

- Mahatma Gandhi

**I**t was demonstrated in Chapter 5 that the method based on linear regression is capable of predicting the peak pressure level  $L_{peak}$  from the sound exposure level  $SEL$ , either measured or modelled, within the standard error of less than 3 dB over ranges up to 90 km. The main cause of the prediction errors is that the peak pressure is much more affected by interference effects in randomly varying multipath acoustic channels than the sound energy governing  $SEL$ .

This chapter presents an algorithm based on Eq. 5.1 and Extreme Value Theory (EVT) to model the distribution of fluctuations of  $L_{peak}$  around its mean value and predict the probability of  $L_{peak}$  staying below a certain threshold.

### 7.1 Randomness of the peak pressure

Random events are those where a lack of pattern or law is exhibited and thus they cannot be deterministically predicted. However, when multiple random events occur, it can be possible to make statistical predictions to quantify a stochastic process by using probability theory.

Randomness can result from uncertainties of different nature. When there is not enough information about the system to offer an accurate prediction of the metrics of interest, then the randomness is known as epistemic [131].

Underwater acoustic propagation models require accurate input variables such as the sound speed profile and geoacoustic properties of the bottom to produce accurate results. The bathymetry is also crucial for that goal. Some examples of bathymetry data sets are the *Australian Bathymetry and Topography Grid, June 2009* [132] or the *New Zealand Bathymetry Grid 2008 - NIWA* [133]. Both bathymetry data sets have a spatial resolution of 250 m. Finer grids can be obtained in limited areas with advanced multibeam technology, but a fully detailed description of the seafloor cannot be accessible, particularly the exact roughness of the seafloor. Moreover, since the ocean environment is highly dynamic due to currents, tides, internal waves, etc., the effects of the seafloor roughness on sound propagation vary in time in a random manner. Thus, there will be an epistemic uncertainty in the characteristics where their values depend on the exact distribution of such irregularities.

Scattering is a phenomenon produced with incidence of sound waves on a rough surface, such as the seabed and sea surface, or by volume inhomogeneities in the sound propagation medium. Therefore, the signal reflected after the incidence on a scattering object will be subject to an epistemic randomness because the roughness is not fully known and, furthermore, it changes with time at the sea surface with wind waves and swell and in the water column due to internal waves and eddies. At shorter distances, fewer signal arrivals are interacting with scattering objects, and thus, the prediction of the peak value (and also the energy) with a deterministic model can give a good approximation. At longer distances, the interaction of signals propagating along multiple paths can be modelled as a stochastic process, where the energy can be estimated with enough accuracy, but not the peak pressure, which is more affected by the interferences of signal arrivals along different paths with different phases. Therefore, a statistical model is required to predict fluctuations of the peak pressure.

## 7.2 Theoretical foundation

The sound pressure of a signal propagated in an underwater sound channel is affected by both coherent transmission losses and incoherent fluctuations. The coherent transmission losses depend primarily on range from the sound source through energy spreading losses and on sound speed and attenuation in the bottom and water column. The incoherent fluctuations result from interference effects of multipath propagation in the underwater sound channel, which change due to varying diffraction, refraction and scattering effects.

Let us assume a sound source emitting  $N$  repeated coherent broadband signals which are received at a fixed position far enough from the source so that the sound field at the receiver can be considered fully randomized, as discussed in section 2.1. The received signal consists of multiple arrivals along different paths, with significant overlap in time. The resulting received signal can then be considered to be a superposition of different arrivals incoherent with respect to each other in a randomized sound field. Consequently, the amplitude of the received waveform will fluctuate in a saturated regime.

To isolate fluctuations in the peak pressure due to randomly varying interference, peak pressure values measured at different distances from the source should be corrected for the energy loss. This can be done using the linear regression between  $L_{peak}$  and  $SEL$  (Eq. 5.1) derived in Chapter 5. This equation can be rewritten using the definitions of the two measures in the following form:

$$10 \cdot \log \left\{ \frac{\left[ \max |p(r,t)|^2 \right]_{LR}}{\left[ \int_0^T p(r,t)^2 dt \right]^A} \right\} = B, \quad (7.1)$$

where  $T$  is the integration time used to calculate the sound exposure of a transient signal and  $\left[ \max |p(r,t)|^2 \right]_{LR}$  is the peak pressure predicted by the empirical Eq. 5.1,  $A$  and  $B$  are the slope and offset of the linear regression

respectively, and  $LR$  stands for linear regression. Let us introduce a new variable  $y$  using Eq. 7.1:

$$y \equiv \frac{(\max |p(r,t)|^2) \cdot 1s}{\left( \int_0^T p(r)^2 dt \right)^A}, \quad (7.2)$$

where  $p(r,t)$  is the measured pressure waveform. The mean value of variable  $y$  equals  $\bar{y} = 10^{B/10}$  at the predicted value  $\left[ \max |p(r,t)|^2 \right]_{LR}$ . Fluctuations of  $y$  around its predicted value are independent of the sound energy loss.

Then let us assume that the signals received from an impulsive source (1) consist of many arrivals along different rays (or arriving with different normal modes), (2) their amplitudes and phases fluctuate independently due to different scattering effects along different paths, and (3) the scattered incoherent component is large in comparison with the coherent component. In this case, the instantaneous sound pressure  $p(r,t^*)$  at an instant  $t^*$  will tend to be normally distributed [64], its magnitude  $|p(r,t^*)|$  will tend to be Rayleigh distributed, and the squared sound pressure  $|p(r,t^*)|^2$  will tend to be exponentially distributed, as discussed in Chapter 2. If the maximum value of  $|p(r,t^*)|^2$  is picked out of each received signal, where each  $|p(r,t^*)|^2$  is exponentially distributed with similar mean value, then the distribution of the new data set of the peak values will tend to an extreme value distribution [134] (see [135-137] for a detailed explanation of EVT). This distribution is the generalized Gumbel distribution. Its CDF is given in Eq. 7.3 and PDF in Eq. 7.4 for  $x = \max |p(r,t^*)|^2$ , where  $\mu$  and  $\sigma$  are the location and scale parameters respectively. The distribution will be referred to as just the Gumbel distribution henceforth for simplicity.

$$G(x) = e^{-e^{-\left(\frac{x-\mu}{\sigma}\right)}}, \quad x \in (-\infty, \infty), \quad \sigma > 0, \quad (7.3)$$

$$g(x) = \frac{e^{-\left(\frac{x-\mu}{\sigma}\right)} e^{-e^{-\left(\frac{x-\mu}{\sigma}\right)}}}{\sigma}, \quad x \in (-\infty, \infty). \quad (7.4)$$

Note that assumptions (1) and (2) can be satisfied to a certain extent only at relatively long ranges of several water depths from the source, where the number of multipath arrivals is large ( $>10$ ), and only if the transmission losses along different paths do not differ much.

If the conditions for these assumptions are satisfied, then  $y$  is expected to be Gumbel distributed.

If  $y$  is Gumbel distributed, then the upper limit  $y|_p$  for  $y$  to be below it with probability  $P$  ( $0 < P < 1$ ) can be calculated based on estimates of the location  $\mu$  and scale  $\sigma$  of the Gumbel distribution using the quantile function:

$$y|_p = -\ln[-\ln(P)]\sigma + \mu. \quad (7.5)$$

Once the limit  $y|_p$  is calculated for given  $P$  using Eq. 7.4, the limit of  $L_{peak}$  for the same value of  $P$  can be defined from the Eq. 7.5 [134].

$$L_{peak}|_p = 10\log(y|_p) + A \cdot SEL. \quad (7.6)$$

It is important to notice that for a number  $M$  of statistically independent complex variables  $\sigma = \langle |p|^2 \rangle$  and  $\mu/\sigma = \ln(\hat{M})$ , where  $\langle |p|^2 \rangle$  is the mean value of  $|p(r,t)|^2$ . Here  $\hat{M} = 2M \approx 2\gamma$  as  $p$  is a complex variable with two independent components. This means that the parameters  $\mu$  and  $\sigma$  can be estimated from  $\langle |p(r,t)|^2 \rangle$  and the time-bandwidth product,  $\gamma$  of the signal. The ratio of the standard deviation of  $\max|p(r,t)|$  to the mean value  $\langle \max|p(r,t)|^2 \rangle$  is:

$$R_I = \frac{\sqrt{\langle \max |p(r,t)|^2 - \langle \max |p(r,t)|^2 \rangle \rangle^2}}{\langle \max |p(r,t)|^2 \rangle} = \frac{\sigma\pi/\sqrt{6}}{\mu + \eta\sigma} = \frac{\pi}{\sqrt{6}[\ln(\hat{M}) + \eta]} \quad (7.7)$$

where  $\eta \approx 0.577$  is the Euler–Mascheroni constant [134]. Equation 7.6 shows that relative fluctuations of  $\max |p(r,t)|^2$  are approximately inversely proportional to  $\ln(\hat{M})$  at  $\hat{M} \gg 1$ .

Using the parameters defined below one can see that the sound exposure also fluctuates in the sound pressure field and its fluctuations are subject to a Gamma distribution [67]. The scale parameter of the Gamma distribution is  $\alpha = \langle |p(r,t)|^2 \rangle / \beta$ , where  $\beta \approx \hat{M}$  is the shape parameter [67]. Consequently, the standard deviation of the sound exposure is  $\langle |p(r,t)|^2 \rangle / \sqrt{\beta} \approx \langle |p(r,t)|^2 \rangle / \sqrt{\hat{M}}$ , the mean value is  $\langle |p(r,t)|^2 \rangle$  and their ratio  $R_{CE} \approx 1/\sqrt{\hat{M}}$ . By comparing  $R_{CE}$  with  $R_I$  in Eq. 7.7, one can see that relative fluctuations of the sound exposure in a fully randomized sound field decrease significantly faster with increasing time-bandwidth product than the relative peak pressure fluctuations [134].

Quite often measurements of acoustic signals in the ocean, such as signals from airgun arrays, are recorded at different distances. Then it becomes not possible to measure the average sound exposure at a particular range. In this case the averaging could be achieved via a sliding spatial window of an appropriate length such that a number of samples at different ranges are taken for averaging. However, broadband impulsive signals, such as those from airgun signals and impact pile driving, have a large time-bandwidth product (typically  $> 1000$  at ranges of several water depths) such that the fluctuations of the average intensity (or energy) due to the sound field randomization are small compared to those of the instantaneous intensity. Therefore samples of the sound exposure at each distance can be used in Eq. 7.2 for correction.

If measurements are made with a stationary complex Gaussian random signal, then the sound exposure is  $E = \langle |p(r,t)|^2 \rangle T$ , where  $T$  is the integration time, and hence the scale parameter of the Gumbel distribution of the ratio  $y$  will be  $\sigma = \langle |p(r,t)|^2 \rangle^{1-A} T^{-A}$  and the location parameter  $\mu = \sigma \ln(\hat{M})$  [134].

In the following subsections this approach to model fluctuations of  $L_{peak}$  and predict the maximum levels of certain probability is examined using the combined data set and the single data set from the Cape Leeuwin seismic survey.

### 7.3 Analysis of the combined data set

The generalised regression coefficients  $A_G = 1.213$ , and  $B_G = -20.1$  dB re 1  $\mu$ Pa derived in Chapter 5 were used for this analysis. The ratio  $y$  was calculated for the combined data set with measurements at different ranges using Eq. 7.2 and the coefficient  $A_G$ . The fluctuations of  $y$  around the predicted value  $\bar{y} = 10^{B_G/10}$  are shown in Fig. 7.1 for all measurements. Then, the distribution of  $y$  was fitted with a Gumbel distribution using the maximum likelihood method (Fig. 7.2). The agreement between the experimental distribution and the Gumbel model fit is fairly good. The Gumbel distribution parameters obtained from the best fit will be referred to as the generalised location parameter  $\mu_G$  and the generalised scale parameter  $\sigma_G$ , with values  $\mu_G = 0.00863 \pm 0.00008$  and  $\sigma_G = 0.00307 \pm 0.00006$  for a 95% confidence interval.

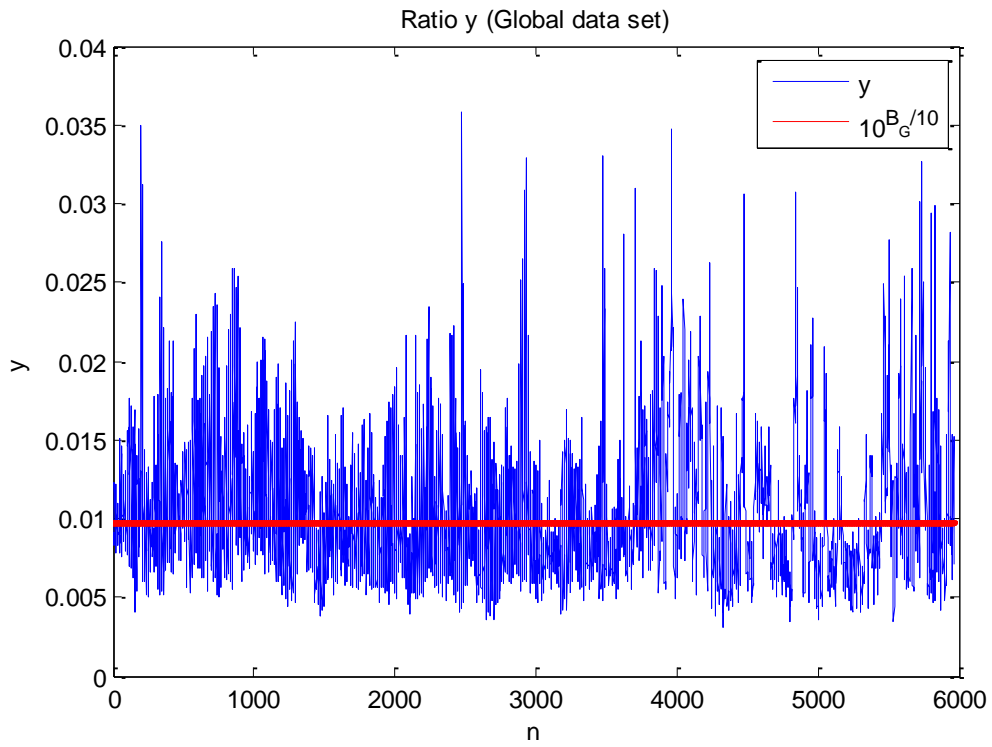


Fig. 7.1: Fluctuations of the ratio  $y$  around the constant value of  $10^{B_G/10}$  derived from Eq. 7.2 using the coefficient  $A_G$ . The number  $n$  represents the order of each individual measurement of the generalised data set at different locations.

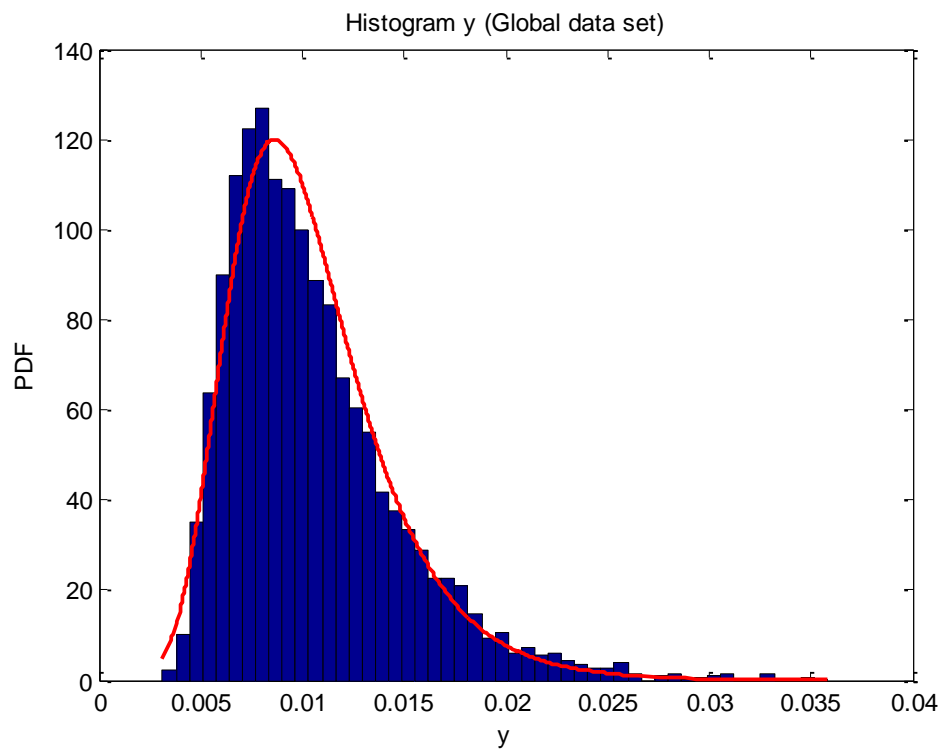


Fig. 7.2: Histogram of  $y$  and its best fit by the Gumbel distribution for the combined data set.

## 7.4 Analysis of the Cape Leeuwin data

The analysis described in the previous sections was applied to the Cape Leeuwin data set in two different ways. Firstly, the measurements of  $SEL$  and  $L_{peak}$  were analysed to assess variations of  $L_{peak}$  relative to the value predicted from the linear regression. Then, the variations of  $L_{peak}$  were modelled, using the numerical predictions of  $SEL$ , the linear regression (Eq. 5.1) and the Gumbel distribution parameters  $\mu$  and  $\sigma$ . Finally the modelled variations were compared to the measured variations.

### 7.4.1 Cape Leeuwin - Empirical analysis

Using the Cape Leeuwin data set, the ratio  $y$  defined in Eq. 7.2 was calculated with the specific regression coefficients  $A_s = 1.24$  and  $B_s = -24.0$  dB re  $1 \mu\text{Pa}$  which were derived based only on the Cape Leeuwin data set (see Chapter 5).

Figure 7.3 shows the fluctuations of the ratio  $y$  as a function of range. It can be seen that  $y$  fluctuates around the predicted value but does not gradually change with range. Then the distribution of  $y$  was fitted with a Gumbel distribution (see Fig. 7.4), which resulted in the specific location and scale parameters  $\mu_s = 0.00359 \pm 0.00006$  and  $\sigma_s = 0.00146 \pm 0.00005$  respectively for a 95% confidence interval. The agreement between the best-fit Gumbel distribution model and the experimental distribution looks worse in this case than that for the combined data set. This is supposed to take place partly because of the length of statistical sample, which is considerably smaller in the Cape Leeuwin set than that in the combined one. Also, the estimates of the location and scale parameters of the Gumbel distribution model made for the Cape Leeuwin data set are noticeably different from those made for the combined data set.

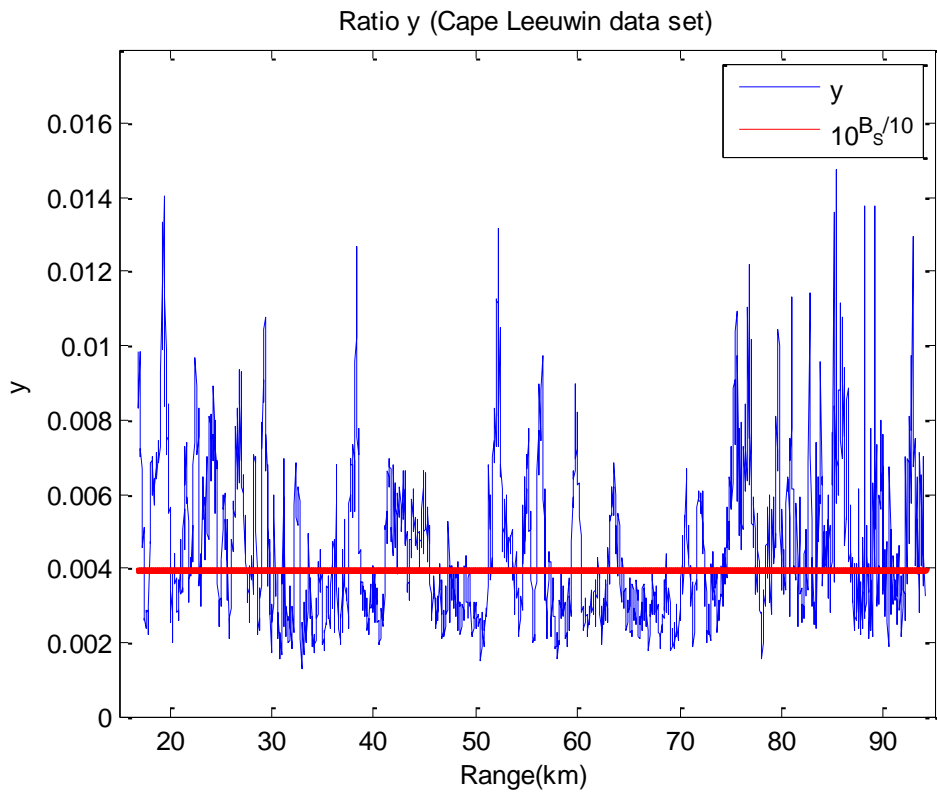


Fig. 7.3: Fluctuations of ratio  $y$  around the constant  $10^{B_s/10} u$  derived from Eq. 7.2 using the Cape Leeuwin data set and the coefficient  $A_s$ .

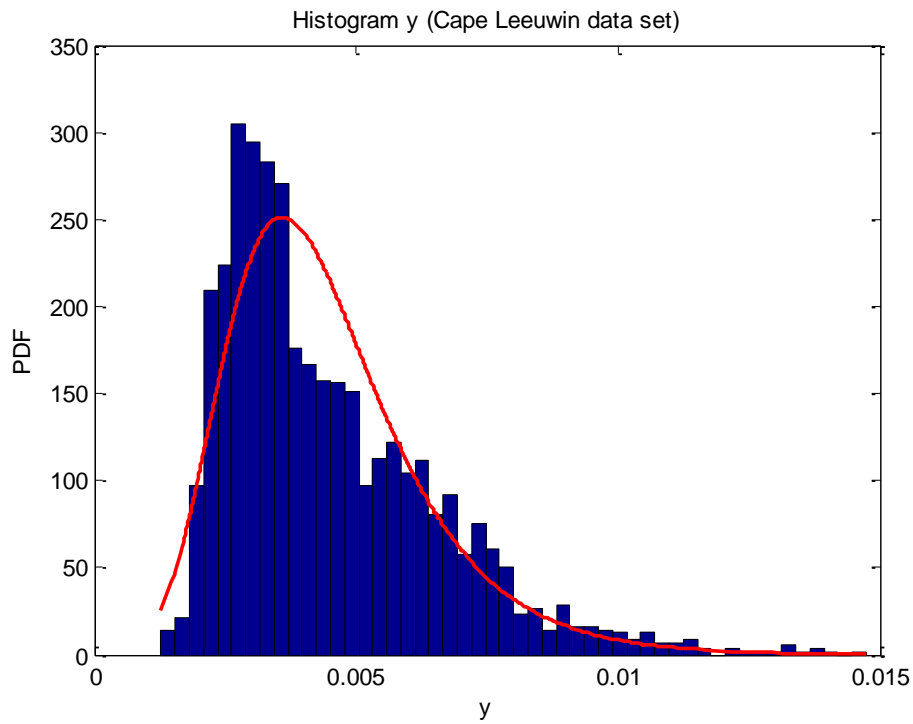


Fig. 7.4: Histogram of  $y$  and best fit to the Gumbel distribution for the Cape Leeuwin data set based on the experimental values.

Let us now consider how the difference in the regression coefficients and the estimated parameters of the Gumbel distribution model affects the probability of  $L_{peak}$  and the limit  $L_{peak}|_P$  for certain probability level  $P$ . Figure 7.5 shows the CDF of  $L_{peak}$  calculated for the low (120 dB) and high (170 dB) values of  $SEL$  observed in the combined data set. As one can see from these plots, at low  $SEL$  values (left panel) the difference in the CDFs of  $L_{peak}$  modelled using the generalised and specific regression coefficient with the Gumbel model parameters, is much smaller than 1 dB. Both CDFs predict 90% of samples to be below approximately 127 dB. At higher  $SEL$  values (right panel) the difference in the CDF models is larger; however it is still smaller than approximately 1.5 dB. For example, the CDF model based on the generalised parameters predicts that 90% of  $L_{peak}$  samples are expected to be lower than approximately 187.5 dB, while the model based on the specific parameters predicts the limit of about 189 dB with 90% probability.

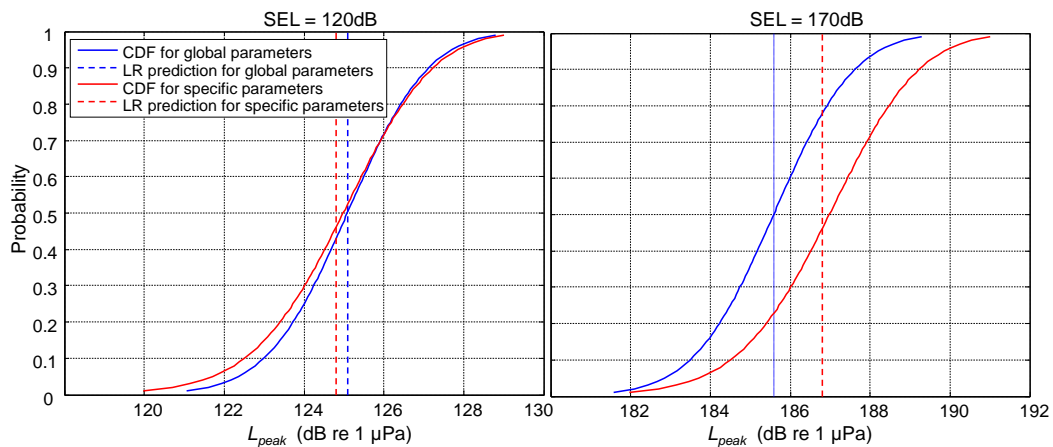


Fig. 7.5: CDF of  $L_{peak}$  calculated for two different  $SEL$  values using the regression coefficients and Gumbel distribution parameters derived from the combined data set (solid blue) and only from the Cape Leeuwin set (solid red). The dashed vertical lines show the estimation of  $L_{peak}$  using the generalised (blue) and Cape Leeuwin specific regression coefficients (red).

The comparison of the upper limits  $L_{peak}|_P$  predicted at different ranges of the Cape Leeuwin data set for probability  $P = 0.9$  using the generalised and specific parameters is shown in Fig. 7.6. This plot demonstrates clearly that the predictions made from the specific or generalised coefficients using the Gumbel model parameters give very similar results. To check this quantitatively, the number of  $L_{peak}$  values measured below both curves was calculated and then divided by the total number of measurements. The results are: 89.5% of measurements lying below the curve obtained from the specific parameters (red line) and 86.9% lying below the curve with the generalised parameters (green line). Both numbers are close to the chosen probability of 0.9, although the prediction based on the specific parameters is somewhat more accurate.

Finally, for an illustration of this empirical prediction, the upper limit  $L_{peak}|_P$  for  $P = 0.9$  calculated using the generalised parameters is shown in Fig. 7.7 in comparison with the measured values of  $L_{peak}$  and the empirical estimation of  $L_{peak}$  using Eq. 5.1.

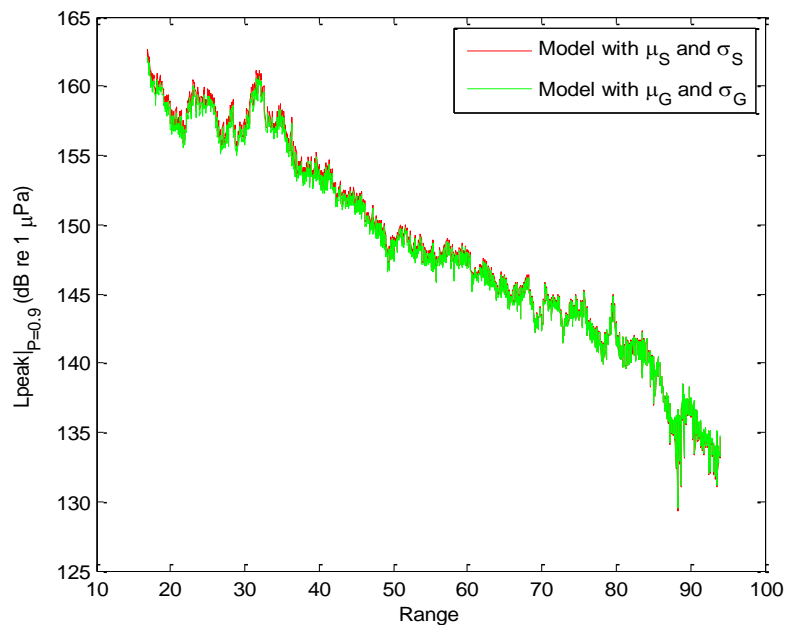


Fig. 7.6: Estimation of  $L_{peak}|_P$  for  $P = 0.9$  for the Cape Leeuwin data set using experimental *SEL* values. The red curve was obtained with the use of the specific coefficients and the green curve with the generalised coefficients.

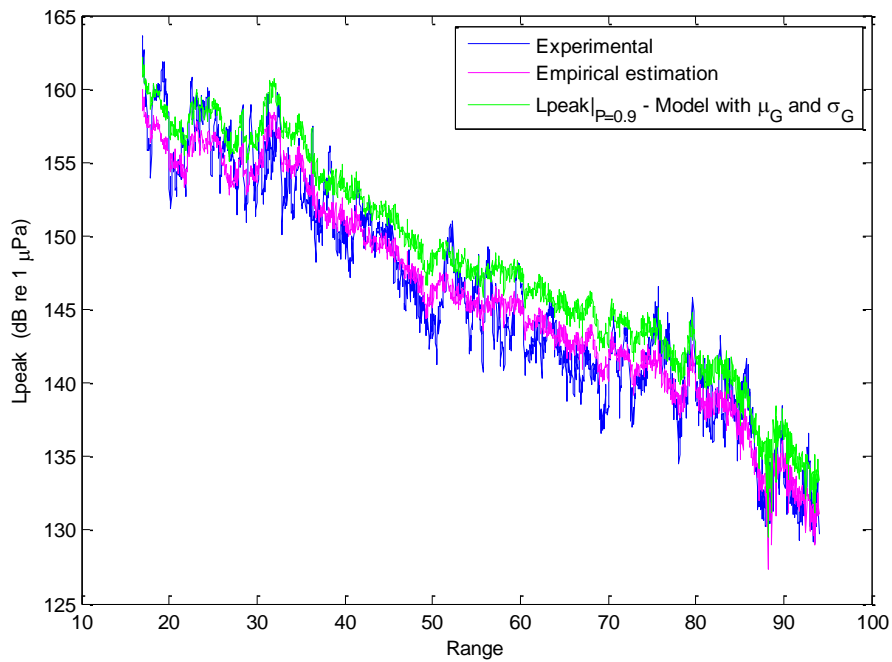


Fig. 7.7: Estimation of  $L_{peak}$  vs range for the Cape Leeuwin data set. The upper limit  $L_{peak}|_P$  estimated for probability  $P = 0.9$  using the generalised Gumbel distribution parameters (green line) is compared with experimental measurements (blue line) and the empirical estimation of the mean value using Eq. 5.1 (magenta).

## 7.4.2 Cape Leeuwin – Semi-empirical analysis

In this section the ratio  $y$  defined in Eq. 7.2 is calculated for the Cape Leeuwin data set using the values of  $SEL$  predicted with the sound propagation model RAMGeo, as described in Chapter 5.

The upper limits  $L_{peak}|_P$  predicted at different ranges for probability  $P = 0.9$  using the generalised and specific parameters are shown in Fig. 7.8. Both curves are very similar, as were those obtained from the empirical analysis in the previous section, because the same sets of the regression and Gumbel distribution parameters were used.

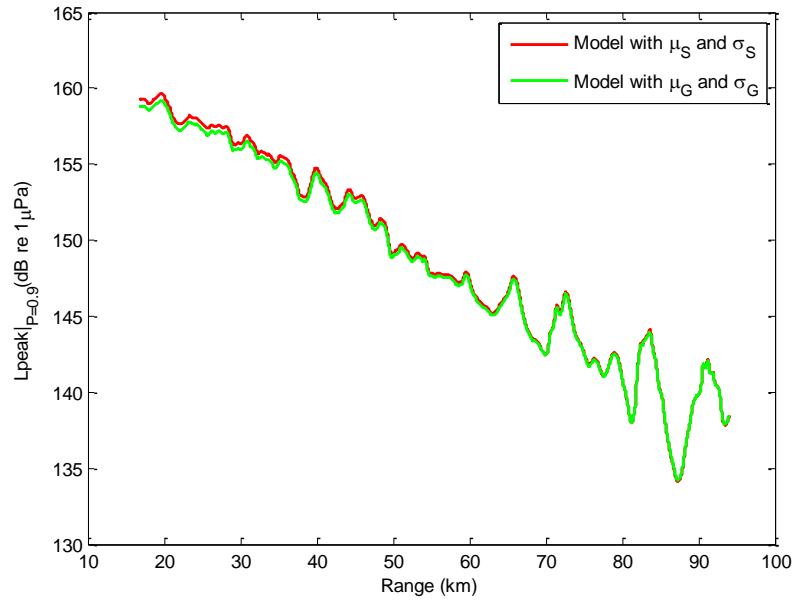


Fig. 7.8: Prediction of  $L_{peak} \Big|_P$  for  $P = 0.9$  for the Cape Leeuwin data set using the semi-empirical prediction of  $L_{peak}$  from *SEL*. The red curve was obtained with the use of the specific coefficients and the green curve with the generalised coefficients.

To assess these values, the number of actual measurements of  $L_{peak}$  below both curves was calculated and divided by the total number of measurements. The results are: 83.1% of measurements lie below the curve obtained with the specific coefficients, and 80.3% of them lie below the curve obtained with the generalised coefficients. Comparing with the modelled probability level of 90%, the results obtained have a relative error of 8% when using the specific coefficients, and 11% when using the generalised coefficients. The difference does not seem negligible; however, if the upper limit predicted with the generalised coefficients is increased by just 1 dB (which would result from small changes in the offset), then the percentage of the samples lying below the new upper limit is 89.2%. The difference between using the specific and generalised coefficients is small, and therefore the generalised coefficients can be used for different data sets to calculate  $L_{peak} \Big|_P$ .

Finally the two parts constituting the model to predict  $L_{peak}$  and its upper limit for a particular probability are represented in Fig. 7.9 for the Cape Leeuwin

data set. The measurements of  $L_{peak}$  are compared with the semi-empirical prediction (obtained in Chapter 5) and the upper limit  $L_{peak}|_P$  for  $P = 0.9$  calculated using the generalised coefficients (regression coefficient  $A_G$  obtained in Chapter 5 and Gumbel parameters  $\mu_G$  and  $\sigma_G$  obtained in this chapter). The decay predicted with the semi-empirical model (average value) is now complemented with an estimation of the upper limit of 0.9 probability as a function of range.

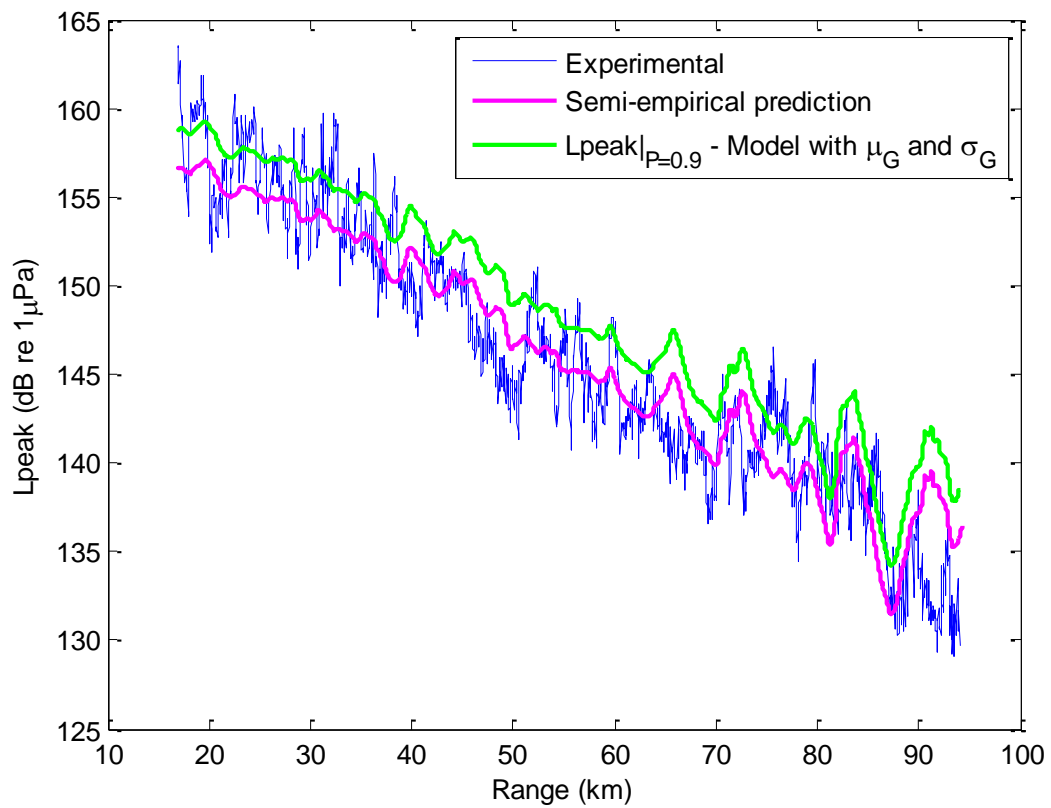


Fig. 7.9: Prediction of  $L_{peak}$  and its upper limit of 90% probability vs range for the Cape Leeuwin data set. Semi-empirical prediction of the average value of  $L_{peak}$  (magenta). The upper limit for the 90% of values (green). Experimental measurements of  $L_{peak}$  (blue).

## 7.5 Description of the algorithm

Following the analysis made in this chapter and summarising the main results, this section presents the algorithm (see Fig. 7.10) to predict the upper limit of  $L_{peak}$  fluctuations of specified probability as a function of range from an airgun array.

Before describing the algorithm, it must be noted that predictions of the peak pressure level and its variations would not be needed if (1) signals from an seismic survey were recorded at various distance from the source spanning all ranges of interest and (2) a sufficiently large number of recordings were made at each distance. In this case, the mean and fluctuations of the peak pressure with its upper limit could be obtained directly from the measurements. However, if measurements are spatially sparse and/or too few recordings are made at each particular distance, then the algorithm summarised below is applied to predict the upper limit of the fluctuations of  $L_{peak}$  as a function of range. This algorithm is also applicable if we do not have measurement data (for instance prior a seismic survey). In this case, the generalised regression coefficients and Gumbel distribution parameters derived in this study are used (hence steps 1 to 3 are omitted) and  $SEL$  is modelled for each distance of interest.

1. If the number and span of measurements are sufficient to estimate the regression coefficients with: (1) relatively small confidence intervals (e.g.  $\pm 5\%$  of estimated value at 95% probability) and (2) a high quality of fit (e.g. adjusted  $R^2$  statistics  $\geq 0.95$ ), the slope and offset obtained with the measured data are validated against the generalised coefficients  $A_G$  and  $B_G$ . The rectified (specific) coefficients are accepted for further calculations, if the difference is large.
2. The function  $y$  is calculated using recorded signals and Eq. 7.2, where  $A$  is the slope in Eq. 5.1 estimated at step 1.
3. The parameters  $\mu$  and  $\sigma$  are obtained from the best fit of a generalized Gumbel distribution to the distribution of  $y$ . The number of samples of  $y$

should be large enough to ensure relatively small confidence intervals (e.g.  $\pm 5\%$  of estimated value at 95% probability).

4. For a chosen probability  $P$  ( $0 < P < 1$ ) the upper limit  $y|_p$  is calculated using Eq. 7.5 and the parameters  $\mu$  and  $\sigma$ .
5. The *SEL* values are taken from the measurements and/or modelled using an underwater sound propagation model for ranges where measurements are not available.
6. For the probability level  $P$ , the upper limit of  $L_{peak}$  is calculated as a function of range using Eq. 7.6, measured/modelled *SEL* values vs range, and the coefficient  $A$ .

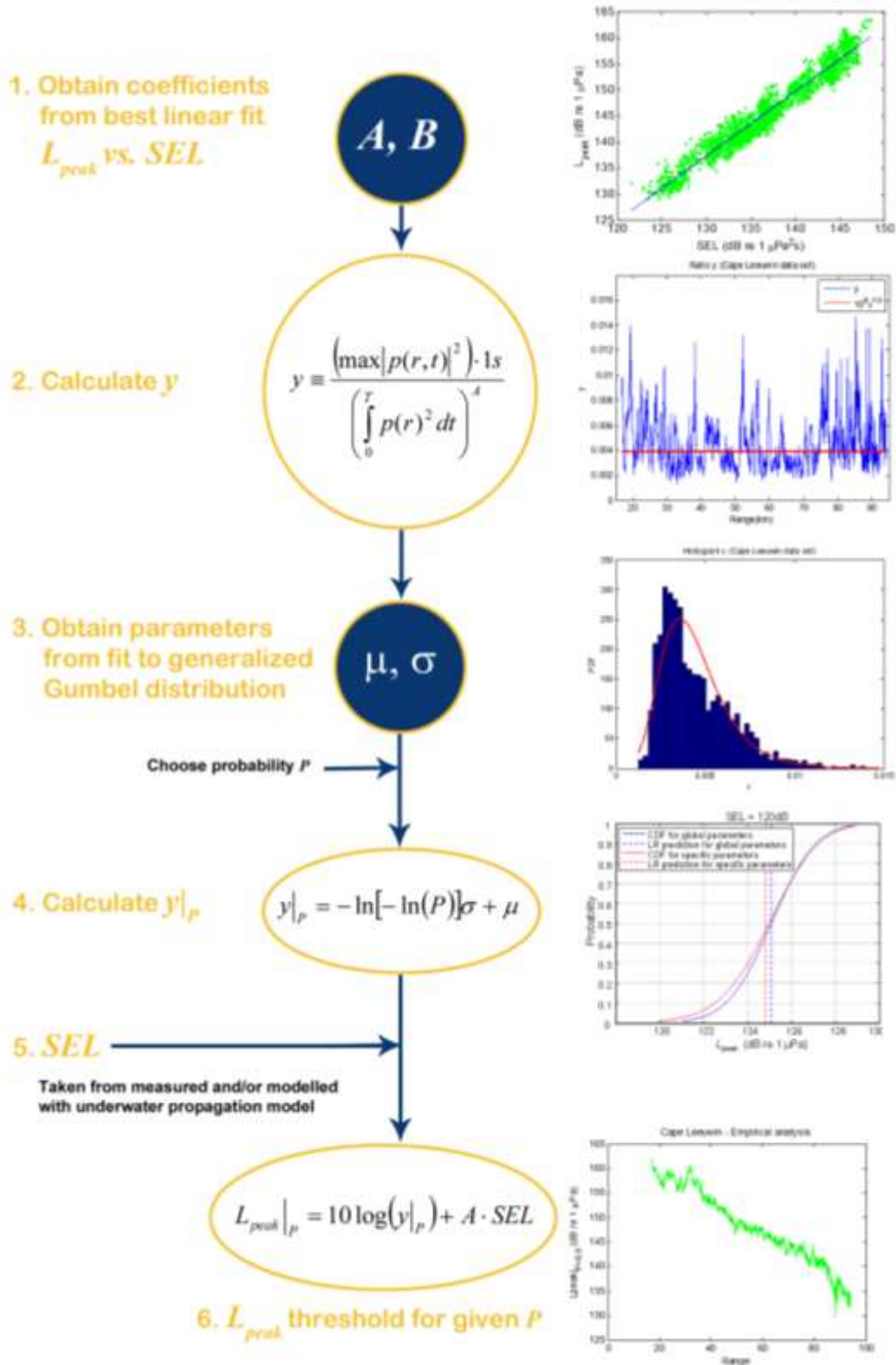


Fig. 7.10: Visualization of the algorithm to estimate the upper limit of  $L_{peak}$  fluctuations for specified probability as a function of range from an airgun array.

## 7.6 Concluding remarks

An algorithm to estimate fluctuations of  $L_{peak}$  around the mean value was presented in this chapter.

A new variable  $y$  was defined using the correlation between  $L_{peak}$  and  $SEL$  with the generalised regression coefficients derived in Chapter 5. This variable was used to quantify the fluctuations of the peak pressure around its mean value due to randomly varying interference. Extreme value theory was used to approximate the distribution of  $y$  using the properties of the peak pressure as a maximum value taken from a Rayleigh distributed amplitude. New generalised parameters  $\mu_G$  and  $\sigma_G$  were obtained from the best fit of  $y$  by a generalized Gumbel distribution, which were used to estimate the probability of  $L_{peak}$  to stay below a certain threshold.

The method was applied to the Cape Leeuwin data set to calculate the upper limit to  $L_{peak}$  for 90% of its values. Comparison with measurements showed an agreement for over 80% of values.

Therefore, the method presented offers a good approximation to estimate the threshold for a certain percentage of  $L_{peak}$  fluctuations around the mean value previously predicted with the semi-empirical model.

It is important to notice that the Gumbel distribution parameters can be derived directly from the mean intensity and time-bandwidth product only for idealised complex Gaussian random signals. However, in reality signals propagated underwater are only partly randomised to a smaller or larger extent, so that measurements of  $SEL$  and  $L_{peak}$  of signals from real sound sources are needed to estimate these parameters, which can be different for different sound source types and underwater sound transmission environments. However, the method presented in this study still can be interpreted as predictive, because offshore seismic surveys are often conducted over long time periods, so that measurements made at the beginning of operation at certain distances can then be used to predict the peak pressure level and its variations at other distances for the remaining operation.

Further theoretical and experimental analysis of the peak pressure statistics for non-fully randomized impulsive signals propagated in the ocean sound channel is needed to establish the limitations of the extreme value theory and to examine whether the parameters of the peak pressure distribution can be derived directly from measured or predicted signal characteristics, such as the bandwidth and duration.

## Chapter 8.

# Estimation of peak pressure level of signals from offshore impact pile driving operations

**C**orrelation between  $SEL$  and  $L_{peak}$  was first observed in [46] for offshore pile driving signals measured in Port Philip Bay (Victoria), as mentioned in Chapter 5, which motivated the analysis developed in this thesis and presented in the previous chapters. The linear regression coefficients obtained by the authors in [46] for  $L_{peak}$  (after conversion from the peak-to-peak pressure level  $L_{p-p}$ ) were  $A = 1.12$  and  $B = 6.3$  dB re  $1 \mu\text{Pa}$ . A new work analysing this correlation for measurements of offshore pile driving signals in the North Sea [130] was based on a similar method to the one described in this thesis for airgun array signals. This study modified the equation relating  $L_{peak}$  and  $SEL$  to account for changes in the pile parameters linked to the sharpness of the force pulse. Unlike the method for airgun array signals, where generalised coefficients were derived, the method suggested for the estimation of  $L_{peak}$  for pile driving signals is based on the use of reference values of the parameters  $A$  and  $B$  from one site to estimate the value of those parameters and  $L_{peak}$  for a new site.

This chapter analyses new data recorded in Western Australia and presents an alternative formulation to the procedure presented in [130] to estimate  $L_{peak}$

of offshore impact pile driving signals. An algorithm to estimate the fluctuations of  $L_{peak}$  around the mean value is also included.

The relevance of this study is based on the use of similar equations to estimate  $L_{peak}$  from the values of  $SEL$  for different impulsive anthropogenic signals.

## 8.1 Pile driving experimental data

The data presented in this chapter are from the measurements of pile driving noise at the Wheatstone project site, within the Ashburton North Strategic Industrial Area, located 12 kilometres west of Onslow, Western Australia. The measurements were taken as part of the noise monitoring program during the construction of the jetty and berths from November 2014 to July 2015.

Noise from 76 out of 88 steel cylindrical piles driven during the construction was recorded at a sampling frequency of 8 kHz at three different locations (see Fig. 8.1) using bottom-mounted CMST-DSTO underwater sound recorders. The distance from the driven piles varied from about 900 m to nearly 3 km

The hammer energy was within  $280 \pm 10$  kJ for most of the nearly 30,000 blows taken for the analysis, and for all blows it had a value between 200 kJ and 300 kJ.

Two different types of piles were used during the construction – vertical and slanting. All vertical piles except for two were 1016 mm in outer diameter with a wall thickness of 22 mm, whereas the slanting piles and the other two vertical piles were 1200 mm in diameter with a wall thickness of 25 mm. Slanting piles were driven at  $14^\circ$  relative to the vertical. The number of blows taken for analysis was approximately 7300 and 22600 blows for vertical and slanting piles respectively.

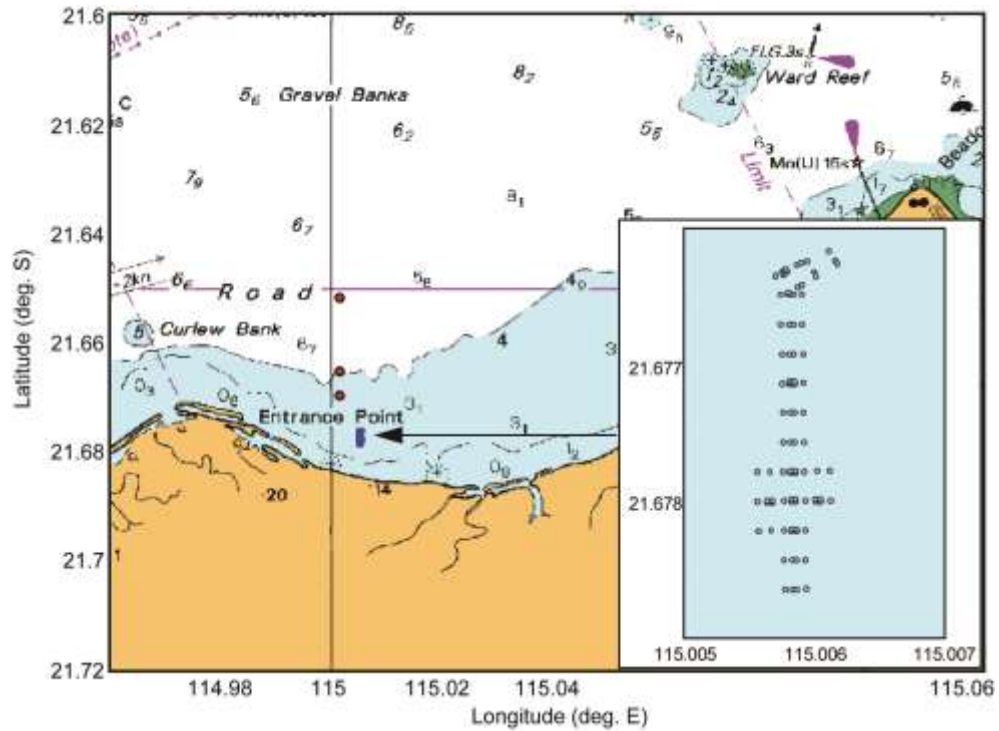


Fig. 8.1: Map of the area with location of piles (blue dots) and noise recorders (red dots). The panel on the right side shows the layout of the piles.

## 8.2 Analysis of correlation for pile driving data

Measurements of  $SEL$  and  $L_{peak}$  were plotted as a function of distance as shown in Fig. 8.2.

The correlation between  $L_{peak}$  and  $SEL$  was then analysed using all blows of the vertical and slanting piles. The measured values are shown in Fig. 8.3 with the best linear fit using Eq. 5.1. The best fit resulted in regression coefficients  $A = 1.132$  and  $B = 2.4$  dB re  $1 \mu\text{Pa}$  obtained with a root-mean-square residual of 1.4 dB and a 95% confidence interval of  $\pm 0.002$  and  $\pm 0.3$  dB for coefficients  $A$  and  $B$  respectively ( $R^2$  statistic value of about 0.975).

The distribution of the difference between the measurements of  $L_{peak}$  and the estimation obtained using Eq. 5.1, the values of  $SEL$ , and the regression coefficients obtained from all data, is represented in Fig. 8.4 with its CDF shown on the right panel. The variation of this difference follows a normal distribution, and the best fit is shown in the same plot. The standard deviation  $\sigma$  of the fit is

1.39 dB, which means that ~95% of measured  $L_{peak}$  values are within an interval of about  $\pm 2.8$  dB around the predicted result.

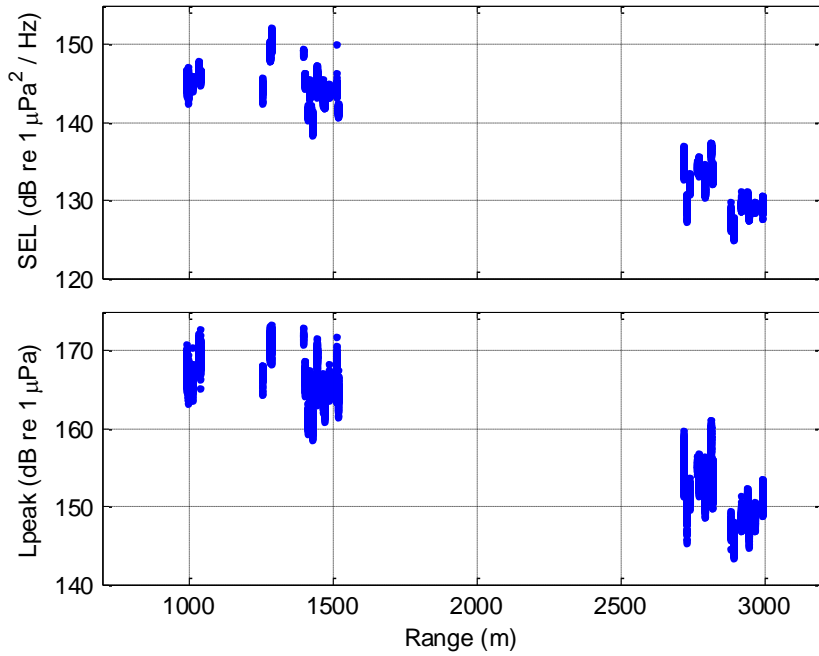


Fig. 8.2: Measurements of  $SEL$  and  $L_{peak}$  vs. range.

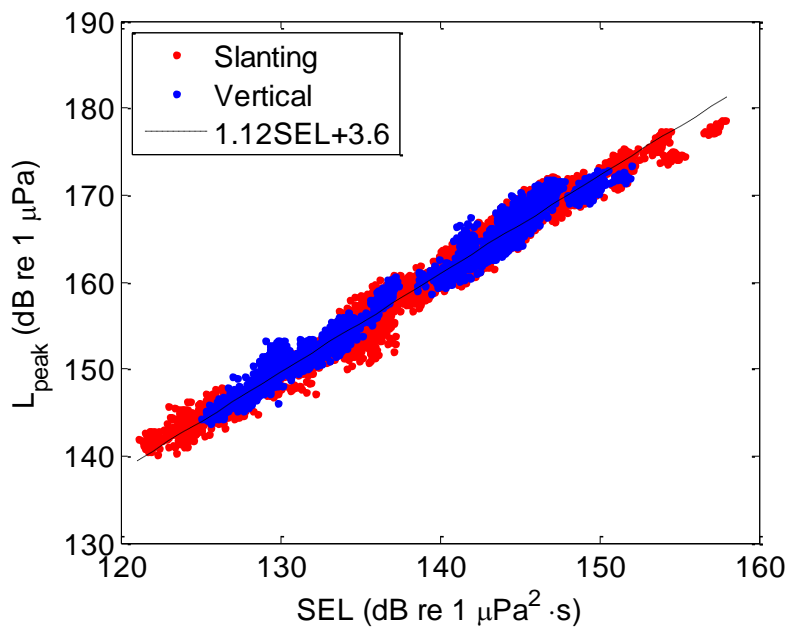


Fig. 8.3: Measurements of  $L_{peak}$  vs.  $SEL$  from vertical (blue dots) and slanting (red dots) pile. The black dashed line shows the best linear fit for the relationship derived from all samples.

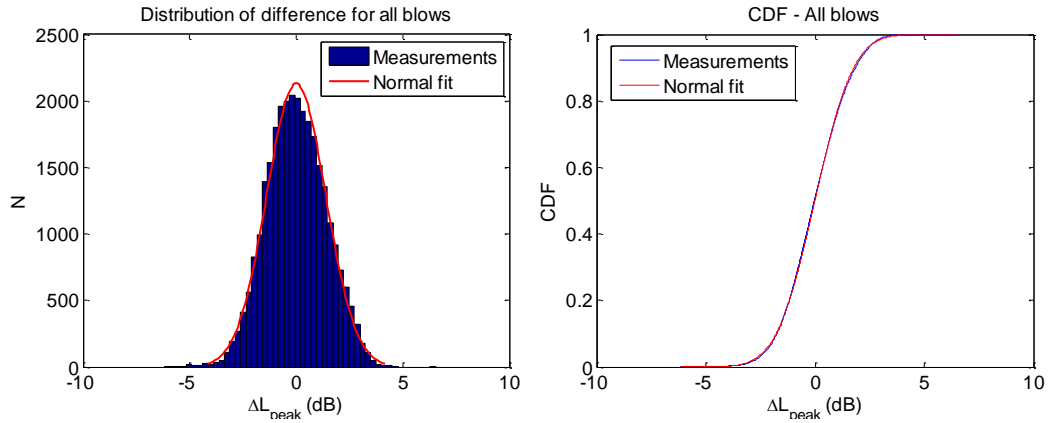


Fig. 8.4: Distribution of the difference between measured  $L_{peak}$  values and their prediction from the corresponding  $SEL$  values using Eq. 5.1 with the regression coefficients  $A = 1.13$  and  $B = 2.4$  dB (blue bars) and fit to a normal distribution (red). (a) Histogram, (b) Cumulative Density Function (CDF). Parameters of the normal fit:  $\mu = -2.3979e-013$  dB,  $\sigma = 1.3878$  dB.

The regression coefficients  $A$  and  $B$  obtained for all blows are similar to the results obtained separately for vertical and slanting piles (see Table 8.1).

Table 8.1: Regression coefficients for pile driving data

Piles	$A$	$B$ (dB)	RMS Residual (dB)
Vertical and slanting	1.13	2.4	1.4
Vertical	1.11	5.2	1.2
Slanting	1.14	1.6	1.4

When comparing now the coefficients to the results obtained in Port Phillip Bay, it can be seen that the slope  $A$  has approximately the same value, whereas the offset  $B$  is smaller in Onslow (2.4 dB vs. 6.3 dB). The results obtained previously for airgun array signals, presented in Chapter 5 and Chapter 6, suggest that the difference is most likely a consequence of the different sources parameters, i.e., different pile-hammer interaction. The comparison of the main characteristics of the piles and hammers is given in Table 8.2.

The next section suggests the corrections to be implemented in Eq. 5.1 to account for variations in pile parameters.

Table 8.2: Comparison of pile characteristics between Port Phillip Bay and Onslow

	Port Phillip Bay	Onslow (Vertical*)	Onslow (Slanting)
<b>Diameter piles (mm)</b>	710	1016	1200
<b>Wall thickness (mm)</b>	21	22	25
<b>Hammer weight (ton)</b>	4.5	13.6	13.6

\* All vertical piles except for two.

### 8.3 Correction of empirical equation for peak pressure level estimation of pile driving signals with different hammer-pile interaction

This section presents a simple model for the pile as the source of sound based on the force function. More physically comprehensive models of sound radiation from impact piles are beyond the scope of this project.

A simple hammer-pile interaction with no cushioning is assumed. The pile is represented by a damper and the hammer is represented by a mass  $m_r$ , with the velocity  $v_0$  at the impact and wall displacement  $u$  after striking the head of the pile. This model can be solved analytically [138]. The equation of motion is given by Eq. 8.1 where  $Z_p$  is the mechanical impedance of the pile, given by Eq. 8.2, for a Young's modulus  $E_p$ , pile's cross-section  $A_p$  and axial pressure wave velocity in the pile  $c_p$ .

$$m_r \ddot{u} + Z_p \dot{u} = 0, \tag{8.1}$$

$$Z_p = \frac{E_p A_p}{c_p}. \quad (8.2)$$

For the impact velocity  $v_0$  of the ram, the motion equations yield the force exerted on the pile head with the hammer (Eq. 8.3):

$$f_p = Z_p v_0 \exp\left[-\left(\frac{Z_p}{m_r}\right)t\right]. \quad (8.3)$$

The radial displacement of the pile wall and consequently acoustic pressure in the radiated sound are proportional to the force function  $f_p$ , so that the peak pressure can be expressed as:

$$P_p = K_1 Z_p v_0, \quad (8.4)$$

where the coefficient  $K_1$  allows for all effects resulting in the impact-to-sound conversion.

The energy of a sound signal or sound exposure  $E_s$  received at a certain distance from the pile is expected to be proportional to the sound energy radiated by the pile into the water column, which in turn is proportional to the impact energy  $E_r = m_r v_0^2 / 2$ , so  $E_s$  can be expressed as:

$$E_s = K_2 m_r \frac{v_0^2}{2}, \quad (8.5)$$

where the coefficient  $K_2$  allows for energy losses due to pile-ground friction, sound radiation into the seabed and spreading loss in the underwater sound channel.

Since  $L_{peak} = 20\log(Pp)$  and  $SEL = 10\log(E_s)$  Eqs. 8.4 and 8.5 can be used to calculate  $L_{peak}$  in terms of  $SEL$ :

$$L_{peak} = SEL + 10\log\left(\frac{Z_p^2}{m_r}\right) + 10\log\left(\frac{K_1}{K_2}\right) + 3. \quad (8.6)$$

Notice that the difference  $L_{peak} - SEL$  does not depend on impact energy.

Let us assume now that the regression coefficients  $A_0$  and  $B_0$  were derived from a reference data set measured for certain pile and hammer types with parameters  $Z_{p0}$  and  $m_{r0}$ . Let us also assume that changes in the piling and environmental characteristics do not significantly affect the ratio of coefficients  $K_1$  and  $K_2$ . In this case, the regression formula derived from the reference measurements can be used to estimate  $L_{peak}$  from  $SEL$  for other pile and hammer parameters using a correction term based on Eq. 8.6:

$$L_{peak} = A_0 SEL + B_0 + 10\log\left(\frac{Z_{p0}^2 m_r}{Z_p^2 m_{r0}}\right). \quad (8.7)$$

It must be noted that this equation is equivalent to Eq. 5.1, where  $A = A_0$  and  $B$  has an extra correction term,  $B = B_0 + 10\log\left(Z_{p0}^2 \cdot m_r / Z_p^2 / m_{r0}\right)$ . If the Onslow data are used as a reference set, then the correction of  $B$  for the Port Phillip Bay data set is -1.4 dB, i.e.  $B = 6.3 - 1.4 = 4.9$  dB, which is higher than the value  $B = 2.4$  dB derived from the Onslow data. However, the difference is small.

Thus Eq. 8.7 can be used to estimate mean values of  $L_{peak}$  from either measured  $SEL$  values or modelled  $SEL$  values for different piles and hammers. The latter case would be equivalent of using the semi-empirical method presented in section 5.4 for airgun array signals but using Eq. 8.7 instead of Eq. 5.1. A comparison of empirical predictions for  $L_{peak}$ , using numerical predictions for  $SEL$  and Eq. 8.7, with experimental data is beyond the scope of this study.

## 8.4 Fluctuations of the peak pressure level of pile driving signals around the mean value

### 8.4.1 Analysis of the Onslow data

Function  $y$  (defined in Eq. 7.1) was calculated for the Onslow data using all 30,000 piling signals. It is represented in Fig. 8.5, where the fluctuations around the value  $\bar{y} = 10^{B/10}$  are shown.

Figure 8.6 show the histogram and CDF of the experimental function  $y$  and its best fit by a Gumbel distribution, which resulted in the location and scale parameters  $\mu = 1.566 \pm 0.006$  and  $\sigma = 0.478 \pm 0.004$  respectively for a 95% confidence interval. As one can see, the approximation of the experimental distribution by the Gumbel model is reasonably accurate.

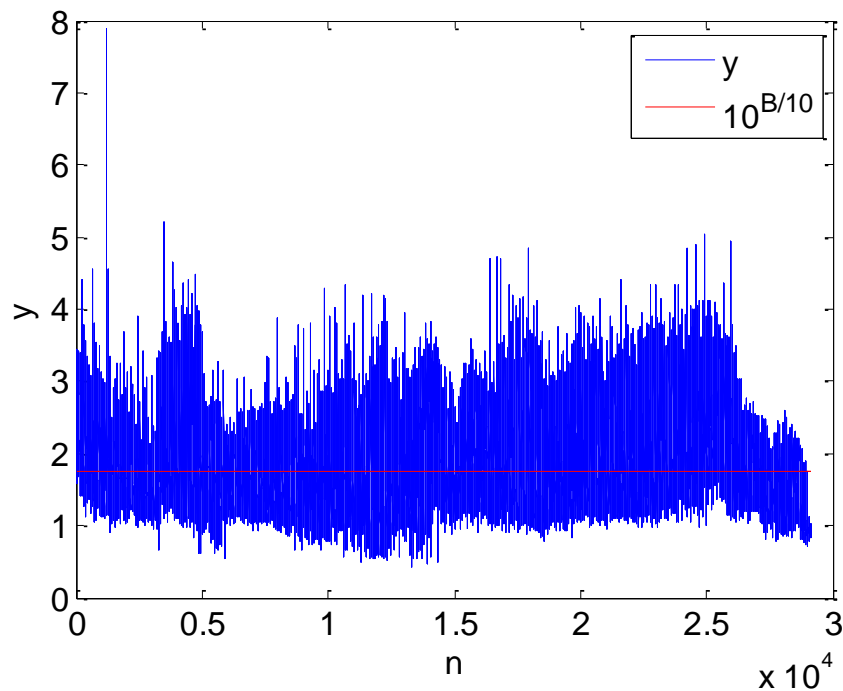


Fig. 8.5: Fluctuations of the ratio  $y$  around the constant value of  $10^{B/10}$  predicted from Eq. 7.2 using the coefficient  $A$ . The number  $n$  represents the order of each individual measurement of the data set.

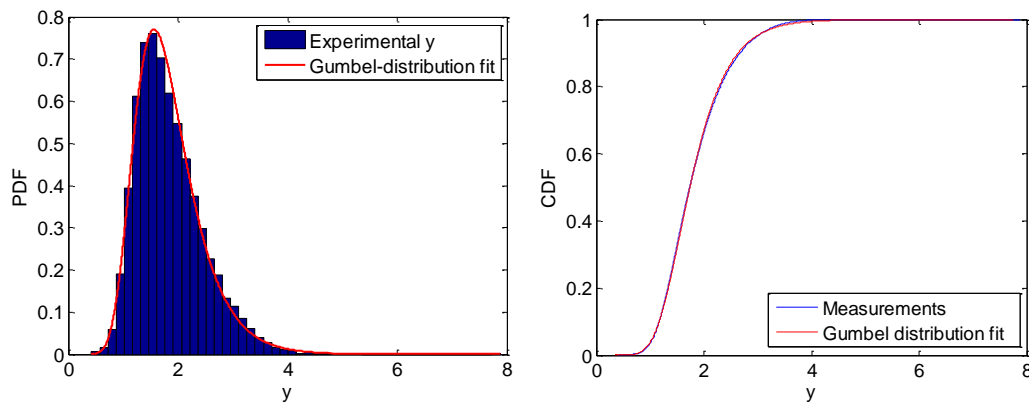


Fig. 8.6: (a) Histogram of  $y$  calculated with the experimental data (blue) and its best fit by a Gumbel distribution (red). (b) Cumulative Density Function (CDF) of measurements (blue) and Gumbel distribution fit (red).

### 8.4.2 Description of the algorithm

The first approach to calculate the probability of  $L_{peak}$  staying below a certain threshold could be using the nearly normal distribution of the difference between the measured and predicted values of  $L_{peak}$ , shown in Fig. 8.4. However, a better algorithm, which has a theoretical foundation and is based on the same methodology as that used for airgun array signals, is presented here. See section 7.2 for the theoretical basis.

The applicability of the algorithm depends on the availability of experimental data in the same way it was described for airgun array signals in section 7.5. The algorithm can be used with empirical measurements, if we have recordings at many different distances. Alternatively, when only data at few ranges is available or no data have been recorded (prior to the commencement of pile driving operation), the algorithm could be used with a modelled  $SEL$  and parameters  $A_0$ ,  $B_0$ ,  $\mu_G$  and  $\sigma_G$ . In this case, steps 1 to 3 are omitted. This would be a semi-empirical method which needs to be verified, as the modelling of pile driving signals was out of the scope of this project.

Based on the results given in the previous sections, the following algorithm is suggested. One must note that Steps 3 to 6 are equivalent to the algorithm developed for airgun array signals in section 7.5.

1. If the number and span of measurements are sufficient to estimate the regression coefficients with relatively small confidence intervals (e.g.  $\pm 5\%$  of estimated value at 95% probability) and a high quality of fit (e.g. adjusted  $R^2$  statistics  $\geq 0.95$ ), the linear regression coefficients  $A$  and  $B$  can be calculated from the best fit of the variations of  $L_{peak}$  vs  $SEL$ . Otherwise they can be estimated using reference values  $A_0$  and  $B_0$  from the other piling operations where data are available. In this case,  $A = A_0$  and  $B = B_0 + 10 \log \left[ \frac{(Z_{P0}^2 \cdot m_r)}{(Z_P^2 \cdot m_{r0})} \right]$ , according to Eq. 8.7. The values presented here for the Onslow site can be used as reference values.
2. The function  $y$  is calculated using Eq. 7.2. with the slope  $A$  from step 1.
3. The location and scale parameters  $\mu$  and  $\sigma$  are obtained by finding the best Gumbel distribution fit to the distribution of  $y$ , calculated with Eq. 7.1. The number of samples of  $y$  should be large enough to ensure relatively small confidence intervals (e.g.  $\pm 5\%$  of estimated value at 95% probability).
4. The probability  $P$  ( $0 < P < 1$ ) is chosen and then the threshold  $y|_P$  is calculated using the quantile function (Eq. 7.5) and the parameters  $\mu$  and  $\sigma$ .
5. The  $SEL$  values are taken from the measurements and/or modelled using an underwater sound propagation model for ranges where measurements are not available.
6. Using  $A_0$  as the slope and the measured/modelled  $SEL$  values vs range, the threshold peak pressure level is calculated using Eq. 7.6, so that  $P \times 100\%$  of signals are expected to have  $L_{peak}$  values below this threshold.

The algorithm described here needs to be thoroughly verified using data from different pile driving operations with different piles and hammers and different locations, which is beyond the scope of this research project.

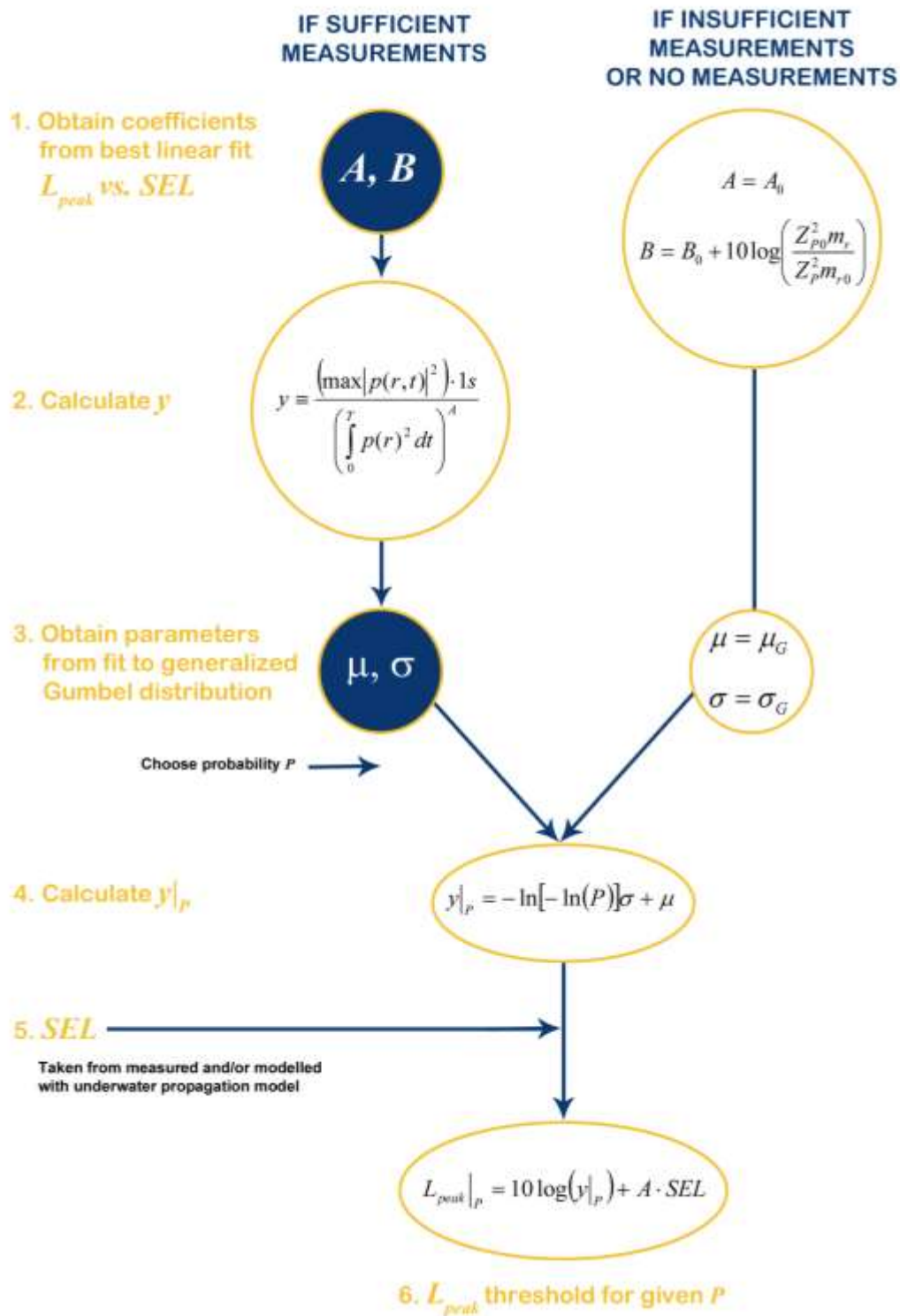


Fig. 8.7: Visualization of the algorithm to estimate the fluctuations of  $L_{peak}$  around its mean value and its upper limit of chosen probability for pile driving signals.

## 8.5 Concluding remarks

Measurements of impulsive noise from offshore impact pile driving close to Onslow, in Western Australia, were analysed.

An alternative formulation to estimate  $L_{peak}$  from  $SEL$  was presented, where the offset  $B$  has a correction term accounting for variations in the characteristics of piles and hammers.

An algorithm to estimate the fluctuations of  $L_{peak}$  around the mean value and its upper limit of chosen probability was also suggested, which needs to be verified with data from multiple sites including different characteristics of piling and the environment. Finally, the semi-empirical approach to predict  $L_{peak}$  and its fluctuations for pile driving signals, based on numerical modelling of  $SEL$  and generalised parameters, also needs to be verified in future studies, as modelling the propagation of pile driving signals was beyond the scope of this project.

This page intentionally left blank

# Chapter 9.

## Conclusions

**T**his chapter summarises and discusses the main findings and achievements resulting from the completion of this project. To conclude the chapter, recommendations for future work are made.

### 9.1 Conclusions

This study was mostly motivated by the requirements of predicting the peak pressure level  $L_{peak}$  in noise impact assessments developed with the goal of protecting the marine environment from noise pollution, and the current limitation of the existing sound propagation models to accurately predict the peak pressure and its variations.

The project was planned to accomplish three main objectives, which were described in section 1.2 and are repeated here for the reader's convenience:

1. Improving the theoretical understanding of changes in the peak pressure that occur as an impulsive signal propagates in a randomly fluctuating underwater sound channel in the ocean.
2. Developing a method to predict peak pressure values and/or their probability distribution as a function of range.
3. Verifying the results of the model by comparison with measured data.

The main tasks undertaken to fulfil the objectives and the results obtained are summarised and discussed hereunder:

- Modelling of sound propagation from an airgun array used for a seismic survey was done and the results were presented in Chapter 4. Two propagation models were chosen to simulate the sound signal at the receiver, PE-based RAMGeo and an adiabatic mode model. The predictions were compared with the measurements at the location of the survey (off Cape Leeuwin, Western Australia). Both models predicted a similar decay rate for the sound exposure level  $SEL$ , which was close to the measured decay. RAMGeo offered more realistic prediction result because it allows for coupling of signals propagated with different modes in contrast to the adiabatic mode model. However, both models predicted slower decay rates of the peak pressure than the experimental data. This result confirms the previous observations and theoretical grounds explained in Chapter 1 and Chapter 2 relative to the difficulties associated with the prediction of  $L_{peak}$ , particularly at long distances from the source, even when the energy or  $SEL$  can be accurately predicted.

- A method to predict  $L_{peak}$  more accurately than using the existing sound propagation models was presented in this thesis and tested with successful results, accomplishing objectives (2) and (3). The full method can be separated into two parts; (a) a method to predict the average value of  $L_{peak}$  at each distance; and (b) a statistical method to model the fluctuations of  $L_{peak}$  around the mean value and estimate the upper limit of fluctuations at specified probability level. Each part is discussed below.

(a) Airgun array signals from three different surveys described in Chapter 3 were used to conduct an empirical study of the correlation between  $L_{peak}$  and  $SEL$ . The analysis led to the formulation of an empirical linear equation which can be used to estimate  $L_{peak}$  from the values of  $SEL$ . The values of the regression coefficients  $A$  are governed by the physics of sound propagation in the ocean sound channel but they were found to be very similar and thus nearly independent of the environment. The values of the regression coefficients  $B$  were also very similar for the different surveys, and they are

expected to be dependent primarily on the sound source parameters, as discussed in Chapter 6. This motivated a generalised analysis with all data combined to obtain generalised regression coefficients independent of the environmental parameters. The values obtained are the slope  $A_G = 1.213 \pm 0.005$  and the offset  $B_G = -20.1 \pm 0.6$  dB re 1  $\mu$ Pa. The empirical equation with coefficients  $A_G$  and  $B_G$  was used to predict  $L_{peak}$  of airgun array signals from their  $SEL$  values at distances from about 1 km to nearly 100 km. Variations of the difference between the prediction of  $L_{peak}$  using the empirical equation, and the measurements of  $L_{peak}$  followed a nearly normal distribution with the mean of 0.00 dB and standard deviation of 1.64 dB. In those cases where either no measurements of the signals are available or only measurements at few distances are available, a semi-empirical method was proposed. This method is based on using the empirical regression equation with the values of  $SEL$  predicted with a numerical model of sound propagation (which can be modelled with good accuracy). This method was tested with the Cape Leeuwin data set using the PE code RAMGeo for numerical modelling. The difference with the measurements followed a nearly normal distribution of 0.09 dB mean and 2.79 dB standard deviation. The peak pressure level  $L_{peak}$  predicted directly from the waveform modelled using RAMGeo exceeded the measured values by more than 10 dB at certain distances greater than 48 km and the difference varied from -2.5 and 14.6 dB at ranges between 70 and 94 km. Therefore, the result obtained with the semi-empirical method was proved to be significantly more accurate than the result obtained by direct application of an underwater acoustic model, as shown in Chapter 5.

(b) The method to estimate the fluctuations of  $L_{peak}$  around the mean value was obtained as follows. Using the correlation between  $L_{peak}$  and  $SEL$  and the generalised coefficient  $A_G$ , a new variable  $y$  was defined to quantify the fluctuations of the peak pressure around its mean value due to randomly varying interference. Extreme value theory was used to approximate the distribution of  $y$  using the properties of the peak pressure as a maximum

value taken from a Rayleigh distributed amplitude. New generalised parameters  $\mu_G$  and  $\sigma_G$  were obtained from the best fit of  $y$  by a generalized Gumbel distribution, which were used to estimate the probability of  $L_{peak}$  staying below a certain threshold. The method was applied to the Cape Leeuwin data set to calculate the upper limit of  $L_{peak}$  for 90% of its values. Comparison with measurements showed an agreement for over 80% of values. Therefore, the method offers a good approximation to estimate the threshold for a certain percentage of  $L_{peak}$  fluctuations around the mean value previously predicted with the semi-empirical model, as shown in Chapter 7. The theory on which the method is based, presented at the beginning of the chapter, improves the understanding of the statistics of  $L_{peak}$  variations in randomly fluctuating underwater environments, which aided achieving objective (1).

- Source signals were modelled for a broad selection of single airguns and airgun arrays to analyse the dependence of the correlation between the peak pressure and sound exposure levels on source parameters. The analysis of the single guns' signals demonstrated that the sound exposure and the squared peak pressure are linearly dependent on the gun volume. The analysis of both single guns and airgun arrays showed that the correlation between  $L_{peak}$  and  $SEL$  is nearly independent of the volume of the guns or arrays. The variation of  $L_{peak}$  with the azimuth angle was shown to be significantly larger than that of  $SEL$ . A correction term  $\beta(\theta)$  dependent on the azimuth angle and specific to the airgun array was presented to correct for the variation of the relation between  $L_{peak}$  and  $SEL$  of the source signal with azimuth angle different from  $0^\circ$ . The correction approach requires testing with signals measured at different azimuth angles relative to the orientation of an airgun array. Additionally, while the values of  $B$  seem to be dependent on the source type, analysis of source signals from different acoustic source types is required to confirm this.

- Measurements of impulsive noise from offshore impact pile driving close to Onslow, in Western Australia, were analysed. An alternative formulation to estimate  $L_{peak}$  from  $SEL$  was presented, where the offset  $B$  has a correction term accounting for variations in the characteristics of piles and hammers. An algorithm to estimate the fluctuations of  $L_{peak}$  around the mean value and its upper limit of chosen probability was also suggested, which needs to be verified with data from multiple sites including different characteristics of piling and the environment. Finally, the semi-empirical approach to predict  $L_{peak}$  and its fluctuations for pile driving signals, based on numerical modelling of  $SEL$  and generalised parameters, also needs to be verified in future studies, as modelling the propagation of pile driving signals was beyond the scope of this project.
- Finally, the results presented here are not limited to the Australian marine environments (where data were collected). Because of the diversity of the areas studied, the results of this project are applicable to other environments with similar characteristics worldwide. Moreover, the results shown in Chapter 6 and 8 demonstrate that the type of source and its parameters have a larger influence on the correlation between  $L_{peak}$  and  $SEL$  than the environment. Therefore, the results presented in this thesis are considered relevant to the international scientific community and industry working in this field.

## 9.2 Future work

In light of the current state of the research on predicting the peak pressure level of anthropogenic impulsive signals propagated underwater, the following studies are recommended for further progress.

- Further testing of the empirical equation described in Chapter 5 with measurements taken in different seismic surveys, particularly at short distances from the source.

- Further testing of the algorithm described in Chapter 7 with a more suitable data set, i.e., with a data set containing a larger number of measurements at long ranges than the Cape Leeuwin data set. For such a data set, the extreme value theory is expected to produce more accurate results, given that one of the assumptions of the model is having a large number of events (signal arrivals).
- Empirical verification of the equation formulated to predict  $L_{peak}$  of airgun array signals emitted at different azimuth angles relative to array orientation.
- Modelling of sound emission and propagation from offshore piling to test the validity of the semi-empirical method for pile driving signals.
- Further testing of the algorithm described in Chapter 8 for pile driving signals with more data sets including different piles, hammers and environments.
- Analysis of signals from other anthropogenic sources of impulsive underwater noise, such as underwater explosions and sonars in various environments to compare the values of the regression coefficients and then assess the applicability of the methods presented here to predict the peak pressure level of such signals as a function of range.

## REFERENCES

1. Hildebrand, J.A., *Anthropogenic and natural sources of ambient noise in the ocean*. Marine Ecology Progress Series, 2009. **395**: p. 5–20.
2. National Research Council, *Ocean Noise and Marine Mammals*, ed. W. Natl. Acad. Press, D. C. 2003.
3. Tyack, P.L. and Miller, E.H., *Vocal Anatomy, Acoustic Communication and Echolocation*, in *Marine Mammal Biology: An Evolutionary Approach*, S. Blackwell, Editor. 2002: Oxford, England. p. 142-184.
4. McCauley, R. and Salgado Kent, C.P., *Pile Driving Underwater Noise Assessment, Proposed Bell Bay Pulp Mill Wharf Development*. 2008, Centre for Marine Science and Technology, Curtin University.
5. Hastings, M.C. and Popper, A.N., *Effects of Sound on Fish*, T.O. Subconsultants to Jones & Stokes Under California Department of Transportation Contract No. 43A0139, Editor. 2005.
6. De Jong, C.A.F. and Ainslie, M.A., *Underwater radiated noise due to the piling for the Q7 Offshore Wind Park*. The Journal of the Acoustical Society of America, 2008. **123**(5): p. 2987-2987.
7. Richardson, W.J., Würsig, B., and Greene Jr, C.R., *Reactions of bowhead whales, Balaena mysticetus, to drilling and dredging noise in the Canadian Beaufort Sea*. Marine Environmental Research, 1990. **29**(2): p. 135-160.
8. Madsen, P.D., *Wind turbine underwater noise and marine mammals: implications of current knowledge and data needs*, in *Marine Ecology Progress Series*. 2006. p. 279–295.
9. Popper, A.N. and Hawkins, A., *The Effects of Noise on Aquatic Life*, ed. Springer. 2012, New York, USA.

## REFERENCES

---

10. Southall, B.L., Bowles, A.E., Ellison, W.T., Finneran, J.J., Gentry, R.L., Jr, C.R.G., Kastak, D., Ketten, D.R., Miller, J.H., Nachtigall, P.E., Richardson, W.J., Thomas, J.A., and Tyack, P.L., *Marine mammal noise exposure criteria: Initial scientific recommendations*. *Aquatic Mammals*, 2007. **33**(4): p. 411-521.
11. Mueller-Blenkle, C., McGregor, P.K., Gill, A.B., Andersson, M.H., Metcalfe, J., Bendall, V., Sigray, P., Wood, D., and Thomsen, F., *Effects of pile-driving noise on the behaviour of marine fish*. 2010, COWRIE.
12. Simmonds, M.P., Dolman, S.J., Jasny, M., Parsons, E.C.M., and Weilgart, L., *Marine Noise Pollution - Increasing Recognition But Need for More Practical Action*. *Journal of Ocean Technology*, 2014. **9**(1): p. 71-90.
13. Richardson, W.J., Green Jr., C.R., Malme, C.I., and Thomson, D.H., *Marine Mammals and Noise*, ed. A. Press. 1995.
14. Southall, B.L., Bowles, A.E., Ellison, W.T., Finneran, J.J., Gentry, R.L., Jr, C.R.G., Kastak, D., Ketten, D.R., Miller, J.H., Nachtigall, P.E., Richardson, W.J., Thomas, J.A., and Tyack, P.L., *Marine mammal noise exposure criteria: Overview*. *Aquatic Mammals* 2007. **33**(4): p. 411-414.
15. Gordon, J.C.D., Gillespie, D., Potter, J., Frantzis, A., Simmonds, M.P., Swift, R., and Thompson, D., *A review of the effects of seismic survey on marine mammals*. *Marine Technology Society Journal*, 2004. **37**(4): p. 14-32.
16. McCauley, R., *High intensity anthropogenic sound damages fish ears*. *Acoustical Society of America*, 2003. **113**(1): p. 638-642.
17. McCauley, R. and Kent, C., *A Lack of Correlation Between Air Gun Signal Pressure Waveforms and Fish Hearing Damage*, in *The Effects of Noise on Aquatic Life*, A. Popper and A. Hawkins, Editors. 2012, Springer New York. p. 245-250.
18. Popper, A.N., Smith, M.E., Cott, P.A., Hanna, B.W., MacGillivray, A.O., Austin, M.E., and Mann, D.A., *Effects of exposure to seismic airgun use on*

- 
- hearing of three fish species*. The Journal of the Acoustical Society of America, 2005. **117**(6): p. 3958-3971.
19. Song, J., Mann, D.A., Cott, P.A., Hanna, B.W., and Popper, A.N., *The inner ears of Northern Canadian freshwater fishes following exposure to seismic air gun sounds*. The Journal of the Acoustical Society of America, 2008. **124**(2): p. 1360-1366.
20. Gross, J.A., Irvine, K.M., Wilmoth, S., Wagner, T.L., Shields, P.A., and Fox, J.R., *The Effects of Pulse Pressure from Seismic Water Gun Technology on Northern Pike*. Transactions of the American Fisheries Society, 2013. **142**(5): p. 1335-1346.
21. Clark, C.W., Ellison, W.T., Southall, B.L., Hatch, L., Parijs, S.M.V., Frankel, A., and Ponikaris, D., *Acoustic masking in marine ecosystems: intuitions, analysis, and implications*. Marine Ecology Progress Series, 2009. **395**: p. 201-222.
22. Erbe, C., *Underwater noise of whale-watching boats and potential effects on killer whales (orcinus orca), based on an acoustic impact model*. Marine Mammal Science, 2002. **18**(2): p. 394-418.
23. Lucke, K., Siebert, U., Lepper, P.A., and Blanchet, M.-A., *Temporary shift in masked hearing thresholds in a harbor porpoise (Phocoena phocoena) after exposure to seismic airgun stimuli*. The Journal of the Acoustical Society of America, 2009. **125**(6): p. 4060-4070.
24. Finneran, J.J., Schlundt, C.E., Dear, R., Carder, D.A., and Ridgway, S.H., *Temporary shift in masked hearing thresholds in odontocetes after exposure to single underwater impulses from a seismic watergun*. The Journal of the Acoustical Society of America, 2002. **111**(6): p. 2929-2940.
25. McCauley, R., Fewtrell, J.L., Duncan, A.J., Jenner, C., Jenner, M.-N., and Penrose, J.D., *Marine seismic surveys - A study of environmental implications*. APPEA Journal, 2000: p. 692-708.

## REFERENCES

---

26. Fewtrell, J.L. and McCauley, R., *Impact of air gun noise on the behaviour of marine fish and squid*. *Marine Pollution Bulletin*, 2012. **64**: p. 984–993.
27. Gailey, G., Würsig, B., and McDonald, T., *Abundance, behavior, and movement patterns of western gray whales in relation to a 3-D seismic survey, Northeast Sakhalin Island, Russia*. *Environmental Monitoring and Assessment*, 2007. **134**(1-3): p. 75-91.
28. Blackwell, S.B., Nations, C.S., McDonald, T.L., Thode, A.M., Mathias, D., Kim, K.H., Greene, C.R., Jr., and Macrander, A.M., *Effects of Airgun Sounds on Bowhead Whale Calling Rates: Evidence for Two Behavioral Thresholds*. *PLoS ONE*, 2015. **10**(6): p. e0125720.
29. Risch, D., Corkeron, P.J., Ellison, W.T., and Van Parijs, S.M., *Changes in Humpback Whale Song Occurrence in Response to an Acoustic Source 200 km Away*. *PLoS ONE*, 2012. **7**(1): p. e29741.
30. Melcón, M.L., Cummins, A.J., Kerosky, S.M., Roche, L.K., Wiggins, S.M., and Hildebrand, J.A., *Blue Whales Respond to Anthropogenic Noise*. *PLoS ONE*, 2012. **7**(2): p. e32681.
31. Skalski, J.R., Pearson, W.H., and Malme, C.I., *Effects of Sounds from a Geophysical Survey Device on Catch-per-Unit-Effort in a Hook-and-Line Fishery for Rockfish (*Sebastes spp.*)*. *Canadian Journal of Fisheries and Aquatic Sciences*, 1992. **49**(7): p. 1357-1365.
32. Erbe, C., *International regulation of underwater noise*. *Acoustics Australia*, 2013. **41**(1): p. 12-19.
33. Harwood, J., King, S., Schick, R., Donovan, C., and Booth, C., *A Protocol for Implementing the Interim Population Consequences of Disturbance (PCoD) Approach: Quantifying and Assessing the Effects of UK Offshore Renewable Energy Developments on Marine Mammal Populations in Scottish Marine and Freshwater Science*. 2014, Marine Scotland Science

- 
34. Boyd, I.L., Frisk, G., Urban, E., Tyack, P., Ausubel, J., Seeyave, S., Cato, D., Southall, B., Weise, M., Andrew, R., Akamatsu, T., Dekeling, R., Erbe, C., Farmer, D., Gentry, R., Gross, T., Hawkins, A., Li, F., Metcalf, K., Miller, J.H., Moretti, D., Rodrigo, C., and Shinke, T., *An International Quiet Ocean Experiment*. *Oceanography*, 2011. **24**(2).
  35. McCarthy, E., *International Regulation of Underwater Sound: Establishing Rules and Standards to Address Ocean Noise Pollution*, ed. I. Springer-Science+Business Media. 2004: Kluwer Academic Publishers.
  36. EPBC Act, *Environment Protection and Biodiversity Conservation Act 1999 - C2012C00685* 2012, Office of Legislative Drafting and Publishing, Attorney-General's Department, Canberra.
  37. Duncan, A.J., McCauley, R.D., and Maggi, A.L. *Predicting the Environmental Impact of Active Sonar*. in *AIP High Frequency Ocean Acoustics Conference*. 2004.
  38. Australian Government, Department of the Environment,, Water,, Heritage and the Arts,, *EPBC Act Policy Statement 2.1 – Interaction between offshore seismic exploration and whales* 2008.
  39. New Zealand Department of Conservation, *2013 Code of Conduct for Minimising Acoustic Disturbance to Marine Mammals from Seismic Survey Operations*. 2013.
  40. MSFD, *Marine Strategy Framework Directive. Directive 2008/56/EC of the European Parliament and of the Council, in Commission Decision of 1st September 2010*. 2008, The European Parliament and the Council of the European Union: Official Journal of the European Union, L232/14.
  41. RWE npower renewables, *Atlantic Array Offshore Wind Farm. Draft Environmental Statement, Vol.3, Annex 19.1: Underwater Noise Modelling*. 2012, RWE npower renewables.

## REFERENCES

---

42. OSPAR. *OSPAR Commission*. 15th January 2016]; Available from: <http://www.ospar.org/>.
43. ACCOBANS, *Anthropogenic noise and marine mammals. Review of the effort in addressing the impact of anthropogenic underwater noise in the ACCOBAMS and ASCOBANS areas*.
44. Marine Mammal Commission, *The Marine Mammal Protection Act (MMPA) of 1972*. 1972, NOAA's National Marine Fisheries Service.
45. *Endangered Species Act of 1973*. Department of the Interior U.S. Fish and Wildlife Service, U.S.
46. Duncan, A., McCauley, R., Parnum, I., and Salgado Kent, C.P. *Measurement and Modelling of Underwater Noise from Pile Driving*. in *20th International Congress on Acoustics, ICA 2010*. 2010. Sydney, Australia.
47. TNO, *Standard for measurement and monitoring of underwater noise, Part I: physical quantities and their units*, M. Ainslie, Editor. 2011, TNO. p. 67.
48. Van der Graaf, A.J., Ainslie, M., André, M., Brensing, K., Dalen, J., Dekeling, R.P.A., Robinson, S., Tasker, M.L., Thomsen, F., and Werner, S., *European Marine Strategy Framework Directive - Good Environmental Status (MSFD-GES)*, in *Report of the Technical Subgroup on Underwater noise and other forms of energy*. 2012.
49. Fisheries Hydroacoustic Working Group, *Agreement in Principle for Interim Criteria for Injury to Fish from Pile Driving*. 2008.
50. Sertlek, H.O., Slabbekoorn, H., Ten Cate, C.J., and Ainslie, M.A. *Insights into the calculation of metrics for transient sounds in shallow water*. 2012. Edinburgh, Scotland.
51. McQuinn, I.H. and Carrier, D., *Far-field Measurements of Seismic Airgun Array Pulses in the Nova Scotia Gully Marine Protected Area in Canadian*

- 
- Technical Report of Fisheries and Aquatic Sciences 2615* 2005, Physics Department, Sherbrooke University, Sherbrooke, Quebec, J1K 2R1.
52. Matthews, M.-N.R. and MacGillivray, A.O., *Comparing modeled and measured sound levels from a seismic survey in the Canadian Beaufort Sea*. Proceedings of Meetings on Acoustics, 2013. **19**(1): p. -.
53. Madsen, P.T., *Marine mammals and noise: Problems with root mean square sound pressure levels for transients*. Journal of the Acoustical Society of America, 2005. **117**(6): p. 3952-3957.
54. Weilgart, L.S., *The impacts of anthropogenic ocean noise on cetaceans and implications for management*. Canadian Journal of Zoology, 2007. **85**(11): p. 1091-1116.
55. Jensen, F.B., Kuperman, W. A., Porter, M. B., Schmidt, H., *Computational Ocean Acoustics*, ed. M.A.a.S. Processing. 2011.
56. Etter, P.C., *Underwater Acoustic Modeling and Simulation: Principles, Techniques and Applications*. Third ed, ed. T.F.G. Spon Press. 2003, London & New York.
57. Brekhovskikh, L.M. and Lysanov, Y.P., *Fundamentals of Ocean Acoustics*. Third Edition ed, ed. M.A.a.S. Processing. 2003.
58. Urick, R.J., *Principles of underwater sound*, ed. McGraw-Hill. 1983.
59. Makarov, D., Prants, S., Virovlyansky, A., and Zaslavsky, G., *Ray and Wave Chaos in Ocean Acoustics: Chaos in Waveguides*. Complexity, Nonlinearity and chaos, ed. W.S.P.C.P. Ltd. Vol. 1. 2010, Singapur.
60. Flatté, S.M., *Sound transmission through a fluctuating ocean*, ed. C.U. Press. 1979.
61. Lynch, J.F., Newhall, A.E., Sperry, B., Gawarkiewicz, G., Fredricks, A., Tyack, P., Chiu, C.S., and Abbot, P., *Spatial and temporal variations in*

## REFERENCES

---

- acoustic propagation characteristics at the New England shelfbreak front. Oceanic Engineering, IEEE Journal of*, 2003. **28**(1): p. 129-150.
62. Song, A., Badiey, M., Song, H.C., Hodgkiss, W.S., Porter, M.B., and Group, t.K., *Impact of ocean variability on coherent underwater acoustic communications during the Kauai experiment (KauaiEx)*. The Journal of the Acoustical Society of America, 2008. **123**(2): p. 856-865.
63. Tatarski, V.I., *Wave propagation in a turbulent medium*, ed. McGraw-Hill. 1961, New York.
64. Dyer, I., *Statistics of Sound Propagation in the Ocean*. The Journal of the Acoustical Society of America, 1970. **48**(1B): p. 337-345.
65. Colosi, J.A., Scheer, E.K., Flatte, S.M., Cornuelle, B.D., Dzieciuch, M.A., Munk, W.H., Worcester, P.F., Howe, B.M., Mercer, J.A., Spindel, R.C., Metzger, K., Birdsall, T.G., and Baggeroer, A.B., *Comparisons of measured and predicted acoustic fluctuations for a 3250-km propagation experiment in the eastern North Pacific Ocean*. The Journal of the Acoustical Society of America, 1999. **105**(6): p. 3202-3218.
66. Colosi, J.A., *A reformulation of the  $\Lambda$ - $\Phi$  diagram for the prediction of ocean acoustic fluctuation regimes*. The Journal of the Acoustical Society of America, 2015. **137**(5): p. 2485-2494.
67. Makris, N.C., *The effect of saturated transmission scintillation on ocean acoustic intensity measurements*. The Journal of the Acoustical Society of America, 1996. **100**(2): p. 769-783.
68. Bergman, P.G., *Intensity Fluctuations in Physics of sound in the sea, Part 1: Transmission*. 1946, National Defense Research Committee: Washington, DC.
69. Ramp, S.R., Ching-Sang, C., Bahr, F.L., Yiquan, Q., Dahl, P.H., Miller, J., Lynch, J.F., Renhe, Z., and Jixun, Z., *The shelf-edge frontal structure in the*

- 
- central East China Sea and its impact on low-frequency acoustic propagation. Oceanic Engineering, IEEE Journal of, 2004. 29(4): p. 1011-1031.*
70. Tran, D., Andrews, M., and Ratilal, P., *Probability distribution for energy of saturated broadband ocean acoustic transmission: Results from Gulf of Maine 2006 experiment. The Journal of the Acoustical Society of America, 2012. 132(6): p. 3659-3672.*
71. Bohnenstiehl, D.R., Scheip, C.M., Matsumoto, H., and Dziak, R.P., *Acoustics variability of air gun signals recorded at intermediate ranges within the Lau Basin, in Geochemistry Geophysics Geosystems. 2012, AGU and the Geochemical Society.*
72. Blackman, D.K., de Groot-Hedlin, C., Harben, P., Sauter, A., and Orcutt, J.A., *Testing low/very low frequency acoustic sources for basin-wide propagation in the Indian Ocean. The Journal of the Acoustical Society of America, 2004. 116(4): p. 2057-2066.*
73. Nichols, R.H. and Senko, A., *Amplitude fluctuations of low-frequency underwater acoustic pulses reflected from the ocean surface. The Journal of the Acoustical Society of America, 1974. 55(3): p. 550-554.*
74. Brown, M.V. and Ricard, J., *Fluctuations in Surface-Reflected Pulsed cw Arrivals. The Journal of the Acoustical Society of America, 1960. 32(12): p. 1551-1554.*
75. Duda, T.F., Lynch, J.F., Newhall, A.E., Lixin, W., and Ching-Sang, C., *Fluctuation of 400-Hz sound intensity in the 2001 ASIAEX South China Sea experiment. Oceanic Engineering, IEEE Journal of, 2004. 29(4): p. 1264-1279.*
76. Gavrilov, A.N. and Parnum, I.M., *Fluctuations of Seafloor Backscatter Data From Multibeam Sonar Systems. Oceanic Engineering, IEEE Journal of, 2010. 35(2): p. 209-219.*

## REFERENCES

---

77. Duncan, A.J., Gavrilov, A., and Hu, T., *Using offshore seismic surveys as acoustic sources of opportunity for geoacoustic inversion*. The Journal of the Acoustical Society of America, 2008. **123**(5): p. 3365-3365.
78. Verbeek, N.H. and McGee, T.M., *Characteristics of high-resolution marine reflection profiling sources*. Journal of Applied Geophysics, 1995. **33**(4): p. 251-269.
79. MacGillivray, A.O. and Chapman, N.R., *Results from an acoustic modelling study of seismic airgun survey noise in Queen Charlotte Basin* 2005.
80. Caldwell, J. and Dragoset, W., *A brief overview of seismic air-gun arrays*. The Leading Edge, 2000. **19**(8): p. 898-902.
81. Parkes, G.E. and Hatton, K., *The Marine Seismic Source*, ed. B.V. Springer-Science+Business Media. 1986.
82. Duncan, A.J. and McCauley, R., *Characterisation of an air-gun as a sound source for acoustic propagation studies.*, in *UDT Pacific 2000 Conference*. 2000: Sydney, Australia.
83. Johnston, R.C., *Performance of 2000 and 6000 psi air guns: Theory and experiment\**. Geophysical Prospecting, 1980. **28**(5): p. 700-715.
84. Parkes, G.E. and Hatton, L., *The Marine Seismic Source*, ed. D.R. publ. 1986.
85. Johnson, D.T., *Understanding air-gun bubble behavior*. Geophysics, 1994. **59**(11): p. 1729-1734.
86. Butcher, J.C., *Numerical Methods for Ordinary Differential Equations*. 2003: John Wiley.
87. Duncan, A., *Research Into the Acoustic Characteristics of an Air Gun Sound Source*. 1998, CMST for DSTO.
88. PGS. *Nucleus*. Available from: <https://www.pgs.com/>.
89. Associates, O.C. *Gundalf*. Available from: <https://www.gundalf.com/>.

- 
90. Parkes, G.E., Ziolkowski, A., Hatton, L., and Haugland, T., *The signature of an air gun array: Computation from near-field measurements including interactions - Practical considerations*. *Geophysics*, 1984. **48**(2): p. 105-111.
91. Dahl, P.H., De Jong, C.A.f., and Popper, A.N., *The underwater sound field from impact pile driving and its potential effects on marine life*. *Acoustics Today*, 2015. **11**(2): p. 18-25.
92. Reinhall, P.G. and Dahl, P.H., *Underwater Mach wave radiation from impact pile driving: Theory and observation*. *The Journal of the Acoustical Society of America*, 2011. **130**(3): p. 1209-1216.
93. Dahl, P.H. and Reinhall, P.G., *Beam forming of the underwater sound field from impact pile driving*. *The Journal of the Acoustical Society of America*, 2013. **134**(1): p. EL1-EL6.
94. Lippert, S., Nijhof, M., Lippert, T., Wilkes, D., Gavrilov, A., Heitmann, K., Ruhnau, M., Estorff, O.v., Schäfer, A., Schäfer, I., Ehrlich, J., MacGillivray, A., Park, J., Seong, W., Ainslie, M.A., Jong, C.d., Wood, M., Wang, L., and Theobald, P., *COMPILE - A Generic Benchmark Case for Predictions of Marine Pile Driving Noise*. *IEEE JOURNAL OF OCEAN ENGINEERING*, 2015.
95. PACSYS. *FEA / BEM Solutions*. Available from: <http://www.vibroacoustics.co.uk/>.
96. Hamilton, E.L., *Geoacoustic modeling of the sea floor*. *The Journal of the Acoustical Society of America*, 1980. **68**(5): p. 1313-1340.
97. Taroudakis, M.I. and Makrakis, G.N., *Inverse Problems in Underwater Acoustics*. 2001: Springer New York.
98. Chapman, N.R., Chin-Bing, S., King, D., and Evans, R.B., *Benchmarking geoacoustic inversion methods for range-dependent waveguides*. *Oceanic Engineering, IEEE Journal of*, 2003. **28**(3): p. 320-330.

## REFERENCES

---

99. Buckingham, M.J., *Wave and Material Properties of Marine Sediments: Theoretical Relationships for Geoacoustic Inversions*. AIP Conference Proceedings, 2004. **728**(1): p. 3-11.
100. Buckingham, M.J., *Compressional and shear wave properties of marine sediments: Comparisons between theory and data*. The Journal of the Acoustical Society of America, 2005. **117**(1): p. 137-152.
101. Gavrilov, A.N. and Mikhalevsky, P.N., *Mode-Coupling Effects in Acoustic Thermometry of the Arctic Ocean*, in *Inverse Problems in Underwater Acoustics*, I. Springer-Verlag New York, Editor. 2001.
102. Holland, C.W., *Coupled scattering and reflection measurements in shallow water*. Oceanic Engineering, IEEE Journal of, 2002. **27**(3): p. 454-470.
103. Stotts, S.A., Knobles, D.P., and Koch, R.A., *Scattering in a Pekeris waveguide from a rough bottom using a two-way coupled mode approach*. The Journal of the Acoustical Society of America, 2011. **129**(5): p. EL172-EL178.
104. Goff, J.A. and Jordan, T.H., *Stochastic modeling of seafloor morphology; Resolution of topographic parameters by sea beam data*. Oceanic Engineering, IEEE Journal of, 1989. **14**(4): p. 326-337.
105. Palmer, D.R., Brown, M.G., Tappert, F.D., and Bezdek, H.F., *Classical chaos in nonseparable wave propagation problems*. Geophysical Research Letters, 1988. **15**(6): p. 569-572.
106. Potter, J. and Warn-Varnas, A., *Ocean Variability & Acoustic Propagation*, ed. K.A. Publishers. 1991, Netherlands.
107. Maggi, A.L. and Duncan, A.J., *AcTUP v2.21 Acoustic Toolbox User-interface & Post-processor. Installation & User Guide*.
108. Collins, M.D. and Westwood, E.K., *A higher-order energy-conserving parabolic equation for range-dependent ocean depth, sound speed, and density*. The Journal of the Acoustical Society of America, 1991. **89**(3): p. 1068-1075.

- 
109. Collins, M.D., *A split-step Padé solution for the parabolic equation method*. The Journal of the Acoustical Society of America, 1993. **93**(4): p. 1736-1742.
110. Collins, M.D., *Higher-order Padé approximations for accurate and stable elastic parabolic equations with application to interface wave propagation*. The Journal of the Acoustical Society of America, 1991. **89**(3): p. 1050-1057.
111. Tappert, F., *The parabolic approximation method*, in *Wave Propagation and Underwater Acoustics*, J. Keller and J. Papadakis, Editors. 1977, Springer Berlin Heidelberg, p. 224-287.
112. Goh, J.T. and Schmidt, H., *A hybrid coupled wave-number integration approach to range-dependent seismoacoustic modeling*. The Journal of the Acoustical Society of America, 1996. **100**(3): p. 1409-1420.
113. Isakson, M.J. and Chotiros, N.P., *Finite element modeling of reverberation and transmission loss in shallow water waveguides with rough boundaries*. The Journal of the Acoustical Society of America, 2011. **129**(3): p. 1273-1279.
114. Hovem, J.M., Tronstad, T.V., Karlsen, H.E., and Lokkeborg, S., *Modeling Propagation of Seismic Airgun Sounds and the Effects on Fish Behavior*. Oceanic Engineering, IEEE Journal of, 2012. **37**(4): p. 576-588.
115. Gavrilov, A., Duncan, A., and Wu, J.R. *Geoacoustic inversion from the transmission loss and arrival structure of air-gun signals propagated in deep water*. in *Underwater Acoustic Measurements: Technologies & Results, 2nd International Conference and Exhibition*. 2007. Heraklion, Crete.
116. Hall, M.V. *Toward a simple model for peak pressure of underwater signals from offshore impact pile driving*. in *Acoustics 2012 Fremantle: Acoustics, Development and the Environment*. 2012. Fremantle, Australia.
117. McCauley, R., Fewtrell, J.L., Duncan, A., Jenner, C., Jenner, M.-N., Penrose, J.D., Prince, R.I.T., Adhitya, A., Murdoch, J., and McCabe, K., *Marine seismic surveys: Analysis and propagation of air-gun signals; and effects of air-gun exposure on humpback whales, sea turtles, fishes and squid*. 2000,

- Centre for Marine Science and Technology for Australian Petroleum Production Exploration Association.
118. Siderius, M. and Porter, M.B., *Modeling techniques for marine-mammal risk assessment*. Oceanic Engineering, IEEE Journal of, 2006. **31**(1): p. 49-60.
119. Hovem, J.M., *PlaneRay: An acoustic underwater propagation model based on ray tracing and plane-wave reflection coefficients in Forsvarets forskningsinstitutt/Norwegian Defence Research Establishment (FFI)*. 2008.
120. Korakas, A. and Hovem, J.M. *Comparison of modeling approaches to low-frequency noise propagation in the ocean*. in *OCEANS - Bergen, 2013 MTS/IEEE*. 2013.
121. Bailey, H., Senior, B., Simmons, D., Rusin, J., Picken, G., and Thompson, P.M. *Assessing underwater noise levels during pile-driving at an offshore windfarm and its potential effects on marine mammals*. Elsevier, 2010. **60**, 888–897.
122. Lippert, T. and von Estorff, O., *The significance of parameter uncertainties for the prediction of offshore pile driving noise*. The Journal of the Acoustical Society of America, 2014. **136**(5): p. 2463-2471.
123. Jones, A.D., Clarke, P. A. *Peak levels from SUS measured in shallow oceans in the Australian region*. in *Underwater Acoustics Measurements: Technologies & Results*. 2005. Heraklion, Crete, Greece.
124. Jones, A.D. and Clarke, P.A. *Underwater sound received from some Defense activities in shallow ocean regions*. in *ACOUSTICS 2004*. 2004. Gold Coast, Australia.
125. Soloway, A.G. and Dahl, P.H., *Peak sound pressure and sound exposure level from underwater explosions in shallow water*. The Journal of the Acoustical Society of America, 2014. **136**(3): p. EL218-EL223.

- 
126. McCauley, R., *Air gun signals from the Cliff Head, Lilian and Mary Ann surveys 2003, and the movement of signing humpback whales from acoustic tracking*. 2004, Centre for Marine Science and Technology, Curtin University.
127. CMST. *Underwater Sound Recorder*. Available from: <http://cmst.curtin.edu.au/products/underwater-sound-recorder/>.
128. Massey, F.J., *The Kolmogorov-Smirnov Test for Goodness of Fit*. Journal of the American Statistical Association, 1951. **46**(253): p. 68-78.
129. Barger, J.E. and Hamblen, W.R., *The air gun impulsive underwater transducer*. The Journal of the Acoustical Society of America, 1980. **68**(4): p. 1038-1045.
130. Lippert, T., Galindo-Romero, M., Gavrilov, A.N., and von Estorff, O., *Empirical estimation of peak pressure level from sound exposure level. Part II: Offshore impact pile driving noise*. The Journal of the Acoustical Society of America, 2015. **138**(3): p. EL287-EL292.
131. Primas, H., *Basic Elements and Problems of Probability Theory*. Journal of Scientific Exploration, 1999. **13**(4): p. 579-613.
132. Whiteway, T., *Australian Bathymetry and Topography Grid, June 2009. Scale 1:5000000.*, G.A.R. 2009/21, Editor. 2009. p. 46.
133. CANZ, *New Zealand 250m Bathymetry Grid*. 2008.
134. Galindo-Romero, M., Gavrilov, A., and Duncan, A., *Fluctuations of the peak pressure level of man-made impulsive sound signals propagating in the ocean*. JASA, 2017. **141**(2): p. 661-668.
135. Embrechts, P., Kluppenberg, C., and Mikosch, T., *Modelling Extremal Events*, ed. Springer. 1988.
136. Castillo, E., *Extreme Value Theory in Engineering*, ed. A. Press. 1998.

## REFERENCES

---

137. Beirlant, J., Goegebeur, Y., Segers, J., Teugels, S., and Ferro, C., *Statistics of Extremes: Theory and Applications*. Probability and Statistics, ed. J.W.S. Ltd. 2004.
138. Deeks, A.J., *Numerical analysis of pile driving dynamics*, in *Department of Civil Engineering*. 1992, University of Western Australia: Crawley, Australia.

Every reasonable effort has been made to acknowledge the owners of copyright material. I would be pleased to hear from any copyright owner who has been omitted or incorrectly acknowledge.

## APPENDIX A: Acronyms

A list of acronyms used throughout the text is presented in this appendix.

ACCOBANS	Agreement on the Conservation of Cetaceans of the Black Sea, Mediterranean Sea and Contiguous Atlantic Area
AMM	Adiabatic Mode Model
ASCOBANS	Agreement on the Conservation of Small Cetaceans of the Baltic and North Seas
ASIAEX	Asian Seas International Acoustics Experiment
EPBC	Environment Protection and Biodiversity Conservation Act 1999
ESA	Endangered Species Act 1973
ETV	Extreme Value Theory
FDM	Finite Difference Method
FEM	Finite Elements Method
GES	Good Environmental Status, as defined in MSFD
HELCOM	Helsinki Commission
HF	High Frequency
JNCC	Joint Nature Conservation Committee
LF	Low Frequency
LR	Linear Regression
MMPA	Marine Mammal Protection Act of 1972
MSFD	Marine Strategy Framework Directive
NM	Normal Modes

NOPSEMA	National Offshore Petroleum Safety and Environmental Management Authority
PE	Parabolic Equation
RMS	Root-mean-square
SNR	Signal to Noise Ratio
SOFAR	SOund Fixing And Ranging
SSP	Sound Speed Profile
UTM	Universal Transverse Mercator

## APPENDIX B: Symbols

A list of the main mathematical symbols used throughout the text is presented in this appendix. Next to the symbol and its description, the equation number that defines it or the section where it first appears is indicated.

$A$	Regression coefficient in Eq. 5.1 (slope)	Section 5.2.1
$A_G$	Generalised regression coefficient in Eq. 5.1 (slope) obtained with generalised data set	Section 5.3.2
$A_p$	Cross-section of pile	Section 8.3
$A_s$	Specific regression coefficient in Eq. 5.1 (slope) obtained with data specific from one environment (e.g. Cape Leeuwin)	Section 5.2
$B$	Regression coefficient in Eq. 5.1 (offset)	Section 5.2.1
$B_G$	Generalised regression coefficient in Eq. 5.1 (offset) obtained with generalised data set	Section 5.3.2
$B_s$	Specific regression coefficient in Eq. 5.1 (offset) obtained with data specific from one environment (e.g. Cape Leeuwin)	Section 5.2
$c$	Sound speed in water	Section 2.2.1
$c_0$	Reference sound speed in water	Section 2.3.1
$c_p$	Compressional wave speed in water	Section 2.3
$c_p$	Axial pressure wave velocity in pile	Section 8.3
$EL$	Equivalent Energy	Section 2.4.2
$E_p$	Young's modulus	Section 8.3

$E_s$	Sound exposure	Eq. 8.3
$f_p$	Force applied to a pile	Eq. 8.3
$h$	Hypothesis status from K-S test	Chapter 5
$k_0$	Reference wavenumber	Section 2.3.1
$K_1$	Coefficient allowing for effects resulting in the impact-to-sound conversion	Section 8.3
$K_2$	Coefficient allowing for energy losses due to pile-ground friction, sound radiation into the seabed and spreading loss in the underwater sound channel	Section 8.3
$L_{peak}$	Peak pressure level	Eq. 1.3
$L_{peak}  _P$	$L_{peak}$ threshold for probability $P$	Eq. 7.6
$M$	Number of statistically independent complex variables	Section 7.2
$\hat{M}$	Complex variable defined as two times $M$	Section 7.2
$m_r$	Mass of a ram of a pile driver	Section 8.3
$n$	Refraction index	Section 2.3.1
$P$	Probability	Section 7.2
$P_p$	Peak pressure	Eq. 8.4
$p$	Sound pressure	Eq. 2.27
$p$	$p$ -value from K-S test	Chapter 5
$R_{CE}$	Inverse of square root of $\hat{M}$	Section 7.2
$R_I$	Ratio of the standard deviation of $\max p(r,t) $ to the mean value $\langle \max p(r,t) ^2 \rangle$	Eq. 7.7

$r$	Range	Section 2.3.1
$SEL$	Sound Exposure Level	Eq. 1.2
$SL_E$	Source sound exposure level	Eq. 4.3
$SL_{peak}$	Source peak pressure level	Eq. 4.5
$SPL$	Sound Pressure Level	Eq. 1.1
$T$	Integration time	Section 1.1
$T_a$	Average time	Section 1.1
$TL$	Transmission Loss	Section 2.1
$TL_E$	Transmission Loss associated to the Sound Exposure Level	Eq. 4.2
$TL_{peak}$	Transmission Loss associated to the Peak Pressure Level	Eq. 4.4
$t$	Time	Section 1.1
$u$	Radial displacement of pile after hammer strike	Section 8.3
$v_0$	Velocity of hammer at impact	Section 8.3
$y$	Ratio defined to estimate fluctuations around $L_{peak}$	Eq. 7.2
$\bar{y}$	Average of the ratio $y$	Section 7.2
$y _P$	Quantile function to obtain the probability of $L_{peak}$ to be below a threshold	Eq. 7.5
$Z_p$	Mechanical impedance of a pile	Eq. 8.3
$\alpha$	Significance level in K-S test	Chapter 5
$\alpha$	Scale parameter of Gumbel distribution	Section 7.2
$\alpha_p$	Compressional wave attenuation	Section 2.3

$\alpha_s$	Shear wave attenuation	Section 2.3
$\beta$	Shape parameter of Gumbel distribution	Section 7.2
$\beta(\theta)$	Correction term in Eq. 6.1 to predict $L_{peak}$ from $SEL$ for azimuth angles different from $0^\circ$	Eq. 6.2
$\gamma$	Time-bandwidth product of the signal	Section 7.2
$\lambda$	Wavelength of sound signal	Section 4.1.1
$\lambda_{bottom}$	Wavelength of sound signal in sea bottom	Section 4.1.1
$\mu$	Mean from normal distribution fit	Chapter 5
$\mu$	Location parameter from Gumbel distribution fit	Section 7.2
$\mu_G$	Generalised location parameter from Gumbel distribution fit	Section 7.3
$\mu_s$	Specific location parameter from Gumbel distribution fit	Section 7.4.1
$\eta$	Euler–Mascheroni constant	Section 7.2
$\rho$	Sediment density	Section 4.1.3
$\sigma$	Standard deviation from Normal distribution fit	Chapter 5
$\sigma$	Scale parameter from Gumbel distribution fit	Section 7.2
$\sigma_G$	Generalised scale parameter from Gumbel distribution fit	Section 7.3
$\sigma_s$	Specific scale parameter from Gumbel distribution fit	Section 7.4.1
$\omega$	Angular frequency	Section 2.3

## APPENDIX C: Transmission loss associated of signal energy modelled for different attenuation coefficients

The curves presented below are  $TL_E$  vs. range for the Cape Leeuwin site. Measurements are compared with the simulated results obtained with RAMGeo and the normal mode model described in Chapter 4 using three different values of  $\alpha_p$ .

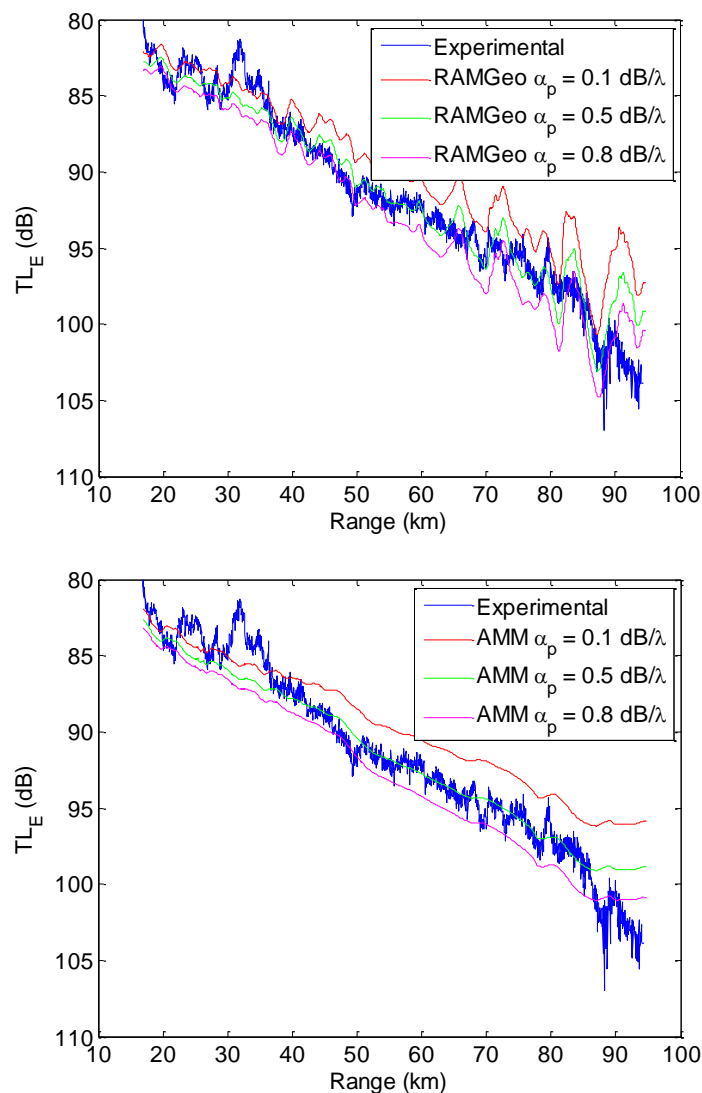


Fig. C.1.1. Transmission loss of the energy for different compressional wave attenuation coefficients modelled using RAMGeo (top) and the adiabatic mode model (bottom)